

**Monte Carlo simulations of
high-energy electron beams:
model validation and dose
calculations**

Pro Gradu, 9.6.2017

Author:

VALTTERI LAHTI

Instructor:

HEIKKI KETTUNEN



JYVÄSKYLÄN YLIOPISTO
FYSIIKAN LAITOS

Abstract

Lahti, Valtteri

Monte Carlo simulations of high-energy electron beams: model validation and dose calculations

Pro Gradu

Department of Physics, University of Jyväskylä, 2017, 115 pages.

A Monte Carlo simulation model of a Varian Clinac 2100 C/D linear accelerator was created in the context of studying radiation effects in electronics. The model was created using Geant4 programming toolkit for modeling the interactions of radiation and matter. The model's ability to predict measurement results about a 20 MeV electron beam was validated by comparing the computed and measured results and recommended steps of future research and development work were defined. Also the absorbed dose in water and silicon phantoms predicted by the model were evaluated and a reference value for the ratio of the absorbed dose and incident electron fluence was calculated. The computed dose profiles were found to be in good agreement with the measured results, but consistent minor deviations between the results were also observed. The differences between the computed and measured results were tracked down to unexpectedly high fractions of low-energy electrons and photons in the computed beam. These anomalies are most likely a consequence of the dual scattering foil model used in the simulation. The model of this part of the accelerator was based on reference values found from literature in the lack of more validated data. In addition, there was small inherent statistical uncertainty to the results which can be done away by increasing the sample size of primary electrons when greater computational power is available.

Keywords: Varian Clinac 2100 C/D, Linear accelerator, Monte Carlo, Electron beam, Computational model

Tiivistelmä

Lahti, Valtteri

Monte Carlo simulations of high energy electron beams: model validation and dose calculations

Pro Gradu

Fysiikan laitos, Jyväskylän yliopisto, 2017, 115 sivua

Komponenttisäteilytykseen valjastetusta Varian Clinac 2100 C/D -lineaarikiihdyttimestä luotiin Monte Carlo -menetelmiä hyödyntävä simulaatiomalli. Malli luotiin aineen ja säteilyn vuorovaikutuksien laskennalliseen mallintamiseen tarkoitettua Geant4 -ohjelmointityökalupakettia käyttäen. Mallin kyky ennustaa mittaustuloksia kiihdyttimen tuottamasta 20 MeV:in elektronisuihkusta todennettiin laskettuja ja mitattuja tuloksia vertailemalla, ja mallin jatkokehityksen kannalta tärkeimmät toimenpiteet määriteltiin. Lisäksi arvioitiin mallin ennustamaa absorpoitunutta annosta vesi- ja piifantomeissa, sekä laskettiin viitearvo absorpoituneen annoksen ja elektronivuon suhteelle. Lasketut annosprofiilit vastasivat mittaustuloksia hyvin, mutta tulosten välillä oli pieniä johdonmukaisia poikkeamia, jotka selittyivät laskennallisen mallin elektronisuihkun odotettua suuremmilla matalaenergisten elektronien ja fotonien osuuksilla. Poikkeamat suihkun hiukkaskoostumuksessa ja energiajakaumassa johtuivat todennäköisesti kiihdyttimen sirontakalvojen mallista, joka perustui kirjallisuudesta löydettyihin viitearvoihin tarkkojen materiaali- ja mittatietojen puuttuessa. Lisäksi laskennallisissa tuloksissa havaittiin hienoista tilastollista epätarkkuutta jota on mahdollista karsia suurentamalla primäärielektronien otoskoko suuremman laskentatehon ollessa saatavilla.

Avainsanat: Varian Clinac 2100 C/D, Lineaarikiihdytin, Monte Carlo, Elektronisuihku, Laskennallinen malli

Contents

Abstract	3
Tiivistelmä	5
1 Introduction	9
2 Theoretical background	13
2.1 Terminology	13
2.2 Relativistic energy scale	13
2.3 On the interactions of radiation and matter	15
2.3.1 Cross sections and scattering theory	15
2.3.2 Electron scattering and collisions	20
2.3.3 Bremsstrahlung	24
2.3.4 Electron-positron annihilation	25
2.3.5 Electron energy loss in matter	26
2.3.6 Electromagnetic radiation	28
2.3.7 Photoelectric effect	30
2.3.8 Compton scattering	32
2.3.9 Electron-positron pair production	35
2.3.10 Rayleigh scattering	37
2.3.11 Relaxation	38
2.3.12 Photonuclear giant dipole resonance	39
2.3.13 Mass attenuation and energy absorption coefficients	42
2.3.14 Electromagnetic cascade	44
2.4 Varian Clinac 2100 C/D	44
2.5 Beam formation in the linear accelerator head	46
2.6 Geant4	48
2.6.1 Object-oriented programming	49
2.6.2 Geometry, materials, particles and tracks	51
2.6.3 Hits, digits and steps	51
2.6.4 Tracking	52
2.6.5 Physics processes	52
2.6.6 Events and runs	53
3 Methods	55
3.1 A Geant4 application for Varian Clinac 2100 C/D	55
3.1.1 Features of the application	55

3.1.2	Modeling the electron beam	57
3.1.3	Modeling the accelerator head geometry	57
3.1.4	Modeling the 20 MeV dual scattering foil	58
3.1.5	Optimizing simulation time and accuracy	61
3.2	Computational methods and calculations	62
3.2.1	Monte Carlo methods	62
3.2.2	Computation of interactions	63
3.2.3	Energy loss and dose calculation	64
3.2.4	Simulation output	67
3.2.5	Data analysis	67
4	Results	71
4.1	Validation of application Varian	71
4.1.1	Electron and photon energy spectra	72
4.1.2	Surface dose profiles	73
4.1.3	Depth dose curve	74
4.2	Depth dose analysis in water and silicon phantoms	78
4.3	The ratio of absorbed dose and incident electrons	80
5	Conclusions	83
	References	87
A	Tabulated data of the materials and structure of the simulation model	95
B	Validation figures	99
C	PDD curves for water and silicon phantoms	113

1 Introduction

In 2014 University of Jyväskylä (JYU) received a Varian Clinac 2100 C/D - linear accelerator as a donation from Kuopio University Hospital. Radiation Effects and Industrial Applications group of JYU is now using this previous radiation therapy device for studies of radiation effects in space electronics.

The Varian accelerator is placed in the accelerator chamber of Radiation Effects Facility (RADEF) located at the bottom of JYU's Department of Physics. Since 2005 RADEF has been an official ESA-supported European Component Irradiation Facility (ECIF) and has performed irradiation tests for ESA, NASA, JAXA, CNES and for other universities and companies.

So far RADEF has specialized in high penetration heavy ion cocktail beams and high and low energy protons. Introducing the Varian Clinac 2100 C/D linear accelerator brings along two new specialties: energetic electrons and photons.

A typical customer request for RADEF may include irradiating a test piece with a given amount of high energy electrons. So far the group has had to work around this type of tasks using only dose data from device calibration measurements without actual particle data. Among other needs this gave reason to create a computational model of the new linear accelerator.

Creating a computer simulation model of an experimental set up is a typical practice in accelerator physics research. It serves several purposes from securing radiation safety to predicting experiment results and analyzing individual events of experiments in detail.

In medical applications simulations play a key role in maximizing the benefits and minimizing the damage done by radiation therapy. But even when not dealing with living targets, a simulation model of the experimental setup provides significant benefits. A simulation can generate several types of data that would be hard or impossible to measure in practice. This makes it possible to recognize and understand different phenomena that take place in the experiment. With the help of simulation results it is possible to make more accurate interpretations of the measurement results.

It is also useful to test the experimental setup before the actual experiment because the samples to be radiated may well be expensive or difficult to obtain. Additionally the beam of the accelerator is an expensive resource and minimizing the beam time is then a priority.

The project to create a simulation model of Varian Clinac 2100 C/D accelerator for the purposes of RADEF was initiated as an undergrad student project in May of 2015. The first version of the simulation model was finished in October 2016 reported by Lahti [1]. In the first version a model of the accelerator operating in 6 MeV photon mode was modeled in the RADEF accelerator chamber. The work was focused around creating a functional simulation program with desired features such as different output files and the possibility to manipulate the simulation settings interactively through the user interface and macro files. The report was a description of the simulation model and its properties written to work as a user's guide for the simulation application.

This study continues on the work of the previous paper. Several new features were added to the simulation including the interchangeable parts of the accelerator geometry to operate the simulation in the 20 MeV electron mode, new interchangeable phantoms, and options for initializing the application to model different experimental setups. Using these new features follows the same logic introduced in the previous paper of this project and will not be described explicitly. Instead, this thesis is focused on practical calculations done with the application and evaluating their validity.

The experimental setup of interest in this study was generating a 20 MeV electron beam in the accelerator head and studying its effects in water and silicon phantoms. Calculations about the ratio of dose deposit and particle flux in these phantoms are also provided. For deeper comprehension, the operation of the accelerator and the physics related to this context are first discussed. Treating the setup as computational problem and understanding the principles of the simulation are also in the focal point of this thesis.

The simulation model was created with Geant4. Geant4 is a Monte Carlo simulation toolkit for the propagation of particles in matter. It is a result of a world wide collaboration of physicists and software engineers. It contains all the functionality required such as models of materials, geometry, physical processes, hits and particle tracking. Geant4 is applicable for energies from a few hundred eV to TeV scale. Many simulation codes for similar purposes exist but Geant4 was chosen for this work because of its detailed and broad documentation, its ongoing development process and the peer review it has gone through. [2, 3, 4, 5, 6, 7]

Geant4 has been implemented with C++ programming language and thus it is object-oriented. Respectively all Geant4 applications follow this object-oriented approach, are written in C++ and utilize the libraries of Geant4. Geant4 provides the libraries for the functionality of the simulation, but the features included such as the application or effect to be modeled, the observables of interest, the required input and the information output are left for the user to decide and implement.

The simulation application used in this study is conveniently named "Varian" and it was created with version 4.10.1 of Geant4. The source code of the application is based on a readily written Geant4 example called MedLinac2 by Claudio Andenna

and Barbara Caccia. It served as a modifiable basis for the accelerator model and provided a source code hierarchy and a method for producing primary particles for the Varian application [1].

2 Theoretical background

2.1 Terminology

This study is focused around a 20 MeV electron beam in a linear accelerator and its effects in different phantoms.

An electronvolt (eV) is a unit of energy equal to the amount of kinetic energy gained by an electron, or any other particle of elementary charge e , as it moves through an electric potential difference of 1 volt (V).

An electron beam of energy E refers to a constant intensity flux of electrons each with energy $\sim E$. Such beams are generated in particle accelerators via thermal emission, accelerated and directed with electric and magnetic fields and manipulated to desired shapes and sizes with shielding instruments.

A phantom is a physical body of a known composition and substance(s) used to study the radiation effects of a given particle beam in a subject of interest.

2.2 Relativistic energy scale

Expressing the values of energy and other quantities in terms of electronvolts is a standard practice in particle physics. This is mainly due to the impracticality of handling very small masses and lengths in terms of SI units, but it is also done among other convenient conventions to lessen the amount of labor in calculations. Below a few exercises are done to help grasp the characteristics of 20 MeV electrons. This is to help the reader understand what can and can not be assumed in this context. This information is valuable when assessing the theoretical models and computational algorithms used to model the physical interactions that take place in the accelerator and the phantoms.

Einstein's mass-energy equivalence $E = mc^2$ includes both the kinetic energy and the rest mass energy of a particle [8]. E denotes the total energy of the particle and c is the speed of light in a vacuum. For the kinetic energy E_k of any particle then holds

$$E_k = mc^2 - m_0c^2, \quad (1)$$

where m_0 is the rest mass of the particle. On the other hand, for a particle moving with velocity v we may write

$$E_k = m_0 c^2 \left[\frac{1}{\sqrt{1 - \frac{v^2}{c^2}}} - 1 \right] \quad [9]. \quad (2)$$

Solving for $\frac{v}{c}$ and substituting E_k from equation 1 gives

$$\frac{v}{c} = \sqrt{1 - \left[\frac{1}{\frac{m_0 c^2 - E_k}{m_0 c^2} + 1} \right]^2}. \quad (3)$$

When dealing with electrons of energies $E = mc^2 \sim 20$ MeV carrying out the calculation of 3 shows the electrons move with speeds $v \sim 0.9997c$

Another way to illustrate the importance of the relativistic approach is to find out the proportional error caused by the classical approach. The classical Newtonian expression for kinetic energy $E_k = \frac{1}{2}m_0 v^2$ is an approximation of the relativistic kinetic energy applicable in low speeds. It can be derived from the relativistic kinetic energy of equation 2 by expanding the square root expression according to the binomial theorem. With v known, the proportional error in kinetic energy ΔE_k due to the unjust assumption $v \ll c$ can be calculated as follows

$$\Delta E_K = \frac{\left[\frac{1}{\sqrt{1 - \frac{v^2}{c^2}}} - 1 \right] m_0 c^2 - \frac{1}{2} m_0 v^2}{\left[\frac{1}{\sqrt{1 - \frac{v^2}{c^2}}} - 1 \right] m_0 c^2}. \quad (4)$$

Thus for electrons traveling at $v = 0.9997c$ the error caused by the classical approach is as much as 98.70%.

The rest mass energy of the 20 MeV electron makes up only 2.55% of its total energy. That is to say the electron's energy is almost entirely due to its momentum p , or more precisely $m_0 c^2 \ll pc$. It may therefore be argued that the ultrarelativistic assumption of neglecting the rest mass portion of the electron's energy is well justified. The total energy of the electron can then be approximated according to equation 5

$$E = mc^2 = \sqrt{p^2 c^2 + m_0^2 c^4} \approx pc \quad [10]. \quad (5)$$

The product of momentum and speed of light pc can be written in terms of kinetic energy

$$pc = \sqrt{E_k^2 + 2E_k m_0 c^2}. \quad (6)$$

For the 20 MeV electron this gives 19.489 MeV. And as for all electrons regardless of momentum, the rest mass energy m_0c^2 is equal to 511 keV summing the total energy to 20 MeV.

The 2.55% error caused by the assumption is small but significant compared to the precision with which the calculations of this study are performed. More over, 20 MeV is the nominal electron energy produced by the accelerator in this study. Many physical processes that contribute to the results take place in lower energies as the electrons lose energy propagating through the structures of the accelerator head and the phantom. As the proportional error increases with decreasing energy, the ultrarelativistic assumption is not a good approximation throughout the path of the electrons. Thus it can be concluded, that the electrons in this context are relativistic, not ultrarelativistic.

2.3 On the interactions of radiation and matter

This study is focused around a 20 MeV electron beam in a linear accelerator and its effects in different phantoms. Thus the topic is here limited to the particles, materials and interactions present in these circumstances. However, even when narrowing down the subject to this special case, there are still numerous physics processes to consider. Here the interactions dominant to particles' energy loss are treated in detail.

2.3.1 Cross sections and scattering theory

There are numerous ways in which radiation can interact with matter. Different interactions take place in different circumstances depending on the type and energy of the radiation as well as on the density and the atomic number of the atoms in the matter. The measure which describes the likelihood of a certain interaction in terms area is cross section σ .

When matter is bombarded with particles, the rate at which different interactions take place is dependent on the intensity and focus of the particle beam as well as on the properties of the target material. Defining a dimensionless probability for a certain event in this context is therefore appropriate only for the specific experimental setup. Contrary to this, a cross section is defined for certain a type of interaction between certain type of particles as a function of particle energy and it is independent of the variables related to the experimental setup. Cross section values are therefore universally comparable.

The concept of cross-section is analogous with classical mechanics. Let us consider an elastic scattering of a small marble from a large marble as pictured in figure 1. The small marble moves in z -direction with an impact parameter b and energy E_k . The large marble has radius R and it's set to be stationary. The impact parameter

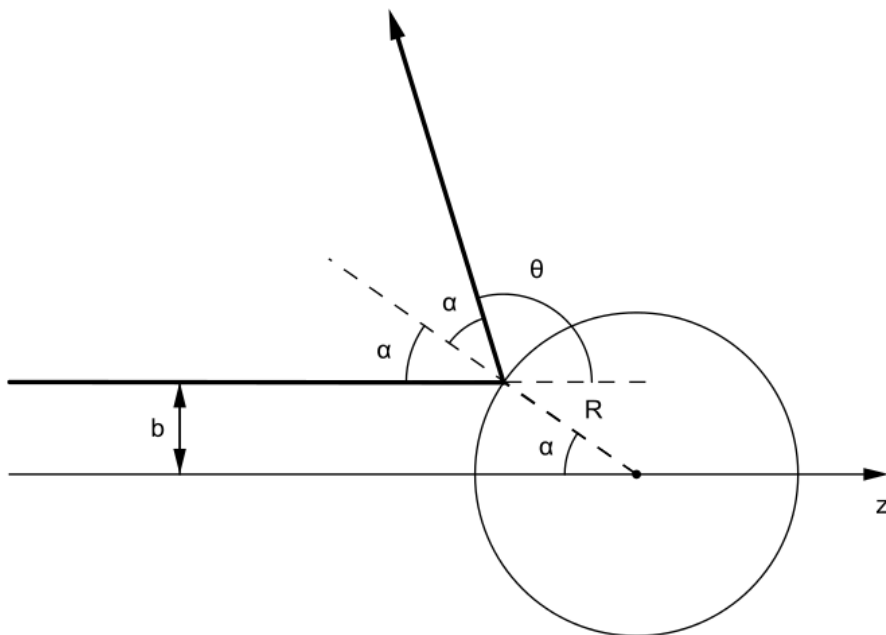


Figure 1. Elastic scattering of hard spheres presented in terms of impact parameter b and scattering angle θ .

b is defined as the perpendicular distance between the path of the moving marble and the center of the stationary marble. For a perfectly round target the situation is azimuthally symmetrical, so the trajectory of the small marble remains in one plane. We can then define an angle α so that $b = R \sin \alpha$ and the scattering angle $\theta = \pi - 2\alpha$. So the relation between b and θ resolves as

$$b = R \sin \left(\frac{\pi}{2} - \frac{\theta}{2} \right) = R \cos \left(\frac{\theta}{2} \right) \quad (7)$$

and for θ we can write

$$\theta = \begin{cases} 2 \arccos(b/R), & \text{if } b \leq R, \\ 0, & \text{if } b \geq R. \end{cases} \quad (8)$$

So the scattering angle becomes larger as the impact parameter decreases, which is an intuitive result.

Now let there be a flux incoming small marbles. Any marble that passes through an infinitesimal region of cross-sectional area in xy -plane denoted as $d\sigma$, will scatter into a corresponding infinitesimal solid angle $d\Omega$. Differential cross-section $d\sigma/d\Omega$ is the probability per unit solid angle that a marble is scattered into the solid angle $d\Omega$. This concept is imaged for long range interactions in figure 2. The differential cross-section is often denoted with $d\sigma/d\Omega$ but here a non-standard notation by Griffiths

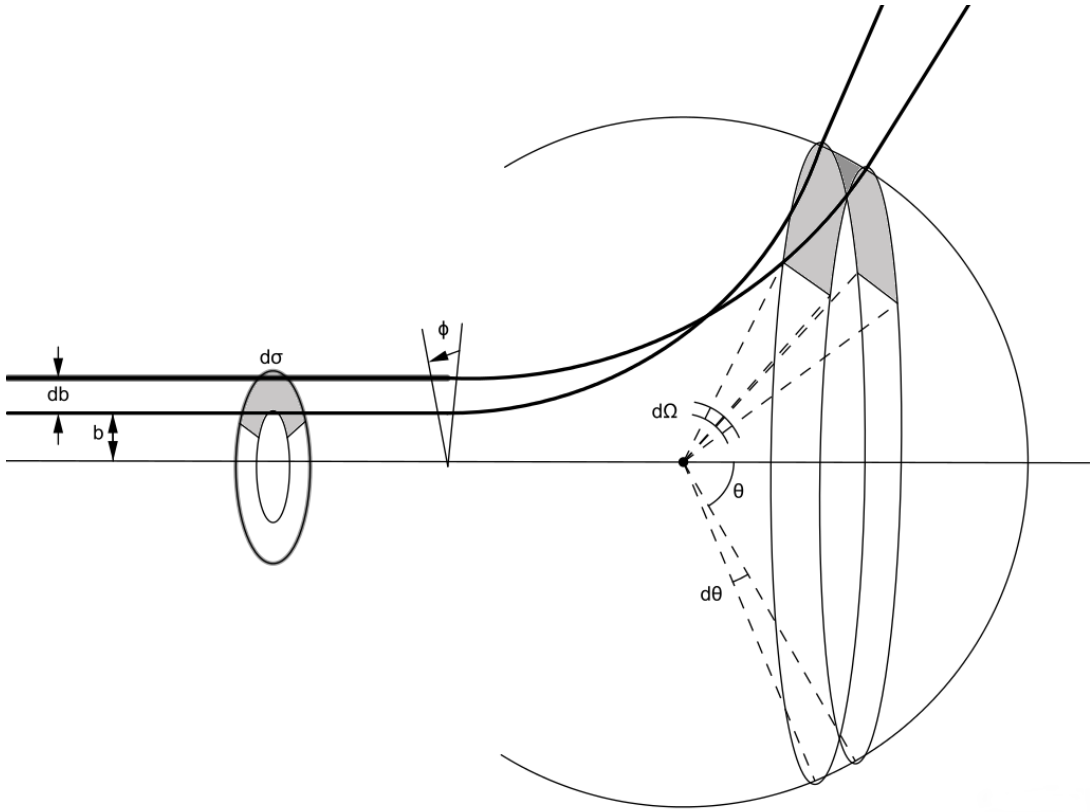


Figure 2. The mathematical formalism developed for hard sphere scattering is equally valid for long range interactions. A particle passing through the cross-sectional area $d\sigma$ will scatter in the corresponding solid angle $d\Omega$.

is adopted to make the following deduction appear coherent [11]. Hence we write $D(\theta) \equiv d\sigma/d\Omega$ and the infinitesimal cross-section region gets the expression

$$d\sigma = D(\theta)d\Omega. \quad (9)$$

On the other hand, we can write $d\sigma = b db d\phi$ and $d\Omega = \sin \phi d\theta d\phi$. Hence the differential cross-section becomes

$$D(\theta) = \frac{b}{\sin \theta} \left| \frac{db}{d\theta} \right|. \quad (10)$$

For the marbles, the change in the impact parameter respect to an infinitesimal change in the scattering angle is

$$\frac{db}{d\theta} = -\frac{1}{2}R \sin\left(\frac{\theta}{2}\right). \quad (11)$$

Substituting the results 7 and 11 to equation 10 then gives the differential cross-section

$$D(\theta) = \frac{R \cos(\theta/2)}{\sin \theta} \left(\frac{R \sin(\theta/2)}{2} \right) = \frac{R^2}{4}, \quad (12)$$

which has no angle dependencies at all. This is a special case due to the symmetry of the spherical marbles. It means that the ratio of incoming marbles passing through a cross-sectional region $d\sigma$ and scattered in corresponding solid angle $d\Omega$ is the same for all azimuthal angles ϕ and scattering angles θ . The ratio simply grows quadratically respect to the radius of the target marble.

The total cross-section is defined as an integral of $D(\theta)$ over the full solid angle of 4 steradians

$$\sigma \equiv \oint_{4\pi} D(\theta) d\Omega = \int_0^{2\pi} \int_0^\pi D(\theta) \sin \theta d\theta d\phi. \quad (13)$$

So for the example this gives an effective area of

$$\sigma = (R^2/4) \oint_{4\pi} d\Omega = \pi R^2, \quad (14)$$

which is the geometrical cross-section of a spherical target marble with radius R . This is the expected result. Any small marble that passes the center of the target marble by a distance longer than the target's radius will miss the target entirely. All marbles within the range of the target's radius will be scattered.

The reason that this simple case example from classical mechanics was presented in detail is that the mathematical formalism developed here is equally valid for the long range interactions of charged particles.

Scattering cross-sections are measured in a laboratory by placing a detector so that it only counts particles scattered in a solid angle $d\Omega$ and thus have passed through the corresponding cross-sectional region $d\sigma$. For a particle beam of constant intensity \mathcal{L} , the number of particles entering the cross-sectional region $d\sigma$ per unit time is $dN = \mathcal{L}d\sigma = \mathcal{L}D(\theta)d\Omega$. This means that for all the particles detected, the differential cross-section is

$$D(\theta) = \frac{1}{\mathcal{L}} \frac{dN}{d\Omega}. \quad (15)$$

Measuring the particle count dN and applying equation 15 gives a universally comparable value for the differential cross-section, since it's normalized to the beam intensity. [11]

Switching to quantum mechanics requires the recognition of the wave-like properties of particles. The wave function ψ of a particle carries the information of what region in space the particle is most probably found. By properly formatting the scattering problem in terms of the incident particle's wave function, solving the Schrödinger equation will reveal how probable it is for a particle to scatter in a given angle.

As in the previous example, let there be a particle traveling towards the center of an azimuthally symmetrical scattering potential in z direction. The quantum treatment of the scattering problem is based on the idea of a plane wave $\psi(z) = Ae^{ikz}$ as pictured in figure 3. As it hits the scattering potential, an outgoing spherical wave

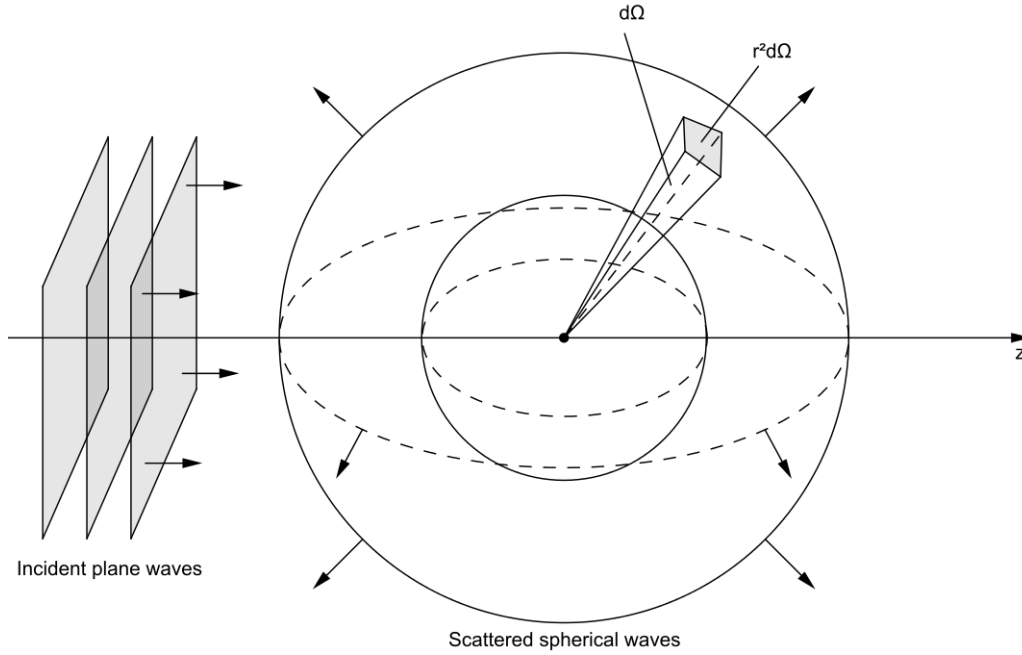


Figure 3. The quantum theory of scattering is based on the idea of an incoming plane wave which scatters as a spherical wave.

$\psi(r, \theta)$ is produced. Thus the solutions of interest to the Schrödinger equation are of the form

$$\psi(r, \theta) \approx A \left(e^{ikz} + f(\theta) \frac{e^{ikr}}{r} \right) \quad (16)$$

which is the sum wave of the incoming plane wave and the scattered spherical wave. The spherical wave has a factor of r^{-1} because the corresponding part of the probability density function $|\psi|^2$ must be proportional to $1/r^2$. The wave number k is related to the energy of the incident particles as

$$k \equiv \frac{\sqrt{2mE}}{\hbar}, \quad (17)$$

and $f(\theta)$ is the scattering amplitude. Scattering amplitude is the quantum mechanical counterpart of differential cross-section as it contains the information of the scattering probability to a given direction. Analogously to the previous example the probability that an incident particle traveling with speed v passes through the infinitesimal cross-sectional region $d\sigma$ in time dt is equal to the probability that the same particle is scattered into the corresponding solid angle $d\Omega$. So for the incident particle holds

$$dP = |\psi_{incident}|^2 dV = |A|^2 (v dt) d\sigma, \quad (18)$$

and for the scattered particle holds

$$dP = |\psi_{scattered}|^2 dV = \frac{|A|^2 |f(\theta)|^2}{r^2} (v dt) r^2 d\Omega. \quad (19)$$

Setting equations 18 and 19 equal yields

$$d\sigma = |f(\theta)|^2 d\Omega, \quad (20)$$

and hence on the basis of equation 9

$$D(\theta) = \frac{d\sigma}{d\Omega} = |f(\theta)|^2. \quad (21)$$

Solving the Schrödinger equation to find out the scattering amplitude is a rigorous exercise and it is not in the focus of this work. For further details the reader should look into Introduction to Quantum Mechanics by Griffiths where techniques such as partial wave analysis and the Born approximation are introduced. [11]

Respectively cross-sections can be defined also for other interactions than scattering. The SI unit of cross-section is 1 m^2 but in practice smaller units are used. The unit barn (1 b) is commonly used in nuclear physics and it is equal to 10^{-28} m^2 or 10^{-24} cm^2 .

The concept of cross section is in the core of the physics models of Geant4 and any other computational model used to predict the outcome of particle interactions. It is therefore crucial to understand. To better grasp it, it is necessary to give up the image of a solid classical particle with a well-defined spatial volume and rather think about the interacting particles as quantum mechanical objects that will interact or pass through each other with an energy-dependent probability.

2.3.2 Electron scattering and collisions

Like all charged particles, electrons lose their energy continuously as they propagate through matter. The dominant processes through which the energy is dissipated are

- elastic collisions accompanied by Coulomb scattering
- inelastic collisions that cause ionization and excitation of atoms
- electromagnetic energy radiated by electrons that experience rapid changes in their velocity. [12]

Coulomb scattering is the elastic scattering of charged particles by Coulomb interaction. This means that the direction of propagation of the charged particle is modified by the electrostatic forces from the atomic electrons and nuclei, so that the kinetic energy of the system is conserved. Consequently the change in the magnitude of the electron's velocity is negligible.

Coulomb scattering occurs mostly due to atomic electrons. Rutherford scattering, which is Coulomb scattering by atomic nuclei, occurs as well but much more rarely. The nuclei in matter occupy only 10^{-15} of the volume of their atoms, so it's crudely 10^{15} times more probable for an incoming particle to be scattered by an atomic electron than by a nucleus. [13]

Conversely to elastic collisions and scattering, in an inelastic collision the total kinetic energy is not conserved. Collisions are more likely to be inelastic in higher energies and with small incident angles thus causing the *primary* electron to slow down but only a minor change to its propagation direction. In an interaction between a propagating primary electron and an atomic electron, the kinetic energy lost in the process will either do the work required to ionize the atom producing a *secondary* electron or simply place the atom to an excited state. In a direct collision of two electrons there is also a problem of identical particles: it's impossible to tell which electron was incident and which was struck. [12, 13]

Ionization energies for materials of interest for this study have been tabulated in table 1. The amount of energy required to remove an atomic electron is of the order of 10 eV. Hence one 20 MeV electron can cause the ionization of thousands of atoms. The energy required to remove an electron from an ion increases with each electron removed. Because this higher order ionization is probable in relativistic energies, it is useful to define a mean excitation energy I which represents the average energy of all occurring atomic ionization and excitation processes. I is an element specific constant with a value of the order of $10Z$ in electronvolts, where Z is the atomic number of the element. Thus the value is higher for heavier elements. While it is possible to calculate a theoretical value for I by averaging over all atomic ionization and excitation processes, in practice it's regarded as an empirical constant. Also the mean excitation energies for the elements of interest in this study have been tabulated in table 1. [14, 13]

If the energy transferred by the primary electron is not enough to free an atomic electron from the atom, the atom will move to a excited state and quickly de-excite by emitting a photon of corresponding characteristic energy. If the energy transferred is of the order of 1 keV or higher, the secondary electron can go on to produce more secondary electrons via inelastic collisions. [12, 13]

The Coulomb scattering process between 2 electrons is known as Møller scattering after Christian Møller who first described it in quantum electrodynamics. The tedious derivation of the differential cross-section for Møller scattering is beyond the scope of this work, but the main result, which is the electron-electron scattering differential cross-section in the center of mass frame is

$$D_M(\theta) = \frac{\alpha^2(2E^2 - m^2)^2}{4E^2(E^2 - m^2)^2} \left(\frac{4}{\sin^4 \theta} - \frac{3}{\sin^2 \theta} + \frac{(E^2 - m^2)^2}{(2E^2 - m^2)^2} \left(1 + \frac{4}{\sin^2 \theta} \right) \right). \quad (22)$$

This equation presents the differential scattering cross-section in natural units, where $\hbar = c = 1$, $[E] = \text{eV}$ and $[m] = \text{eV}/c^2$. Thus, one can see that $[D(\theta)] = 1/(\text{eV})^2$.

Table 1. First ionization energies and mean excitation energies for elements present in this study [14]

Element	Symbol	Ionization energy (eV)	Mean excitation energy (eV)	K-shell binding energy (eV)
Hydrogen	H	13.6	19.2	13.6
Beryllium	Be	9.32	63.7	111.5
Carbon	C	11.3	78.0	284.2
Oxygen	O	13.6	95.0	543.1
Aluminum	Al	5.99	166	1559.6
Silicon	Si	8.15	173	1839
Phosphorus	P	10.5	173	2145.5
Sulfur	S	10.4	180	2472
Chromium	Cr	6.76	257	5989
Manganese	Mn	7.43	272	6539
Iron	Fe	7.90	286	7112
Nickel	Ni	7.64	311	8333
Copper	Cu	7.73	322	8979
Tantalum	Ta	7.55	718	67416
Tungsten	W	7.86	727	69525
Lead	Pb	7.42	823	88005

The transition from natural to SI units gives $\hbar c/1 \text{ eV} \approx 0.1975 \mu\text{m}$ so $1 \text{ eV}^{-2} \approx 0.03894 \mu\text{m}^2$ [10]. The symbol α denotes the fine structure constant which has the value 0.007297 in natural units and 1/137 in SI units.

As can be seen, equation 22 diverges for zero angle and straight angle, that is

$$\lim_{\theta \rightarrow 0} D_M(\theta) = \lim_{\theta \rightarrow \pi} D_M(\theta) = \infty.$$

Thus small angle deflections occur with large cross sections. Two different presentations of $D_M(\theta)$ are given in figure 4. Figure 4(a) is a linearly scaled polar plot of $D_M(\theta)$ for large deflections ($\theta \in [21^\circ, 159^\circ] \cup [201^\circ, 339^\circ]$). Figure 4(c) is a logarithmic polar plot of $D_M(\theta)$ over all angles. It shows the divergent behavior of $D_M(\theta)$ for small deflections. This behavior is expected due to the infinite range Coulomb force. The longer the distance between the electrons is as they pass each other, the weaker the interaction and smaller the deflection angle. The size of the cross-sectional area through which the incident electron may pass is proportional to the square of the distance from the target electron. Therefore very small deflections are most probable.

Figure 4(a) goes to show that there is also a finite cross-section for large deflections. It varies from $100 \mu\text{b}$ to some hundreds of mb depending on the electron energy and exact scattering angle. The figures also show the energy dependence of $D_M(\theta)$. The scattering probability for each angle decreases with increasing electron energy.

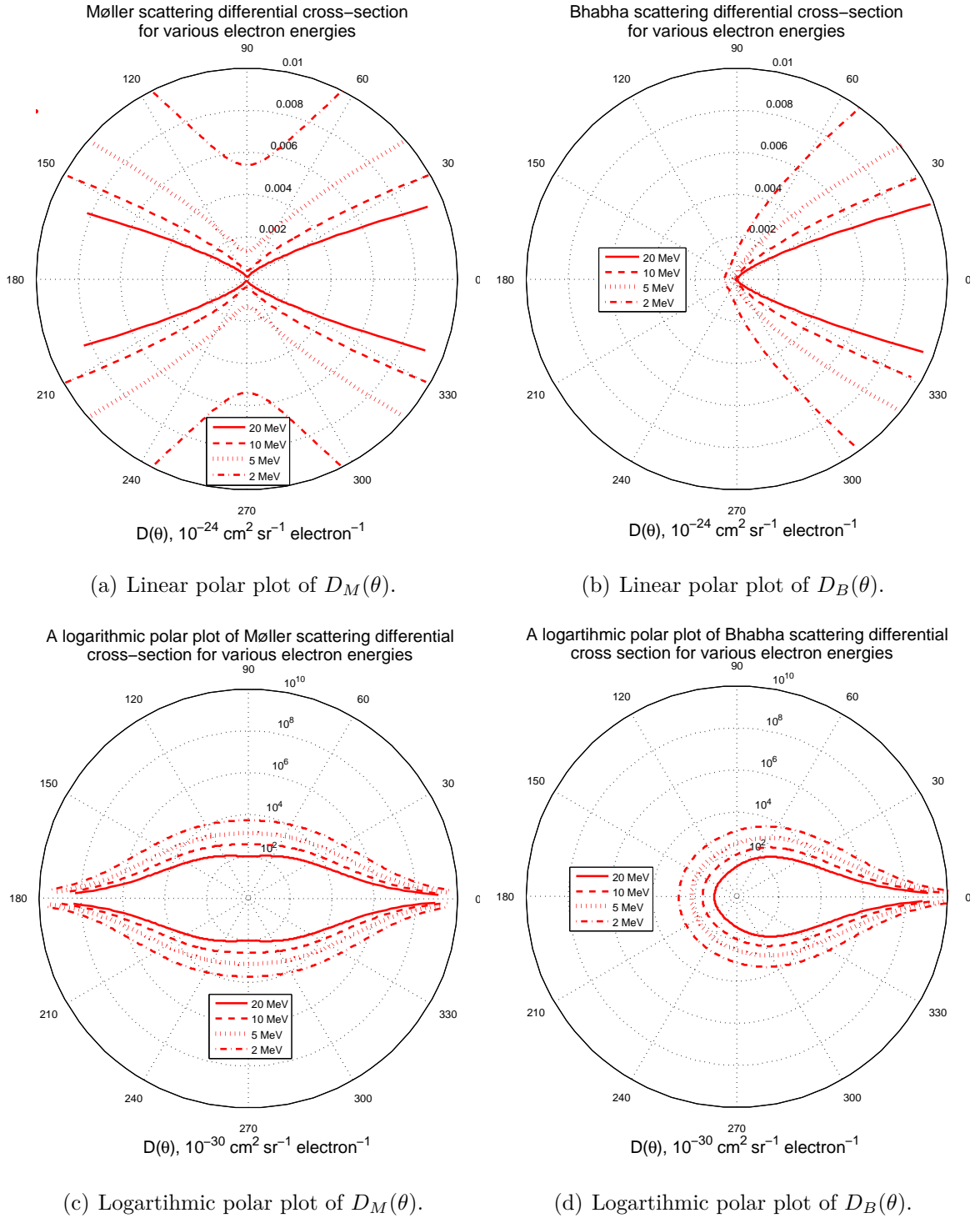


Figure 4. Polar plots of the differential cross-sections of Møller and Bhabha scattering for various energies. The top row images are for large scattering angles and the radial scale is linear with numeric values in barns. In the bottom images cover all scattering angles and the radial scaling is logarithmic with numeric values in microbarns. This scaling was chosen because a logarithmic plot with numeric values below 1 is harder to interpret.

High-energy photons produced in the interactions of the primary electrons may go on to produce electron-positron pairs (see section 2.3.9). Thus, also positrons emerge and cause interactions. Positrons interact and lose energy largely similar to electrons, but significant differences naturally exist due to its opposite charge. Also, in case of positrons there is no identical particle problem in scattering events.

The quantum electrodynamical description of the electron-positron scattering is called Bhabha scattering. The differential cross-section, derived in a manner respective to equation 22, is

$$\frac{\alpha^2}{8E^2} \left(\frac{1}{2}(1 + \cos^2 \theta) + \frac{1 + \cos^4 \frac{\theta}{2}}{\sin^4 \frac{\theta}{2}} - \frac{2 \cos^4 \frac{\theta}{2}}{\sin^2 \frac{\theta}{2}} \right). \quad (23)$$

Figures 4(b) and 4(d) show the linear and logarithmic polar plots of this equation. For deflections less than 90° the curves are somewhat symmetrical to $D_M(\theta)$. The curves start to differ more and more near the origin and the main difference is that for positrons the probability of backscattering is also very small. Unlike with 2 electrons, a collision of a positron and electron is not likely to turn the trajectory of the incident positron around, as there is an attractive force between the two particles.

2.3.3 Bremsstrahlung

When an electron moving in relativistic speed is rapidly decelerated or accelerated by the Coulomb force of a near by particle, the kinetic energy lost in the process is converted into a photon. Electromagnetic radiation produced this way is called bremsstrahlung, which is German for “braking radiation”. [13]

The intensity of bremsstrahlung as a function of wave length is a continuous distribution which shifts towards higher frequencies with increasing incident electron energy. So the higher the electron energy, the higher the potential photon energy. [15]

A comprehensive compilation of bremsstrahlung cross-section calculations and related data has been done by Koch and Motz [16]. Cross-section calculations for bremsstrahlung are complex by nature. Many different theoretical models have been deduced to describe it for different electron and photon energies and different photon emission angles. These formulas can further be sorted by whether they account for atomic screening or not. The screening effect means that the effective Coulomb field at a given point near the target particle may be damped by the presence of other near by charges. [16]

Bremsstrahlung cross-section formulas in the field of an atomic nucleus vary as Z^2 . For high- Z elements the additional influence of electron-electron bremsstrahlung can be included by replacing Z^2 with $Z(Z + 1)$, but for low- Z further measures are needed. [16]

In energies below 50 MeV applicable theoretical models are obtained with the use of Born approximation. The accuracy of these models decreases with increasing atomic number Z of the target material, decreasing incident electron energy and increasing photon frequency near the high-frequency limit. [16]

One form of the bremsstrahlung differential cross-section applicable in the energy range of this study, derived by Tsai, is

$$D(\theta, E_\gamma) = \frac{2\alpha^2 E_e^2}{\pi E_\gamma m_e^4} \left\{ \left[\frac{2y - 2}{(1+l)^2} + \frac{12l(1-y)}{(1+l)^4} \right] Z(Z+1) + \left[\frac{2 - 2y - y^2}{(1+l)^2} - \frac{4l(1-y)}{(1+l)^4} \right] \times [X - 2Z^2 f((\alpha Z)^2)] \right\}, \quad (24)$$

where $y = k/E$, $l = \theta^2 E^2/m_e^2$ and

$$X = \int_{t_{\min}}^{m_e^2(1+l)^2} [G_2^{\text{el}}(t) + G_2^{\text{inel}}(t)] \frac{(t - t_{\min})}{t^2} dt.$$

In these equations E_γ is the photon energy, E_e is the total relativistic energy of the electron, θ is the photon emission angle, m is the electron rest mass energy, $G_2^{\text{el, inel}}(t)$ are elastic and inelastic atomic form factors and $t_{\min} = [E_\gamma m^2(1+l)^2/2E_e(E_e - E_\gamma)]^2$. [17, 18, 19]

2.3.4 Electron-positron annihilation

In electron-positron annihilation an electron and a positron vanish upon interaction producing two photons of equal energy. In the process electric charge, energy, linear momentum and angular momentum are conserved. If the kinetic energies of the initial positron and electron are very small, the photons emerge with energies equal to the rest mass energy of the positron and electron, 511 keV, and they are propelled in opposite directions. For higher kinetic energies the photon energies become higher respectively and the directions of the photons are determined by the momentums of the initial particles.

Electron-positron annihilation may result in a number of other final states including the emission of three or more photons, or heavier particles such as B mesons and W and Z bosons. However, in the energy range of this study only photons are produced, and the inspection of this process is limited to the most probable case of 2 emerging photons. [20]

A cross-section formula for electron-positron annihilation in flight is provided by Heitler

$$\sigma_{an}(Z, E) = \frac{Z\pi r_e^2}{\gamma + 1} \left[\frac{\gamma^2 + 4\gamma + 1}{\gamma^2 - 1} \ln \left(\gamma \sqrt{\gamma^2 - 1} \right) - \frac{\gamma + 3}{\gamma^2 - 1} \right], \quad (25)$$

where $\gamma = E/mc^2$, E is the total relativistic incident positron energy and r_e is the classical electron radius. [21]

2.3.5 Electron energy loss in matter

In previous sections different interactions were discussed separately, but due to the infinite range of the Coulomb force, in reality the propagating electrons interact with multiple other electrons (atomic and free) and nuclei at the same time. And according to the law of conservation of energy, the total energy loss of the electron due to elastic and inelastic collisions is equal to the leftover energy of the primary electron plus all the secondary electron energies and atomic excitations.

The state-of-the-art theoretical models about the relationship of a particle's energy and its penetration range into matter are largely based on the work of Bethe [12]. Equation 26 is the Bethe formula for electrons as presented by Krane [13]. It was derived with the use of quantum mechanical perturbation theory and it describes a propagating electron's energy loss per unit length dE/dx due to collisions and scattering from atomic electrons and nuclei

$$\left(\frac{dE}{dx} \right)_c = \left(\frac{e^2}{4\pi\epsilon_0} \right)^2 \frac{2\pi N_0 Z \rho}{mc^2 \beta^2 A} \left[\ln \frac{E_k (E_k + mc^2)^2 \beta^2}{2I^2 mc^2} + (1 - \beta^2) - (2\sqrt{1 - \beta^2} - 1 + \beta^2) \ln 2 - \frac{1}{8}(1 - \sqrt{1 - \beta^2})^2 \right], \quad (26)$$

where $v = \beta c$, e is the electron charge, ϵ_0 is the permittivity of a vacuum, Z , A and ρ are the atomic number, atomic weight and density of the material, N_0 is the Avogadro's number, m is the electron mass and I is the mean excitation energy of the atomic electrons. The subscript c stands for collision losses. [12, 13]

Since a propagating electron has a small mass, and it's not constrained to a fixed path by any external force, it is subject to large deflections in the many scattering events it goes through. Coulomb scattering can occur at any angle so the direction of propagation may change multiple times leading to an irregular path. A particle's *range* is the linear penetration distance of a certain particle to given matter. A mean range can be defined but for electrons it differs significantly from the length of unpredictable individual paths. [13]

The mathematical expression for electron energy loss due to radiation, also derived by Bethe, is the following

$$\left(\frac{dE}{dx}\right)_r = \left(\frac{e^2}{4\pi\epsilon_0}\right)^2 \frac{Z^2 N_0 (E_k + mc^2) \rho}{137m^2 c^4 A} \left[4 \ln \frac{2(E_k + mc^2)}{mc^2} - \frac{4}{3}\right], \quad (27)$$

where the subscript r stands for radiation losses. [12, 13]

The interactions discussed above are the dominant processes through which an electron's kinetic energy is dissipated in matter. Thus the expression for the electrons total energy loss per unit length becomes

$$\frac{dE}{dx} = \left(\frac{dE}{dx}\right)_c + \left(\frac{dE}{dx}\right)_r. \quad (28)$$

The wavelength of bremsstrahlung photons decreases with increasing electron energy and the radiation losses become more relevant. Below 1 MeV energies the contribution to the total energy loss is negligible but in the relativistic region radiation losses become significant the ratio of the radiation and collision losses is approximately

$$\frac{(dE/dx)_r}{(dE/dx)_c} = \frac{E_k + mc^2}{mc^2} \frac{Z}{1600}. \quad (29)$$

As stated by equation 29, the radiation losses are also more significant in heavier elements. [13]

Radiation length X_0 is a convenient parameter in describing the energy loss of electrons and photons in matter. The higher the electron energy, the higher the fractional energy loss due to bremsstrahlung. The same is true to the pair production process in case of photons (see section 2.3.9). The radiation length X_0 holds the information about the mean distance over which the energy of an electron is reduced to a factor of $1/e$ (where e is the Neper number) of its initial energy due to bremsstrahlung losses. The same distance is also $7/9$ of the mean free path for pair production by energetic photons. [22]

Y.S. Tsai has calculated and tabulated the radiation length for different elements according to

$$\frac{1}{X_0} = 4\alpha r_e^2 \frac{N_A}{A} \left\{ Z^2 [L_{\text{rad}} - f(Z)] + Z L'_{\text{rad}} \right\}. \quad (30)$$

where the function $f(Z)$ is an infinite sum but for elements up to uranium it can be approximated to 4-place accuracy with

$$f(Z) = a^2 \left[(1 + a^2)^{-1} + 0.20206 - 0.0369a^2 + 0.0083a^4 - 0.002a^6 \right], \quad (31)$$

where $a = \alpha Z$. [22, 17, 18]

For $Z > 4$ the parameters L_{rad} and L'_{rad} behave as functions of Z as follows:

$$L_{\text{rad}} = \ln(184.15Z^{-1/3}) \text{ and } L'_{\text{rad}} = \ln(1194Z^{-2/3}). \quad (32)$$

For a mixture or a compound the radiation length can be approximated by

$$1/X_0 = \sum \omega_j/X_j \quad (33)$$

where ω_j and X_j are the mass fraction and radiation length for the j th element. [22]

Radiation length is usually measured in g/cm^2 to account for different material densities. Figure 5 shows the fractional energy loss per radiation length of electrons and positrons in lead. Above critical energy, where the bremsstrahlung losses start to govern the energy loss, the energy loss of positrons and electrons becomes very similar, as the ionization and bremsstrahlung curves are almost identical. Also the Bhabha scattering energy loss approaches the Møller scattering loss curve for higher energies.

Below critical energy, collision losses quickly become dominant, as can be seen from the steep ionization curve and scattering curves that rise with reducing electron/positron energy. However, it should be noted that the energy scale on the horizontal axis is logarithmic.

The fractional energy loss due to a single type of interaction is determined by the probability (cross-section) of that interaction and the average energy loss per interaction. Even though the differential cross-sections for Møller and Bhabha scattering are similar for small angles, the total cross-section of Møller is significantly higher than that of Bhabha-scattering, due to the high probability of back scattering. This difference becomes more significant for decreasing energies, as the scattering differential cross-section curves become rounder (see figure 4). This difference is compensated by the positron annihilation cross-section which becomes larger with decreasing energy.

2.3.6 Electromagnetic radiation

The three dominant processes through which energetic photons interact with matter are

- the photoelectric absorption
- Compton scattering
- pair production.

As demonstrated by figure 6 these interactions have the largest cross-sections in different regions of energy.

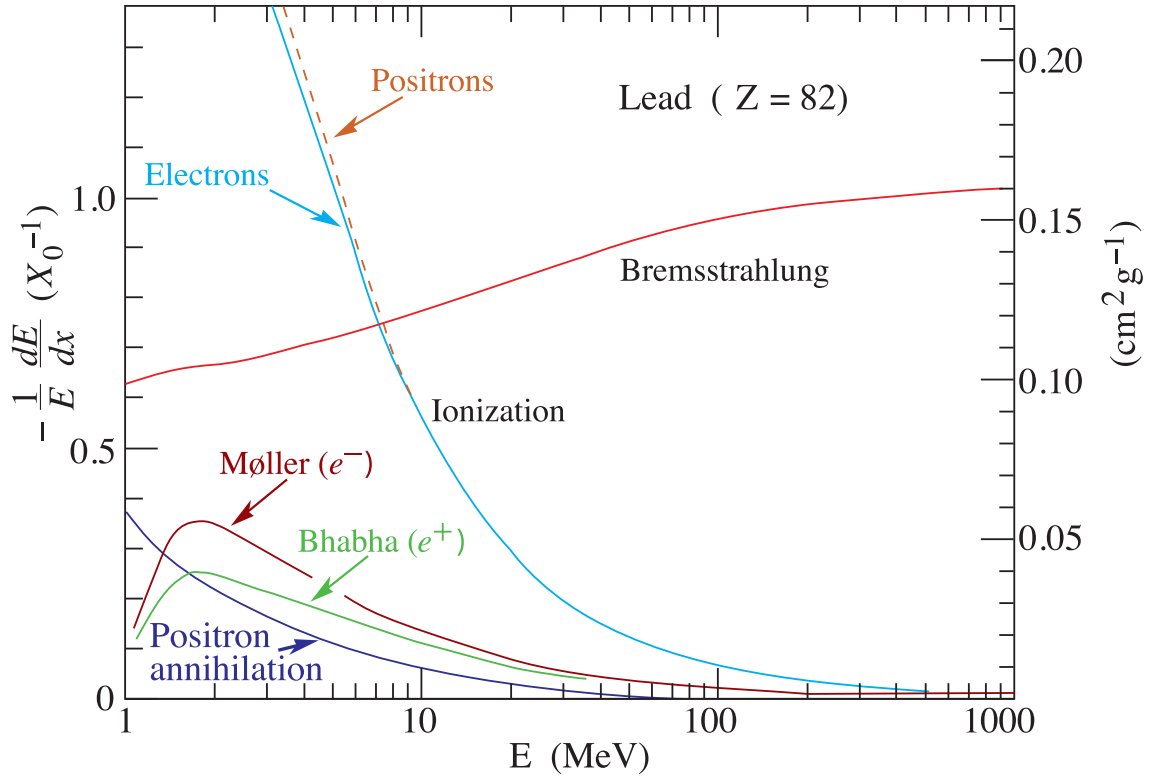


Figure 5. Fractional energy loss per radiation length in lead as a function of electron or positron energy. The fractional energy loss per radiation length is scaled on the left vertical axis and the respective (inverse) radiation length values are on the right vertical axis. Here electron/positron scattering is considered as ionization when the energy loss per collision is below 255 keV and as Møller/Bhabha scattering, when it's above. Original figure by Messel and Crawford [20], who used $X_0(\text{Pb}) = 5.82 \text{ g/cm}^2$. This image was modified by the particle data group to reflect the value $X_0(\text{Pb}) = 6.37 \text{ g/cm}^2$ given in the Table of Atomic and Nuclear Properties of Materials. [22]

2.3.7 Photoelectric effect

Photoelectric effect refers to the emission of an atomic electron by an atom that absorbs a photon of appropriate energy. The emitted electron is called a photoelectron. Photoelectric effect reveals the quantum mechanical nature of light and it was first described by Einstein in his Nobel prize winning work. [23, 13, 24, 25]

Electromagnetic radiation of constant frequency ν consists of photons of fixed energy $E_\gamma = h\nu$, where h is Planck's constant. The photoelectric effect is an interaction between one photon and one electron, so a photon will deliver all of its energy to one electron. The electron receives a kinetic energy of $E_k = E_\gamma - E_B$, where E_B is the binding energy of the electron. Evidently, the photoelectric effect will take place only if $E_\gamma \geq E_B$ so the threshold frequency ν_0 for the electromagnetic radiation can be defined as $\nu_0 = E_B/h$. [23, 13, 24, 25]

The analytical solution for the photoelectric effect cross-section σ_{pe} is complex to derive because it involves wave functions of many atomic electrons. Here the features of photoelectric effect are examined based on experimental findings.

The photoelectric effect cross-section is dependent on the atomic number of the material and on the energy of the photons. Figure 6 shows the photoelectric effect cross-section as a function of photon energy in carbon and lead. The discrete peaks in the cross-section that occur with increasing energy are due to the electron shell-structure of the atom. The inner the electron is in the shell structure, the more tightly it's bound to the nucleus. Characteristically to the photoelectric effect, electrons occupying a given shell will contribute to the total cross-section only if the photon energy is equal or exceeds the binding energy of that specific shell. Thus the cross-section jumps upwards when ever the binding energy of a new shell is attained. [13]

Considering the energies and materials present in this study, the K-shell electrons are the dominant contributors to photon energy loss via photoelectric absorption. The K-shell binding energies for the elements and materials present in this study are also given in table 1.

In general the proportionality of photoelectric absorption cross-section to atomic number and photon energy is the following

$$\sigma_{pe} \begin{cases} \sim Z^4/(h\nu)^3, & \text{for low energies} \\ \sim Z^5/h\nu, & \text{for high energies. [26]} \end{cases} \quad (34)$$

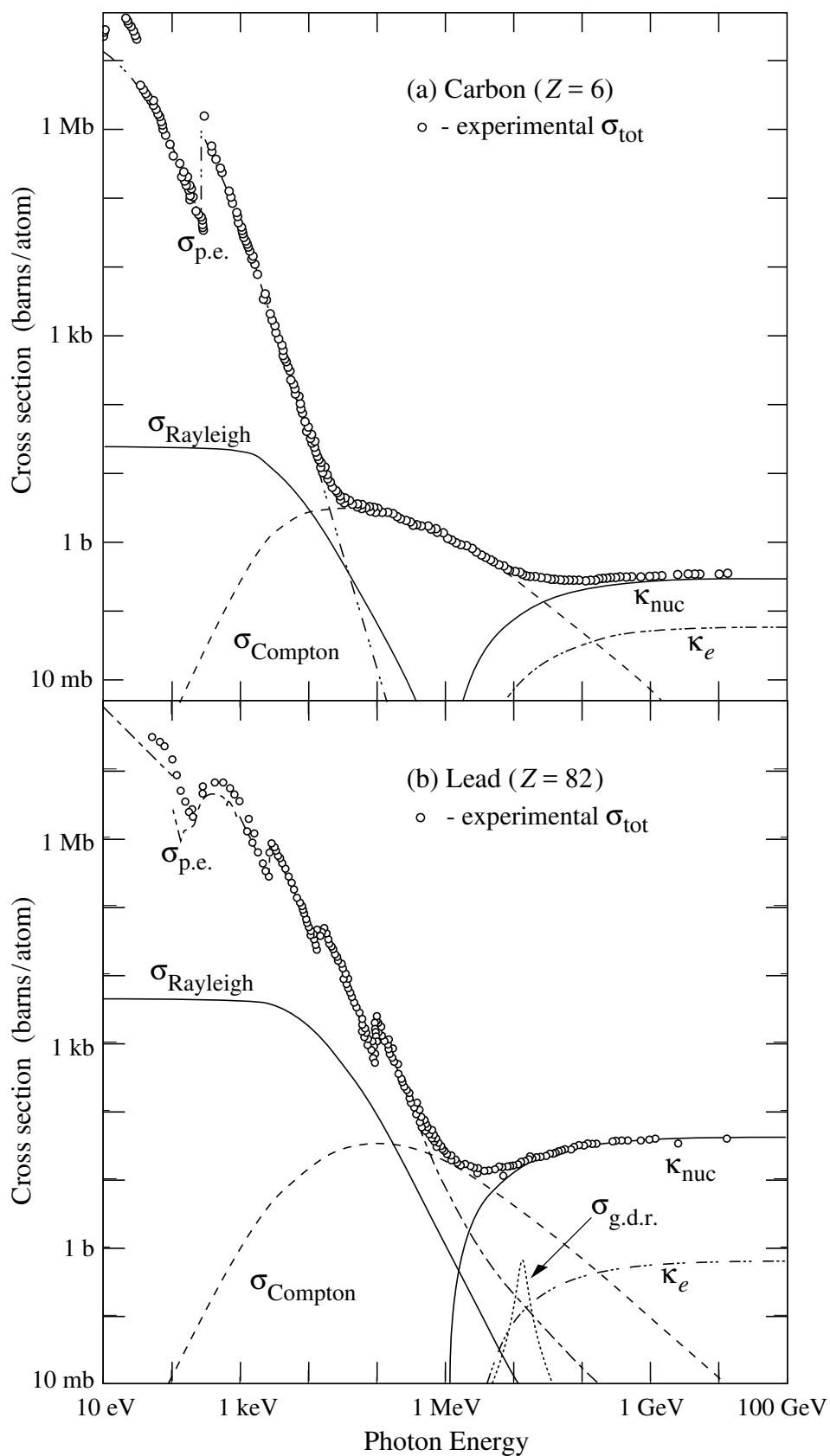


Figure 6. Cross sections for photon interactions in carbon and lead from 10 eV to 100 GeV. Original figures obtained from Particle Data Group collaboration [22] who received them through the courtesy of John H. Hubbell (NIST)

2.3.8 Compton scattering

In Compton scattering, a photon scatters from a quasi-free electron which recoils receiving a fraction of the photon's energy. It was first discovered and explained by Arthur H. Compton when he was studying X-ray scattering in Washington University in 1922. A schematic view of this process is presented in figure 7. [27, 28, 13]

Klein-Nishina theory provides the analytical solution for the Compton scattering cross-section assuming the electron is free and at rest. This assumption is well justified for photon energies above 1 MeV, especially for low- Z materials when the binding energy of the target electron becomes insignificant. [28, 13]

In figure 7 the incident photon has energy $E_\gamma^0 = h\nu_0$ and momentum $P_\gamma^0 = E_\gamma^0/c$. Respectively the scattered photon has energy $E_\gamma = h\nu$ and momentum $P_\gamma = E_\gamma/c$. The momentum of the electron is of the form $P_e = mc\beta/\sqrt{1-\beta^2}$ and its energy is $E_e = mc^2/\sqrt{1-\beta^2}$. Thus over a single Compton scattering event the conservation of linear momentum in x -direction yields

$$\frac{E_\gamma^0}{c} = \frac{E_\gamma}{c} \cos \theta + \frac{mc\beta \cos \phi}{\sqrt{1-\beta^2}}. \quad (35)$$

$$(36)$$

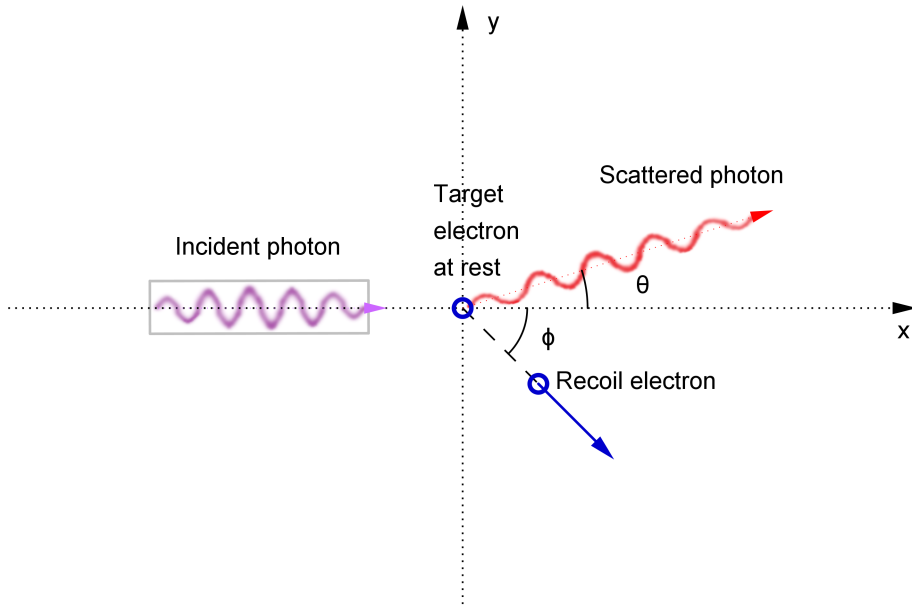


Figure 7. A schematic presentation of Compton Scattering with a free electron at rest.

In y -direction the momentum equation is

$$0 = \frac{E_\gamma}{c} \sin \theta - \frac{mc\beta \sin \phi}{\sqrt{1 - \beta^2}}, \quad (37)$$

$$(38)$$

while the conservation of total energy yields

$$E_\gamma^0 + mc^2 = E_\gamma + \frac{mc^2}{\sqrt{1 - \beta^2}}. \quad (39)$$

Observing the photon energy E_γ^0 allows for the elimination of variables β and ϕ and expressing the energy of the scattered photon in terms of initial photon $E_\gamma^0 = h\nu_0$ energy and photon scattering angle θ

$$h\nu = \frac{h\nu_0}{1 + \left(\frac{h\nu_0}{m_e c^2}\right)(1 - \cos \theta)}. \quad (40)$$

This is known as the Compton-scattering formula. [27, 13]

The probability for Compton scattering at an angle θ can be determined through a quantum mechanical calculation as described in section 2.3.1. The result is the differential scattering cross-section which for Compton scattering is known as the Klein-Nishina formula

$$D_c^{KN}(\theta) = r_0^2 \frac{1 + \cos^2 \theta}{2[1 + h\nu(1 - \cos \theta)]^2} \left[1 + \frac{h\nu^2(1 - \cos \theta)^2}{(1 + \cos^2 \theta)[1 + h\nu(1 - \cos \theta)]} \right]. \quad [28, 13] \quad (41)$$

Further, writing the photon energies in units of electron rest mass energy allows for more compact notation. Thus equation 41 becomes

$$D_c^{KN}(\theta) = \frac{r_0^2}{2} [1 + k(1 - \cos \theta)]^{-2} \left[1 + \cos^2 \theta + \frac{k^2(1 - \cos \theta)^2}{1 + k(1 - \cos \theta)} \right], \quad (42)$$

where $k = h\nu/m_e c^2$. In terms of the initial photon energy $k_0 = h\nu_0/m_e c^2$ the equation reduces to

$$D_c^{KN}(\theta) = \frac{r_0^2}{2} \left(\frac{k}{k_0}\right)^2 \left(\frac{k}{k_0} + \frac{k_0}{k} - \sin^2 \theta\right). \quad (43)$$

The angular distribution of Compton scattering is visualized in a polar plot of figure 8.

Following the scattering theory of section 2.3.1, the total cross section for Compton scattering is obtained by integrating the differential cross-section over all angles θ

$$\sigma^{KN} = 2\pi r_0^2 \left\{ \frac{1 + k}{k^2} \left[\frac{2(1 + k)}{1 + 2k} - \frac{\ln(1 + 2k)}{k} \right] + \frac{\ln(1 + 2k)}{2k} - \frac{1 + 3k}{(1 + 2k)^2} \right\}. \quad [28] \quad (44)$$

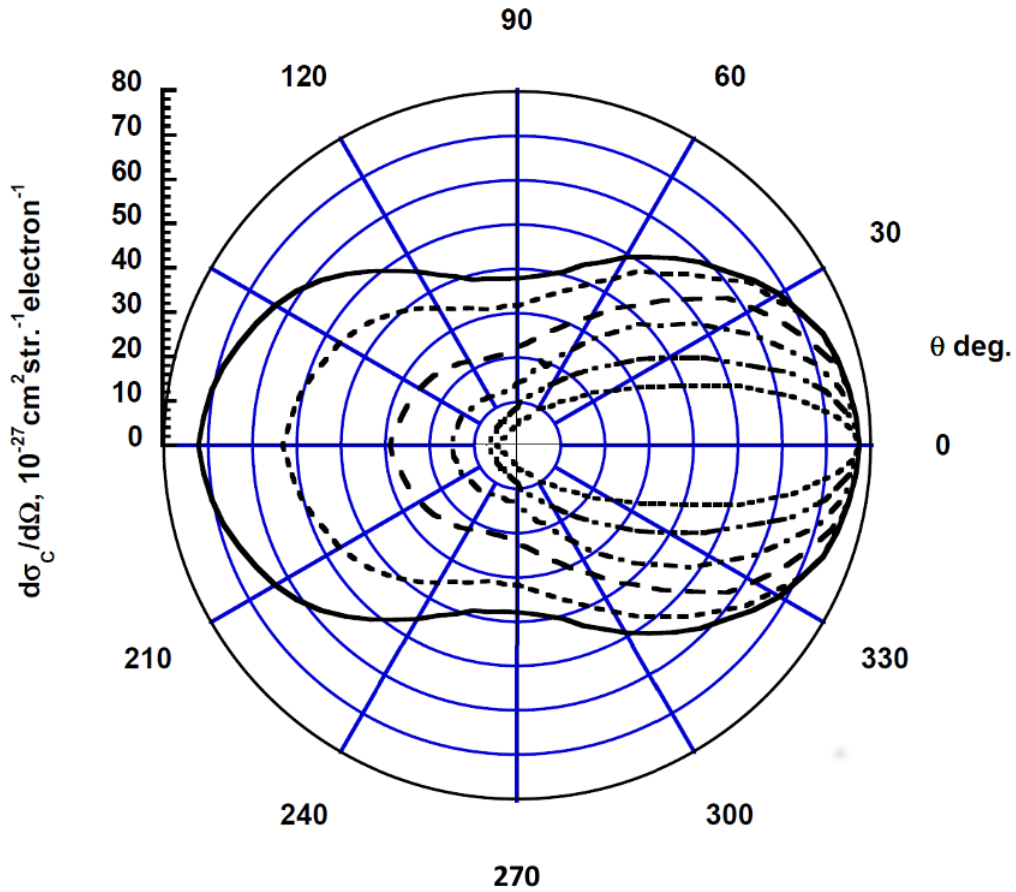


Figure 8. The differential cross-section of Compton scattering. The incident photons move from left to right and the scattering potential is located in the middle of the plot. The curves represent the differential cross-section values for the following energies starting from the outermost curve: 0.01 MeV, 0.016 MeV, 0.2 MeV, 0.5 MeV, 1.2 MeV and 3.0 MeV. Original figure from [29].

The range of validity of Klein-Nishina theory can be broadened by applying corrections in cases when the target electron can not be assumed to be free and at rest. To account for the binding energy of the electron the Klein-Nishina differential cross-section may be multiplied with an incoherent scattering function $S(x, Z)$. Here $x = \sin(\theta/2)/\lambda$ is a momentum-transfer variable and λ is the wavelength of the photon wavelength in units of Ångström (Å). Further, the incoherent scattering function may be generalized to include excited states by defining $S(q, Z)$ where the momentum transfer q is

$$q = \sqrt{k_0^2 + k^2 - 2k_0k \cos \theta}, \quad (45)$$

in units of $m_e c^2$. [30, 26]

2.3.9 Electron-positron pair production

Electron-positron pair production is a process in which a photon disappears and an electron-positron pair of corresponding energy emerges. Like the photoelectric effect, pair production is an absorption-type of interaction that requires the presence of massive body for the conservation of momentum. Thus electron-positron pair production can either take place in the coulomb field of a nucleus or an atomic electron. [13, 31]

The existence of a positively charged electron, positron, was first predicted by Dirac in 1928 who noted that the relativistic wave function for a free electron yielded negative energy states as well as positive energy states [32, 33]. This theoretical prediction was confirmed by Anderson who observed the traces of pair production in his cloud chamber experiments in 1932 and 1933 [34]. [31]

Perrin also suggested the possibility of pair production occurring in the coulomb field of an electron in 1933 [35]. Several cloud chamber experiments were concluded in the following years with descriptions and interpretations of observations but the first photos of the trident signature of triplet production were not published until 1961 by Mohanty et al. and Castor et al. (1970) [36, 37]. [31]

Neglecting the recoil of the nucleus, the conservation of energy and momentum yields a threshold energy E_0^{pair} for pair production in the field of a nucleus

$$E_0^{\text{pair}} \simeq \frac{2m_e c^2}{M c^2} (M c^2) = 2m_e c^2 \approx 1.022 \text{ MeV}, \quad (46)$$

where M is the mass of the nucleus. Respectively in the field of an electron the threshold energy E_0^{trip} for triplet production is

$$E_0^{\text{trip}} = \frac{2m_e c^2}{m_e c^2} (m_e c^2 + m_e c^2) = 4m_e c^2 \approx 2.044 \text{ MeV}. \quad (47)$$

Contrary to most interactions, the standard notation for the pair production cross-section is κ . The probability of a photon to produce an electron positron pair in the

coulomb field of a target-particle is approximately proportional to the square of the target-particle charge. So for the cross-section of pair production in the field of a nucleus κ_n stands

$$\kappa_n \propto Z^2. \quad (48)$$

In the field of an electron which has unit charge the cross-section of triplet production κ_e for a neutral atom with Z electrons is

$$\kappa_e \propto Z. \quad (49)$$

For incident photons with energies far above pair and triplet production energy thresholds, the ratio of the cross-sections then becomes

$$\frac{\kappa_e}{\kappa_n} \simeq \frac{1}{Z}. \quad [31, 26] \quad (50)$$

Many different theoretical models for pair production cross-section have been presented by several authors and groups who have studied the phenomenon in different materials and regions of energy. Also many corrective factors have been developed to improve the existing models to account for effects such as electric-field screening. Other phenomenon to account for include atomic binding of the target electron, indistinguishability of the produced electron and the target electron, retardation in the case of significant recoil velocity of the target electron, the emission of virtual or real photons (radiative corrections) and virtual Compton scattering. [26]

The last comprehensive computations and tabulations of these cross-section values for photon energies from 1 MeV to 100 GeV and target elements from $Z = 1$ to $Z = 100$ were done by Hubbell, Gimm and Øverbø [38]. They developed the following expressions by parsing together many semi-independent models to account for all regions of energy and different corrective factors summing up decades of research. [31]

For the cross-section of pair production in the field of a nucleus κ_n from the threshold energy to 5 MeV the expression is

$$\kappa_n = \kappa_n^{\text{BH}} \left[\kappa_n^{\text{ØMO}} / \kappa_n^{\text{BH}} \right] \left\{ \left[\kappa_n^{\text{BH}} - \Delta \kappa_n^{\text{B}}(\text{scr}) + \Delta \kappa_n^{\text{TP-Ø}}(\text{scr, h.o.}) \right] / \kappa_n^{\text{BH}} \right\} \quad (51)$$

where

- κ_n^{BH} is the Bethe–Heitler unscreened Born approximation cross-section [39] computed using the Maximon expansions [40]
- $\kappa_n^{\text{ØMO}}$ are the Coulomb corrected results of Øverbø et al. [41]
- $\Delta \kappa_n^{\text{B}}(\text{scr})$ is the exact-Born screening correction from an elaborate computation involving the atomic form factor $F(x, Z)$ taken from the relativistic Hartree–Fock compilation of Hubbell and Øverbø [42]

- $\Delta\kappa_n^{\text{TP-}\emptyset}$ (scr, h.o.) are the near-threshold Tseng-Pratt screening corrections [43] including higher-order effects pointed out by Øverbø [44]. [38, 31]

From 5 MeV to 100 GeV the cross-sections were computed according to

$$\kappa_n = \left[\kappa_n^{\text{BH}} \left\{ \left[\kappa_n^{\text{BH}} - \Delta\kappa_n^{\text{B}}(\text{scr}) + \Delta\kappa_n^{\text{TP-}\emptyset}(\text{scr, h.o.}) \right] / \kappa_n^{\text{BH}} \right\} \times \Delta\kappa_n^{\emptyset}(\text{Coul}) \right] [1 + \Delta(\text{rad.corr.})] \quad (52)$$

where

- $\Delta\kappa_n^{\emptyset}(\text{Coul})$ is the Coulomb correction computed from the expressions given by Øverbø [45]
- $\Delta(\text{rad.corr.})$ is the Mork–Olsen radiative correction [46].

The radiative correction term was arbitrarily replaced with a sine function below 10 MeV to prevent unphysical results near the threshold. [38, 31]

For the cross-section of triplet production in the field of an atomic electron κ_e the expression that covers the whole range of energy is

$$\kappa_e = \kappa_e^{\text{BG}} \left[\kappa_e^{\text{H}} / \kappa_e^{\text{BG}} \right] \left\{ \left[\kappa_e^{\text{H}} - \Delta\kappa_e^{\text{BH}}(\text{scr}) \right] / \kappa_e^{\text{H}} \right\} 1.01 \quad (53)$$

where

- κ_e^{BG} is the Borsellino-Ghizzetti unscreened triplet cross section including retardation [47, 48, 49]
- $\kappa_e^{\text{H}} / \kappa_e^{\text{BG}}$ uses the Haug results to include the gamma-electron interaction and exchange effects [50, 51, 52]
- $\Delta\kappa_e^{\text{BH}}(\text{scr})$ screening and electron-binding effects were computed according to the Bethe–Heitler and Wheeler–Lamb expressions [39, 53], using the non-relativistic incoherent scattering functions $S(x, Z)$ compiled by Hubbell et al. [30] from various available sources
- the triplet radiative correction factor 1.01, as advised by Mork [54], is taken as this constant value over the entire energy range. [38, 31]

2.3.10 Rayleigh scattering

In Rayleigh scattering a photon is scattered by the electron cloud of an atom (or some other larger entity) so that the target atom is neither ionized or excited. In comparison to Compton scattering which is a single scattering event between the incident photon and target electron, Rayleigh scattering is a multiple scattering event which means the incident photon scatters many times successively from scattering centers that are grouped together (such as the atomic electrons bound to a nucleus). The photon experiences interference effects between adjacent scattering sites, thus Rayleigh scattering is coherent whereas Compton scattering is incoherent. [26]

Rayleigh scattering was discovered and explained by John William Strutt a.k.a. Lord Rayleigh in a series of publications issued in the late 19th century. [55, 56, 57, 58]

When defining the scattering potential for Rayleigh scattering, the charge distribution of all atomic electrons must be considered at once. This can be done approximately by introducing an atomic form factor $[F(q, Z)]$ based on an atomic model such as Thomas-Fermi, Hartree or similar models. The square of the form factor $[F(q, Z)]^2$ gives the probability with which the Z atomic electrons gain a recoil momentum q without absorbing any energy. In case of negligible energy transfer the assumption $k - k_0 = 0$ is valid and the momentum transfer q of equation 45 reduces to

$$q \approx 2k \sin \frac{\theta}{2} \quad [26]. \quad (54)$$

Combining the low-energy limiting form of the Klein-Nishina differential cross-section with the probability $[F(q, Z)]^2$ gives the differential Rayleigh scattering cross-section $D^R(\theta)$ for unpolarized photons

$$D^R(\theta) = \frac{r_0^2}{2} (1 + \cos^2(\theta)) [F(q, Z)]^2. \quad [26] \quad (55)$$

2.3.11 Relaxation

Many of the interactions discussed in the previous sections may result in the excitation of an atom. An atom is in an excited state whenever one of its electrons has enough energy to move to a (sub)shell of higher energy which is a state with one or more quantum numbers differing from the possible minimum.

Atomic excitation may happen when an atomic electron absorbs sufficient energy to move to a higher state, but not enough to leave the atom. Excitation results also from ionization whenever an inner shell electron is removed from the atom. In both cases an inner shell vacancy is created and the excitation is soon followed by a de-excitation on relaxation, in which the atom returns to its ground state by giving up its excess energy. The relaxation can occur in three different ways.

Firstly, an outer shell electron can fill in the vacancy with the atom emitting a photon with energy equal to the difference between the electron's initial and final state. This is known as X-ray fluorescence and photons emitted this way are known as characteristic X-rays, as the spectrum of possible emitted photon frequencies (energies) is unique to each element. [59, 60, 61]

Secondly, instead of a photon the excess energy of the vacancy filling electron may cause the atom to eject an outer-shell electron from the atom. This is known as the Auger effect and free electrons of such origin are known as Auger electrons. [62]

Thirdly, in a special case of the Auger effect the vacancy can be filled in by an electron from a higher subshell resulting in a new vacancy. The newly created vacancy can be filled with any of the mechanisms described here. This process is known as a Coster-Kronig transition. [63]

By labeling the fractions of relaxation processes that occur in each way as ω for the fluorescence-yield, a for Auger yield and f for Coster-Kronig yield, one may write

$$\omega + a + f = 1. \quad (56)$$

Figure 9 shows the yields for fluorescence, Auger effect and Coster-Kronig transition after the K-, L₁-, L₂-, and L₃- photoelectric effect. [64]

2.3.12 Photonuclear giant dipole resonance

In addition to the electromagnetic interactions that govern the energy loss of electrons and photons propagating in matter, special attention must also be paid to photonuclear absorption. Photonuclear absorption includes a series of nuclear interactions induced by the absorption of a photon by a nucleus.

The most characteristic feature of the cross-section for photonuclear absorption is known as giant resonance, which is a high frequency collective excitation of atomic nuclei. The excited nuclei may de-excite in a number of ways. Possible outcomes of this effect include the emission of one or more neutrons, charged particles, gamma rays, or nuclear fission (only in heavy elements). Of these, the emission of a single neutron is most typical. [26]

Giant resonance includes giant monopole resonance (GMR), giant dipole resonance (GDR), and giant quadrupole resonance (GQR), of which GDR is the dominant effect in this context. GDR occurs when excess energy absorbed by the nucleus causes the the charges in the nucleus to separate. All the protons and all the neutrons of the nucleus oscillate with opposite phases creating a large time-varying electric dipole-moment. [65]

The importance of GDR is due to several reasons. The cross-section of GDR is centered around 24 MeV for light nuclei and it shifts towards lower energies to about 12 MeV for the heaviest stable nuclei. The highest photon energies present in this study are about 24 MeV, thus the emission of neutrons is probable for all materials present in this study. The energy range of incident photons capable of initiating GDR can be described by threshold energies and full width half maximum (FWHM) values Γ which are the differences in energy between the points where the GDR cross-section is half of it's maximum value. [26]

The emitted neutrons are likely to be far more penetrating than the incident photons. This is a concern when planning the shielding of the experiment site. Several studies

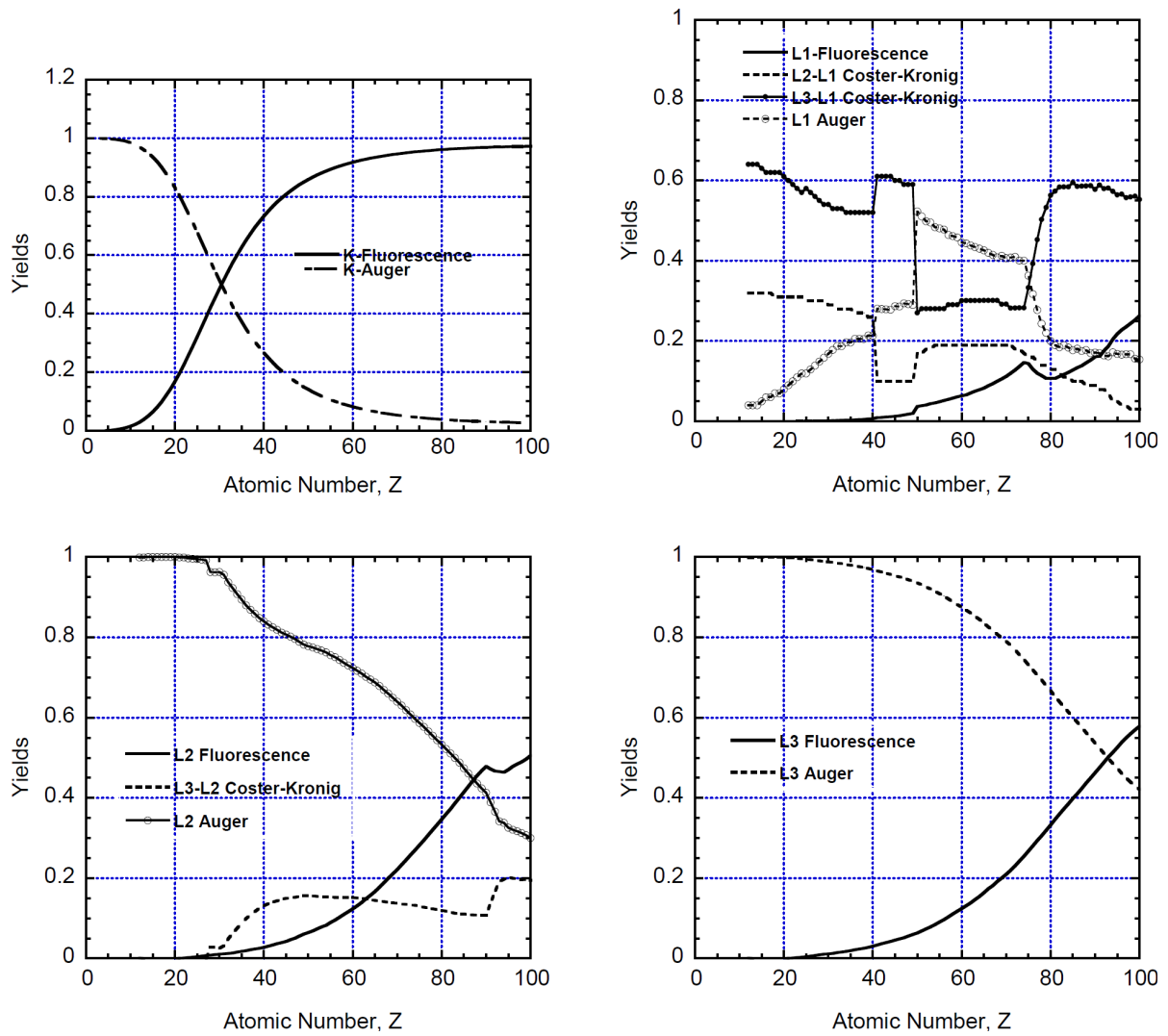


Figure 9. Yields of different relaxation processes after K-, L_1 -, L_2 -, and L_3 -photoelectric effect. Figure obtained from the 8th edition of Table of Isotopes [64].

have pointed out and studied the photoneutron contamination problem regarding the use of Varian Clinac 2100 C/D and patient safety e.g. [66, 67, 68].

Neutron radiation is indirectly ionizing. While the electrically neutral neutron does not cause forces on charged particles of atoms, it may be absorbed by a nucleus causing the nucleus to excite and emit more ionizing gamma radiation. Neutron interactions may also result in recoiling ions which go on to produce more ions, free electrons and photons. In this experimental set up no living subjects are exposed to the beam of the accelerator, but the composition of the beam has high information value when analyzing the effects of the beam on the radiated test piece.

Let the peak value of GDR cross-section be σ_0 and let the corresponding incident photon energy be E_0 . Then, by noting the FWHM energy gap as Γ , the GDR cross-section, which equals the photonuclear absorption cross-section $\sigma_{\text{ph.n.}}$ may be reconstructed as

$$\sigma_{\text{ph. n.}}(E) \approx \sigma_0 \frac{E^2 \Gamma^2}{(E_0^2 - E^2) + E^2 \Gamma^2}. \quad (57)$$

This is done assuming the GDR cross-section has the shape of a Lorenz line [26].

Table 2 gives these parameters for a number of representative nuclei through out the periodic table, some of which are also of special interest to this study (^{27}Al , ^{181}Ta , ^{208}Pb). The GDR cross-section is isotopically dependent and the elements present in this study are composed of different isotopes according to their natural abundance, so these values are not directly applicable for the materials in the accelerator head but they serve as a fairly good approximation.

A closer inspection of the GDR cross-section peak reveals it has an inner fine-structure. For nuclei with large permanent deformations the peak is actually split in two. Some nuclei also have large “dynamic deformations” due to the vibrational nature of the nuclear ground state. Generally both type of deformations cause the nuclei to have their GDR cross-sections spread over a wider range of energy, thus they have a larger FWHM value. Depending on the individual properties of a nucleus, the value varies from 3 MeV to 9 MeV. [26]

GDR can also result from other interactions than photonuclear absorption. In fact any process capable of delivering the required energy to a nucleus can induce GDR. However, for an electron to deliver the required energy via a collision, the initial energy of the electron has to exceed 50 MeV. Thus all GDR events in this context are of photonuclear origin.

Table 2. Photonuclear giant resonance cross section parameters supplied by J.H. Hubbell [26] via E.G.Fuller who gathered the data from various sources given in the table.

Nucleus	Threshold energies (MeV)		E_0 , energy at $\sigma_{\text{ph. n.}}$ peak (MeV)	σ_0 , value of $\sigma_{\text{ph. n.}}$ at peak (b/atom)	Γ , peak width at half maximum (MeV)	Percent of "elec-tronic" cross-section at E_0 (%)	Refs
	(γ ,n)	(γ ,p)					
^{12}C	18.7	16.0	23	0.018	3.6	5.9	[69]
^{27}Al	13.1	8.3	21.5	0.038	9.0	3.9	[70]
^{40}Ca	15.7	8.3	20.5	0.100	4.5	5.2	[71]
^{63}Cu	10.8	6.1	17.0	0.070	8.0	2.0	[72]
^{90}Zr	12.0	8.4	17.0	0.180	4.5	3.0	[73]
^{127}I	9.1	6.2	15.2	0.210	5.7	2.3	[74]
^{165}Ho	8.0	6.1	14.0	0.220	8.5	1.7	[75]
^{181}Ta	7.6	6.2	14.0	0.280	6.5	1.8	[76]
^{208}Pb	7.4	8.0	13.6	0.495	3.8	2.7	[77]
^{235}U	6.1	7.6	12.2	0.500	7.0	2.4	[78]

2.3.13 Mass attenuation and energy absorption coefficients

The individual interactions relevant to a photon propagating in matter have now been discussed separately. Let us now consider a photon propagating in matter. The total cross-section σ_{tot} for the photon to undergo any interaction is the sum of the individual cross-sections for given photon energy,

$$\sigma_{\text{tot}} = \sigma_{\text{p.e.}} + \sigma_C^{KN} Z + \kappa_n + \kappa_e + \sigma_R + \sigma_{\text{ph.n.}} \quad (58)$$

Here all the other cross-sections have been defined in units of barn/atom, but the Klein-Nishina formula gives the cross-section in barn/electron. Thus the Compton scattering cross-section is multiplied with the target material's atomic number Z . [79, 13]

The mass attenuation coefficient μ describes how a beam of photons loses energy as it passes through a layer of matter. It is a measure of the average number of interactions between incident photons and matter that occur in a given mass-per-unit-area thickness of material encountered. The experimental definition of μ is obtained from a setup where a monoenergetic beam of photons with intensity I_0 passes through a layer of material of thickness x . After passing through the material the beam intensity I is measured. The fractional loss in intensity in crossing any

thickness dx of material is

$$\frac{dI}{I} = -\mu/\rho dx, \quad (59)$$

and thus, for a homogenous material, the photon beam gets attenuated according to the exponential absorption law

$$I/I_0 = e^{-\mu x/\rho}, \quad (60)$$

where ρ is the density of the material. [79, 26, 13]

For more complex situations photon attenuation is still exponential, but it may be modified with a geometrical factor to account for the source geometry and a build-up factor to account for the secondary photons produced in the absorber [26].

The attenuation of a photon beam in a given material is directly related to the probability of interactions that remove photons from the beam σ_{tot} . The theoretical value of μ is then defined as

$$\mu/\rho = \sigma_{\text{tot}} \frac{N_A}{uA}, \quad (61)$$

where N_A is Avogadro's number, u is the atomic mass unit and A is the relative atomic mass of the target element.

The mass energy absorption coefficient μ_{en} is a measure of the average fractional amount of incident photon energy transferred to kinetic energy of charged particles as a result of different photon interactions. This energy approximately equals the energy that has the capacity to produce chemical and biological changes and other significant radiation effects in the target. [79]

The coefficient μ_{en} is closely related to other similar variables frequently used in dosimetric calculations. The coefficient μ_{en} relates to the mass energy-transfer coefficient μ_{tr} as

$$\mu_{\text{en}} = \mu_{\text{tr}}(1 - g) \quad (62)$$

where g is the fraction of charged particle kinetic energy lost due to bremsstrahlung. Further, μ_{tr}/ρ multiplied with the photon energy fluence $\psi = \phi h\nu$ (where ϕ is the photon fluence) gives the dosimetric quantity *kerma*. Kerma is the sum of the kinetic charged particle energies released by uncharged particles (here photons) per unit mass [80]. [79]

The mass energy absorption coefficient μ_{en} is useful in a variety of situations for estimating the absorbed dose D , but its applicability is limited to low-energy calculations with $E_e \sim h\nu \lesssim 2$ MeV. This is because using it assumes that photons have significantly larger ranges than electrons of the same kinetic energies. This assumption fails for higher energies. [79]

The most recent compilations of the mass attenuation and energy-absorption coefficients are those of J.H. Hubbell [81].

2.3.14 Electromagnetic cascade

When the energetic electron-gamma beam is incident on a thick absorber, such as the phantom placed in front of the accelerator, it initiates an electromagnetic cascade where new electrons, photons and other particles of lower energy are produced through the many interactions described in the previous sections.

Mostly new photons are generated as bremsstrahlung of high energy electrons and new electrons and positrons are generated in pair production events of high energy photons. When electron energies fall below the critical energy, ionization and excitation events start to govern their energy loss. [22]

Even though the energy loss of the electron-gamma beam is mainly governed by these few processes, energy is converted back and forth to many different forms in the cascade. To summarize this discussion about interactions of radiation and matter, figure 10 shows a flow diagram of the different forms of energy and the transformation processes between them. It is worth noting that photons have no direct energy deposition mechanisms. However, they have the capability to induce several types of reactions that can lead to permanent changes in the medium.

2.4 Varian Clinac 2100 C/D

Varian Clinac 2100 C/D is a linear electron accelerator originally designed for radiation therapy by Varian medical systems. The accelerator produces pulsed electron beams which can be degraded to pulsed photon beams by changing the accelerator's operation mode. Switching between different operation modes is done by changing the instruments in the accelerator head which modify the incident beam.

The nominal energies of different electron beams are 6, 9, 12, 16 and 20 MeV. For photons a continuous spectrum up to 6 MeV with a peak around 1 MeV and a continuous spectrum up to 15 MeV with a peak around 2 MeV can be generated.

The accelerator is able to give a maximum beam area of 30 cm times 30 cm at 100 cm source to surface distance (SSD). Multiple times larger beam areas can be generated by increasing the SSD distance but this comes with increased uncertainties in the beam parameters. Also dose rates decrease as the energy of the beam is distributed over a wider area.

The dose rates of different beams have been measured with water phantoms at the depth of maximum dose deposition. For electron beams these values vary from 1 Gy/min to 10 Gy/min and for photons from 1 Gy/min to 6 Gy/min. The dose deposition profiles vary depending on the beam and target type.

With maximum dose rate, the source beam of the accelerator is produced as a series 5 μ s beam pulses with a period of 5 ms corresponding to a duty cycle of 0.1 %. For lower dose rates, individual pulses are left out of the cycle.

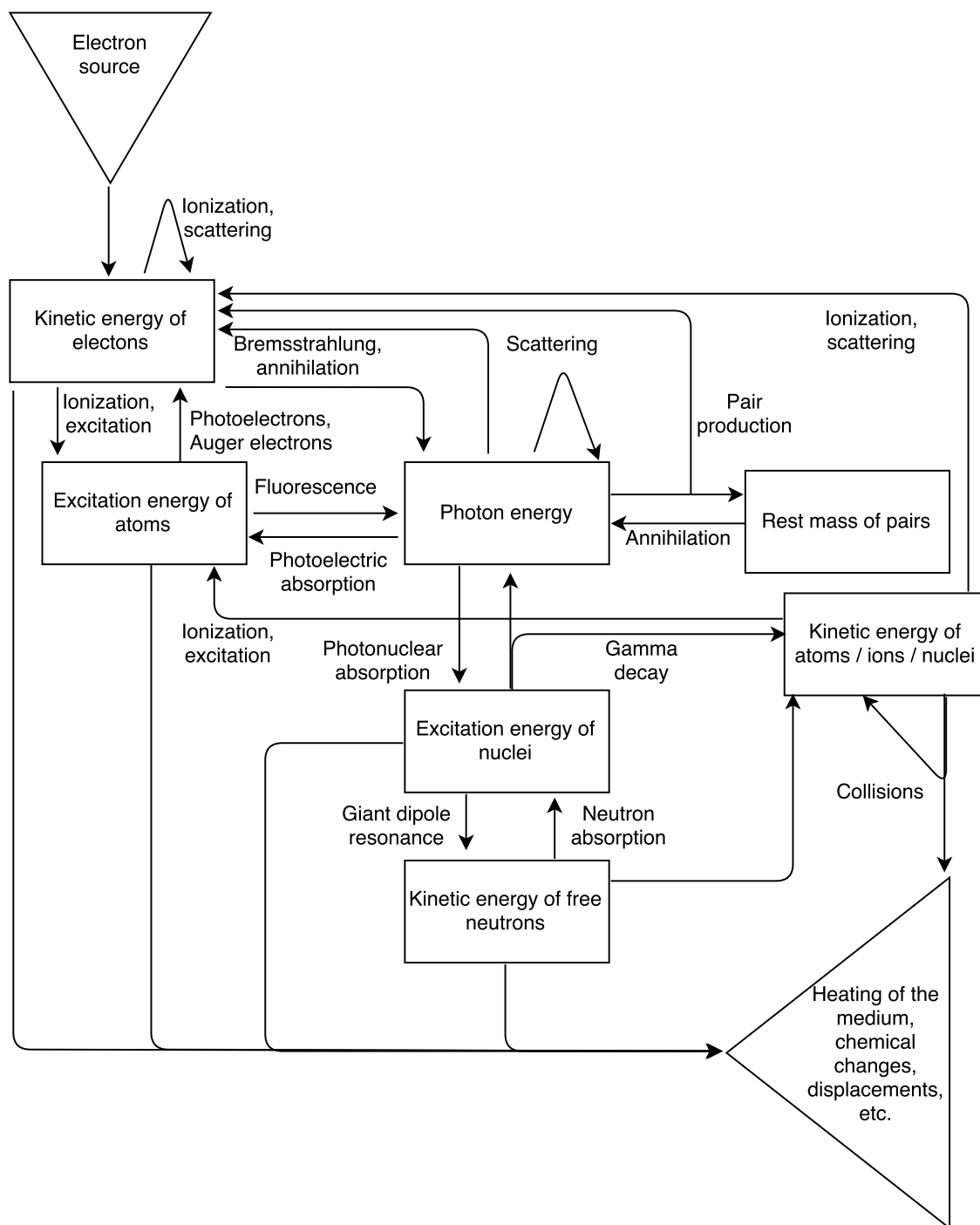


Figure 10. A flow diagram of the energy conversions taking place in the electromagnetic cascade. In addition to electromagnetic interactions, hadronic processes such as photonuclear interactions and interactions with free neutrons have been included.

2.5 Beam formation in the linear accelerator head

A schematic diagram of the modeled accelerator head geometry is presented in figure 11. All modeled parts are included in this figure but their shapes, relative sizes and positioning does not correspond with reality or the actual computer model.

In reality, the primary collimator is responsible for shaping the initial electron and gamma beams. It composes of two thick cylinders made of a high- Z material, in this case tungsten. In the middle of the first cylinder is a narrow cylindrical canal which determines the shape of the source beam. Inside the second cylinder is a cone shaped opening which allows for the source beam to become moderately wider as it is collimated to its initial shape.

In photon mode, the target with which the source electron beam is turned to an initial gamma beam is placed inside the primary collimator. In this case the primary collimator shapes the initial gamma beam. For the electron mode simulation, the primary collimator is of minor importance, because the shape of the source electron beam is determined by the computed electron source in the simulation. The source electron beam exits the primary collimator through a beryllium window.

After the primary collimator come the scattering foils which can justifiably be labeled as the most critical individual structure of the simulation model. The foils are responsible for the spatial, angular and the energy distribution of the beam.

The source electron beam hits the first scattering foil which is a flat tantalum piece of uniform thickness. Through the collisions and scattering events that take place in the foil the sharp incident electron beam is broadened into a Gaussian shape. [82]

As a material tantalum is dense and has a high atomic number ($Z = 73$), thus the primary scattering foil is dense with loosely bound electrons that can be scattered away efficiently. These types of materials make the best primary scattering foils producing less bremsstrahlung and causing minimal electron energy loss. [82]

Immediately after the first scattering foil, the broadened beam hits the secondary scattering foil designed to reduce the intensity of the central region of the beam to make the spatial distribution of the outgoing beam uniform. This means that the particle flux becomes constant in different areas of the beam. [82]

Low Z elements are employed for efficient intensity reduction. In this case the secondary foil is made of aluminum ($Z = 13$). The shape of the secondary foil is roughly Gaussian as it's made of overlaid disks of increasing radius. This way the electrons at the central area of the broadened beam are subjected to more scattering events than the electrons further from the center. Thus the higher electron density in the central area of the broadened beam is spread evenly over the whole beam area forming a homogeneous outgoing beam of uniform intensity. [82]

After the secondary foil the spatial, angular and energy distribution of the beam are very close to that of the outgoing beam. Hence an ionization chamber used for

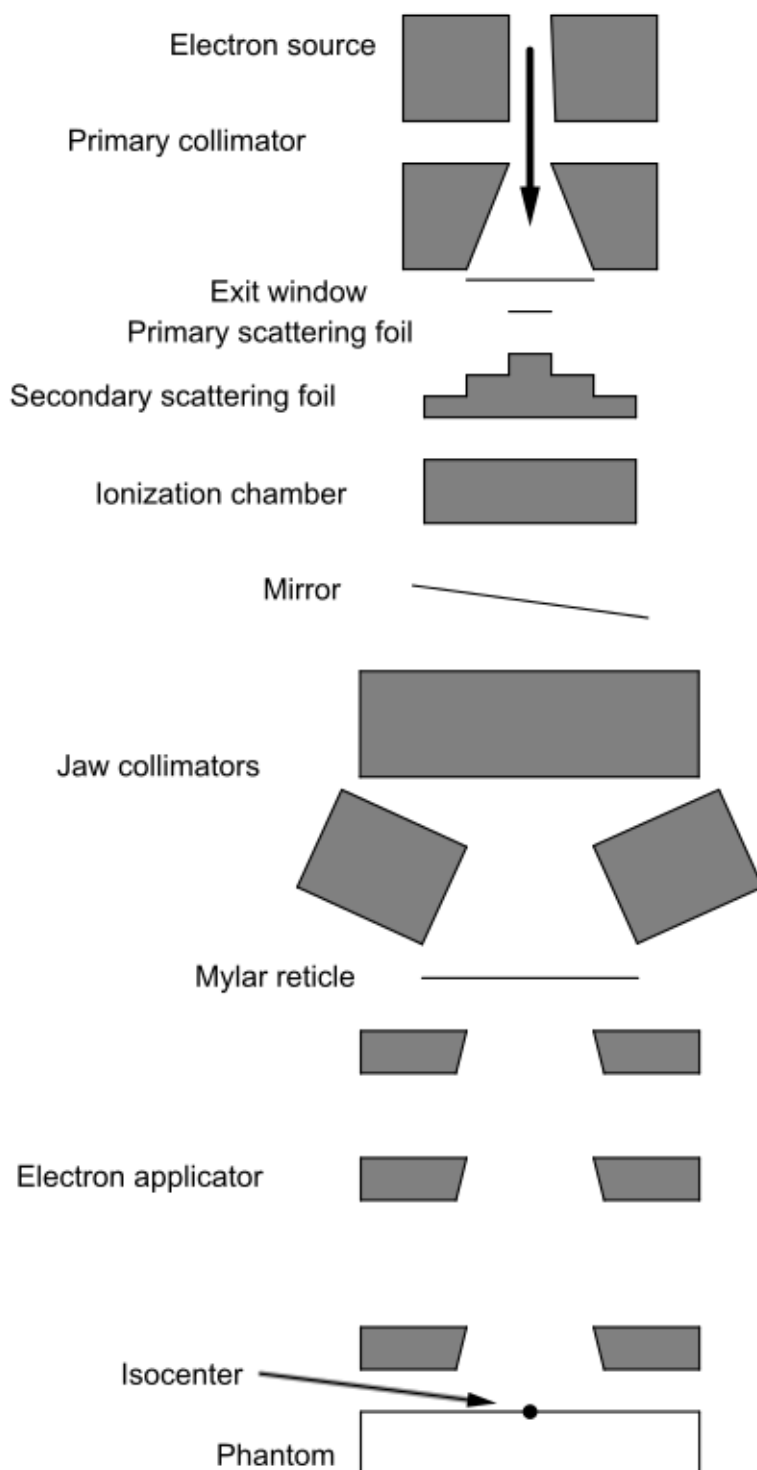


Figure 11. A schematic diagram of the modeled accelerator head geometry for a 20 MeV electron beam.

beam monitoring is placed after the second scattering foil. Like any measurement device, the monitor chamber is designed to have as little impact on the beam as possible. The monitor chamber is a multi-cavity parallel plate ionization chamber which continuously measures the beam intensity in over multiple regions. It provides information about the symmetry and flatness of the beam. To model the essential effect of the ionization chamber on the beam, the chamber is modeled as 6 thin stacked plates made of kapton polyimide film.

The mirror is effectively a thin aluminized mylar piece used to adjust the settings of the accelerator outside of operational time. It has no purpose in shaping the beam and is designed to interfere with it as little as possible.

The jaw collimators are adjustable thick steel blocks used for rough shaping of the outgoing beam. With the jaw collimators the geometrical cross-section of the beam can be shaped to a desired rectangular form. The jaws move on a concavely curved track respect to the isocenter of the accelerator so that the particle absorbing surfaces of the jaws are set perpendicular to the broadened beam.

The beam exits the accelerator head through a thin reticle with an imprinted cross pattern used to adjust the center of the beam. The reticle is made of mylar film.

Finally after exiting the actual accelerator head structure, the shape of the beam is fine tuned with an applicator which in this case is a separate metal frame with three filtering plates that have fine octagonal apertures that open out very subtly. Different kinds of applicators can be utilized to create beams of different shapes and sizes. For this computer model, two octagonal applicators were implemented which create beams of square cross-sections with side lengths of 10 cm and 20 cm. In the bottom plate of the applicator, an insertable lead block is placed to give the beam its final form.

2.6 Geant4

Geant4 is a widely applicable simulation toolkit for the interaction of radiation with matter. The concept “toolkit” implies that a Geant4 simulation is a program code written by the user utilizing the components provided by Geant4 in addition to hers/his own. Geant4 is a result of project RD44 in which two research groups under the facilities of CERN in Switzerland and KEK in Japan began collaborating for a research both groups had worked on independently before. They both were trying to find out how modern computation techniques could improve the existing Geant3 program. The goal of RD44 actualized to be the creation of an object-oriented simulation program. About 100 scientists from over 40 institutes and research groups from 15 different countries contributed to the research and development work. The first version was published in December 1998 after which the development has happened under Geant4 Collaboration which a worldwide organization bringing physicists and software engineers together. [2, 4]

The functionality of Geant4 can be divided into 17 upper categories. The categories and their dependencies have been illustrated in figure 12. The dependencies are uni-directional so that the upper categories depend on the lower ones according to the drawn connections. For example the lowest category Global of which all the other categories depend covers the system of units, constants, numerics and handling of random numbers. [2]

The source code of Geant4 is very large and complex in it's advanced abilities and optimized design. Explaining it's full functionality is beyond the scope of this work. The focus of this work is explaining the features of the created simulation in terms of the user who is interested in it's physics. Therefore only the categories most important for understanding the simulated physics are explained in more detail later in this section. However, to a certain degree the physics models of the simulation are bound to the computation and programming techniques used and it is impossible to fully distinguish between them. Therefore the basic methodology and working principles of Geant4 are first gone through.

2.6.1 Object-oriented programming

Object-oriented programming refers to a programming approach in which the description and solution of a problem is based on mutually interacting data structures called objects. An object contains data and procedures. Traditionally a procedural program code is a logical list of commands given for the computer to execute. In an object-oriented program the logic is decentralized into contents of objects and their interrelations. In an object-oriented program each object is responsible of a certain part of the program. [83][84]

Geant4 has been implemented with C++ programming language so it follows the principles, syntax and semantics of C++. In addition to objects the most important object-oriented concepts of C++ regarding Geant4 are classes, inheritance, and encapsulation.

A class is a definition for the data and procedures a group of objects contain. A class does not contain any data or procedures itself but merely describes what the objects of that class are like.

Inheritance is feature with which new classes can be defined on the basis of existing classes. An inherited class can be defined to contain new data and procedures in addition to the ones it has inherited from it's base class.

Encapsulation refers to gathering data and the procedures manipulating that data into the same unit, that is an object. This way data is secured and handled in entities of manageable size.

Also the concepts of data hiding and abstraction are closely related to encapsulation. Data hiding prevents the access to an object's data from the outside. This reduces the amount of possible mistakes remarkably. Data abstraction is about making

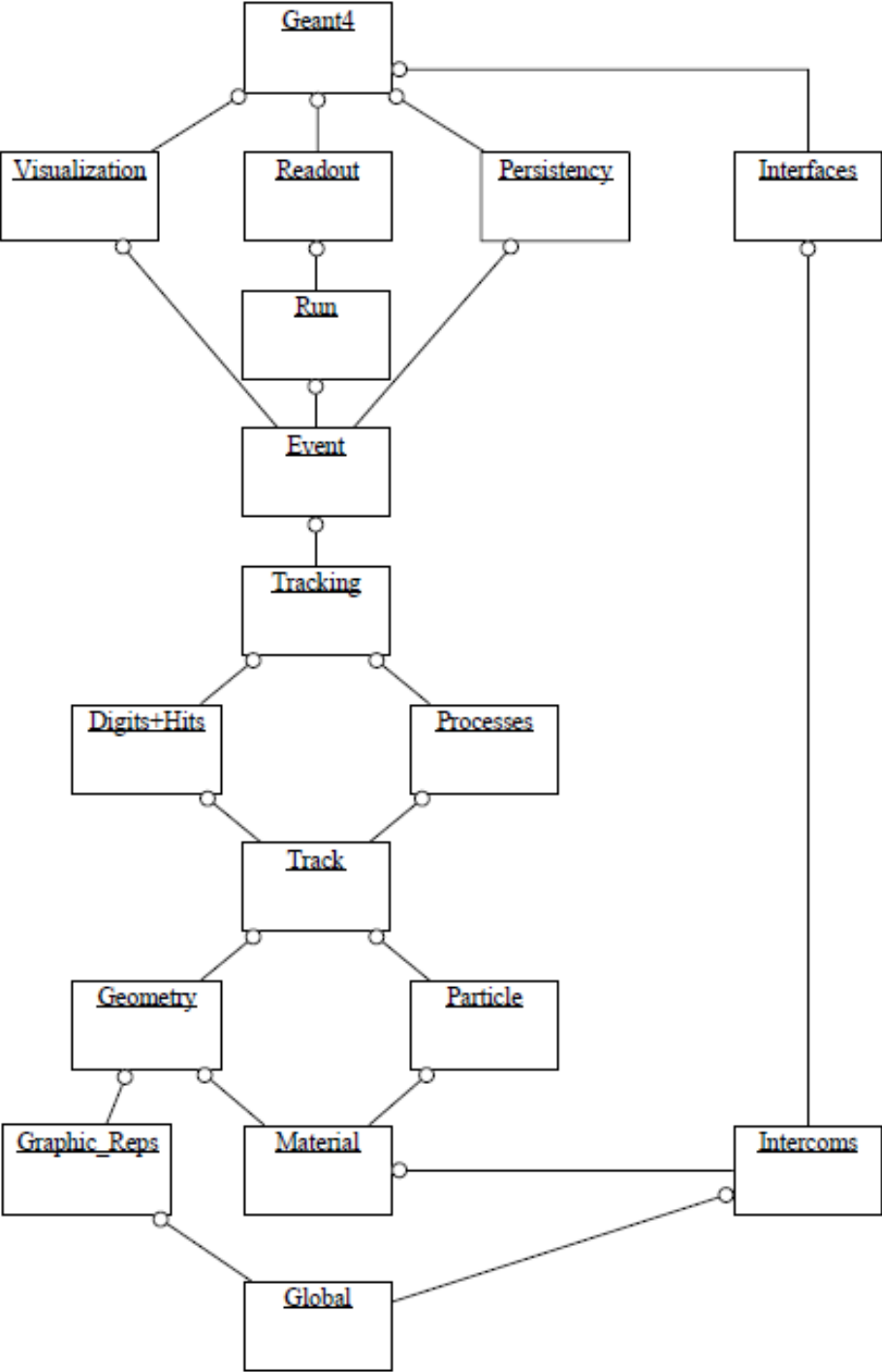


Figure 12. A category map of the functionality of Geant4. [2]

the management of entities easier by hiding the details about an object's contents behind an interface so that the coder only has to know what data the object needs to operate and what kind of data it produces. [83] [84] [85]

2.6.2 Geometry, materials, particles and tracks

The geometry of any solid body in Geant4 is defined as it's own object, a solid. Geant4 has classes for all the typical shapes such as rectangular boxes, circular cylinders and cones. A solid may be defined in a number of ways depending on it's complexity. However, all solids are objects of classes that have been inherited from a base class G4VSolid. For any solid a shape and dimensions are defined. [2]

A solid is used to define a logical volume. An object of the class G4LogicalVolume takes a predefined solid as an argument and fills the defined volume with material that it takes as another argument. A logical volume is abstraction which has no physical placement. Instead an object of class G4PVPlacement is a physical volume which comprises of a logical volume and position and direction data given to it as arguments. [2]

In nature materials comprise of atoms of one or more elements. Elements on their part comprise of different isotopes in a ratio defined by natural abundance. Respectively in Geant4 an object of class G4Material "comprises" of objects of G4Element which again has data of it's own isotope ratios in terms of objects of G4Isotope class.

All particles in Geant4 are based on the G4ParticleDefinition class. Using inheritance a set of virtual intermediate classes for leptons, bosons, mesons, baryons etc. is derived from this base class. These virtual classes serve as base classes for concrete particle classes such as G4Electron and G4Proton. Both categories Geometry and Particle use data provided by the material category and together they define how a particle propagates in a given medium in the track category.

2.6.3 Hits, digits and steps

A hit represents a physical interaction or an accumulation of interactions of a track or tracks in a detector component that has been set sensitive. A digit is a user determined detector output that is created from hits and/or other digits. The quantities of interest and the way to describe a sensitive detector change from application to another. Thus the information held in hits and digits varies greatly. In general this information can be

- the position and time of the step,
- the momentum and energy of the track,
- the energy deposition of the step,

- geometrical information.

In Geant4 particles are moved in steps. The transportation of particles is treated as a process similar to physics processes and is therefore handled by the processes category. In contrast to considering particles self moving, this approach has been chosen to improve the overall performance of the simulation which is critically dependent on the CPU time spent on moving a particle by one step. The step length is controlled by the simulated physics processes and a limit set by the user. The tracking category steers the invocation of processes. [2]

The hit objects are constructed by a sensitive detector. `G4VSensitiveDetector` is an abstract class which represents a detector. It uses the information gathered in objects of `G4Step` class and objects of `G4TouchableHistory` class to construct one or more objects of `G4VHit` class for each step with meaningful information in it.

`G4TouchableHistory` objects are constructed by the `G4VReadoutGeometry` base class which also passes them to the sensitive detector. The sensitive detector does not need the `G4TouchableHistory` objects to construct hits, but they can be used to store more information to hits than can be extracted from `G4Step` objects alone.

2.6.4 Tracking

Classes of many different categories participate the tracking of a particle. A singleton object of the class `G4TrackingManager` passes messages between the event, tracking and track categories. A singleton object of the class `G4SteppingManager` passes messages between categories that are related to particle propagation in matter, such as geometry, processes and particle. It handles objects of class `G4Track` which represent particles. These objects hold external data regarding particles and specific to each step such as current position, the identification of the geometrical volume where the particle is etc. The dynamic and static data of the particle itself are held through pointers to objects of classes `G4DynamicParticle` and `G4ParticleDefinition` respectively. The state of the particle is stored in an object of class `G4TrajectoryPoint` at the end of each step and these objects are aggregated by a `G4Trajectory` object to form the trajectory of the particle. [2]

2.6.5 Physics processes

The physics processes in Geant4 have been divided into seven sub-categories. These are electromagnetic, hadronic, transportation, decay, optical, `photon_hadron` and parametrisation. The categories electromagnetic and hadronic are further divided in to sub-categories of their own. Again, using the inheritance of C++ all processes are derived from the base class `G4VProcess`. The design of physics processes category is based on the ideas of transparency and continuous development without affecting the previous code. [2][19]

As already mentioned, each of the simulated physics processes proposes a step length. The shortest of these is chosen to govern the step length of all processes in order to preserve precision in a situation where the energy of a particle is changing along a step. Depending on the real nature of the process that is being simulated, the simulation model of the process is set to have one or more of the following characteristic actions handled by the tracking category: at rest, along step and post step. A particle at rest may for example go through radioactive decay. In this case the proposed step is a time rather than a length. Along step -processes represent “continuous” such as energy loss or secondary particle production. They take place cumulatively along a step. Post step -processes represent processes like secondary particle production by an interaction or decay. They are invoked at the end of each step. [2]

An object which encapsulates the data and methods required for calculating total cross-sections for a given process in a certain range of validity is referred to as an cross-section data set. Each process includes a list of these data sets. The concrete data set classes are derived from the abstract base class `G4VCrossSectionDataSet`. This class includes declarations for methods that inquire whether a data set is applicable in the given conditions. The implementation depends on the conditions. It may be a simple formula, a sophisticated parametrisation or evaluated data. The calculation of the actual cross-section using the chosen data set is delegated to the method `GetCrossSection`. [2]

The physics processes of a particle are managed by an object of `G4ProcessManager` class. All the simulated processes have to be registered with it. The `G4ProcessManager` object can be used to add new processes to the simulation as well as to activate and inactivate them. For all Geant4 applications the application developer must define the physics by deriving her/his own class from the base class `G4UserPhysicsList` in which all the particles and processes of the simulation must be registered. The desired physics processes can be added as single processes, Geant4’s own physics libraries or as pre-packed physics lists designed for certain types of applications.

2.6.6 Events and runs

An event is the basic unit of Geant4 simulation. It holds the information regarding a primary particle from being generated to losing all its kinetic energy or leaving the simulation volume. More precisely the objects of class `G4Event` contain the primary vertices and primary particles before processing the event. After processing they hold the hits and digitizations generated and optionally the trajectories of the simulated particles. It is these objects that are passed down the program chain for further analysis. A run is a sequence of events.

3 Methods

3.1 A Geant4 application for Varian Clinac 2100 C/D

3.1.1 Features of the application

This work is part of a larger project to develop a functioning simulation code for Varian Clinac 2100 C/D accelerator for RADEF of JYU. The work documented here continues on previous work of Lahti [1].

The Varian application source code is based on a readily written Geant4 example called MedLinac2 by Claudio Andenna and Barbara Caccia. To save time and effort in the code writing process this approach was chosen instead of writing the simulation model from scratch. The decision was justified by the original authors' documentation which stated: "The example is based on a typical structure of a medical linear accelerator for Intensity Modulated Radiation Therapy (IMRT), such as Varian Clinac 2100 accelerator".

Varian Clinac 2100 C/D accelerator has several different operational modes for electron and photon beams of different energies. Acknowledging this, the approach chosen for the development of the Varian application was to create a user-friendly application that flexibly allows the development of additional features.

However, the Geant4 example MedLinac 2 on which the source code of Varian was based on, was not developed with this approach. The example provided a linear accelerator operating in 6 MeV photon mode and 3 optional phantoms. Because the example provided only one operational mode, many features regarding the operation of the accelerator were hard coded and were not designed to be changed. Thus a significant part of the development work of the Varian application was to add the required flexibility to the original source code to allow for moving and changing of different accelerator parts to construct different operational modes. Visualizing any changes made in real time was also considered a priority from the perspective of usability.

In the previous phase of this project the 6 MeV photon mode accelerator was placed inside a model of the accelerator chamber of RADEF. Also many user-friendly features were added and the real time visualization of the modifications was implemented. Though no new accelerator parts were created then, the possibility to move, place and remove any mobile parts was also implemented. The reader should

see [1] for a more detailed description of the previous steps of the development process.

For this study, the parts and features necessary to simulate the operation of the accelerator in 20 MeV electron mode were designed and implemented. Thanks to the approach chosen in the beginning of this project and the ground work done in the previous phase, implementing the additional features was now much more convenient.

By the time of the publication of this thesis the Varian application has controls for

- moving the accelerator along all dimensions
- moving the chosen phantom along all dimensions
- moving the jaw collimators along a curved track defined by the isocenter distance
- placing and removing the mylar reticle
- placing and removing the 20 MeV dual scattering foils (electron mode)
- placing and removing an applicator for 10 cm \times 10 cm square beam (electron mode)
- placing and removing an applicator for 20 cm \times 20 cm square beam (electron mode)
- moving the collimator leaves along one axis (photon mode)
- placing and removing the target (photon mode)
- placing and removing the flattening filter (photon mode)
- rotating the accelerator in two different planes
- setting the isocenter distance value
- setting the mean energy of the primary particles
- setting the standard deviation of the energy of the primary particles
- setting the number of primary particles generated
- setting the number of identical primary particles generated
- setting the initial beam radius
- setting the size of the phase space plane (only on application start-up)
- setting the coordinates of the phase space plane (only on application start-up)
- switching between 3 phantoms: a water container, a silicon block and a small silicon chip (only on application start-up)
- selecting the simulated physics processes

- controlling all possible output files
- switching between visualization modes.

From now on, further development of other operational modes requires only implementing the models for scattering foils, flattening filters, and targets of given energies. New applicators can also be implemented for different beam shapes.

3.1.2 Modeling the electron beam

Largely based on the readily written code of the Geant4 example ML2, a class called `VarianPrimaryGenerationAction` was written to control the production of primary particles. Along the lines of the example, it provides the possibility to generate primary particles randomly by utilizing the `G4ParticleGun` class and by using a readily calculated phase space file with information about particle types, positions, energies, momentum directions and types of the primary particles that produced the particles hitting the plane. In this study, only the random particle source was used.

With its own messenger class, commands can be passed to `VarianPrimaryGenerationAction`. Using these commands, the incident beam was set to have a radius of 0.5 mm.

Information about the outgoing beam was collected with the phase space plane that was placed on the surface of the phantom. Using the phase space data the energy of the incident beam was calibrated. The energy of the beam was set so that the fractional energy of outgoing electrons reached its maximum value at 20 MeV with 1% accuracy.

3.1.3 Modeling the accelerator head geometry

The parts of the accelerator head modeled in this study are shown in figure 11 and an OpenGL runtime visualization of the accelerator is shown in figure 13. The choice of parts and their materials and shapes was based on information about other simulation models of similar linear accelerators. A thorough tabulation of the accelerator geometry including the positioning, shapes and sizes of individual parts is given in appendix A. Detailed material information about the composition of the compounds and elements is also provided.

Many of the required accelerator parts were defined readily in the Geant4 example ML2. These were the primary collimator, exit window, ionization chamber, mirror and jaw collimators. They were included to this simulation model as such.

The model of 20 MeV electron beam operational mode required the 6 MeV photon flattening filter to be replaced by a 20 MeV dual scattering foil. The design process of the foil is reported in detail in the next section. Also the target for converting

an incident electron beam to a photon beam was removed along with the multi-leaf collimator of the photon mode. New parts added to the simulation were a mylar film reticle through which the outgoing beam exits the accelerator head structure and 2 different external electron applicators for the production of square beams of 10 cm by 10 cm and 20 cm by 20 cm. Only the 10 cm by 10 cm applicator was used in this study.

While the dimensions of the electron applicators were actually measured in detail, the model of the mylar reticle was based on general knowledge about similar parts. The source to surface distance (SSD) was set at 1.0 m and respectively the isocenter of the accelerator was also set at 1.0 m. In the simulation model the isocenter value defines the track along which the jaw-collimators move.

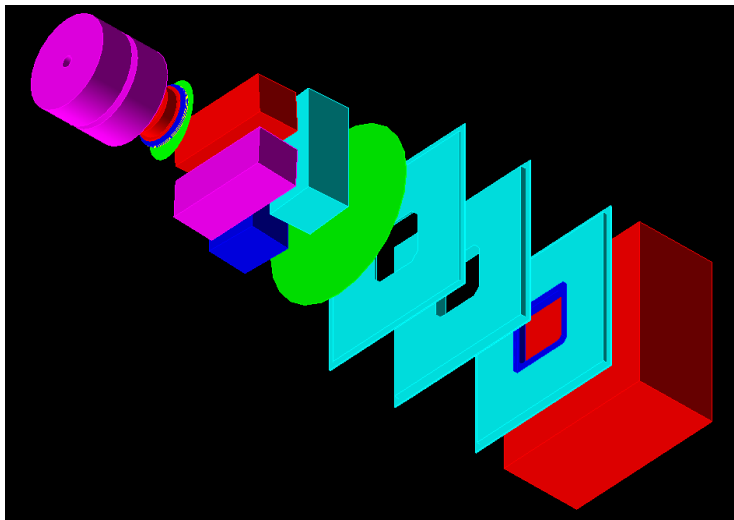


Figure 13. The head geometry of the Varian Clinac 2100 C/D accelerator, external electron applicator plates and water phantom. This image is a snapshot produced with OpenGL runtime visualization of Geant4.

3.1.4 Modeling the 20 MeV dual scattering foil

The most critical individual accelerator part in the simulation model is the scattering foil structure. Its general principle of operation is explained in section 2.5.

The challenge regarding this study was that the detailed information about the scattering foil was not publicly available and the manufacturer was unwilling to provide it. Thus, the model of the 20 MeV dual scattering foil had to be based on reference data found from literature.

On the basis of other similar studies the materials of the primary and secondary scattering foils were chosen to be tantalum and aluminum. The shapes and relative sizes of the foils were based on images of a seminar presentation by Brualla. [86, 87, 82]

Guidelines for determining the detailed values for thickness, side lengths and disc radii were obtained from Dhole et al. [82]. In their paper, they described a design method for an optimized dual scattering foil structures and provided reference values for nominal electron energies 6 MeV, 12 MeV and 18 MeV. Unfortunately no reference values for constructing a dual scattering foil of 20 MeV nominal energy were provided.

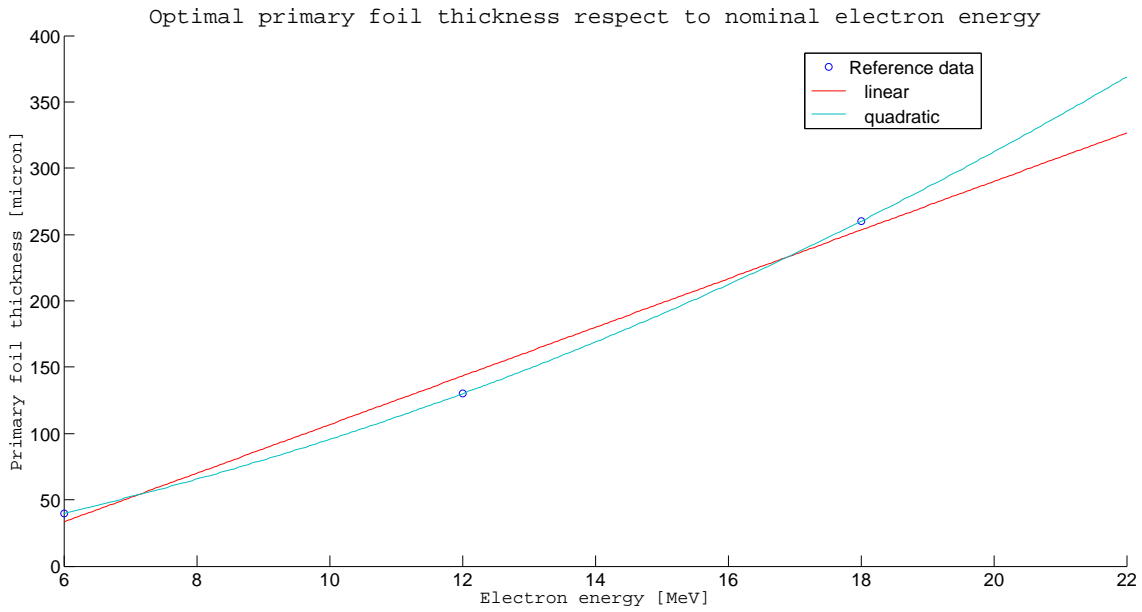
Even though the guidelines found from literature for designing the scattering foil were found very useful, the information gathered this way was too vague for creating an accurately functioning model of the dual scattering foil. Thus, further fine tuning of the model was based on comparing the simulation results of the dose profiles and depth dose curves along with electron energy distributions and photon contamination percentages with the measurement results. In practice this procedure required numerous test simulations, as the energy of the incident beam needed to be re-calibrated for each different foil thickness.

It was tested, that most of the foil dimension values could be based on estimations for required accuracy. The secondary foil width value for a 18 MeV electron beam provided by Dhole et al. was tested to work for a 20 MeV as well. However the thickness values of both foils needed to be based on more accurate reference data since the thickness of the foils is directly proportional to the electron and photon fractions of the beam and hence to the absorbed dose distributions in the phantom.

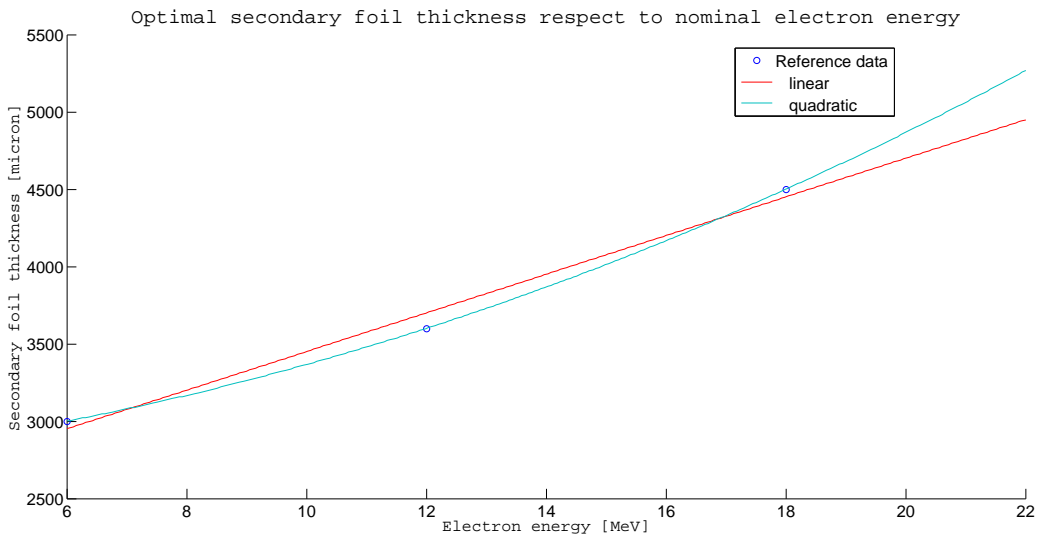
To acquire better reference values for the thickness of the foils, the thickness values of the primary and secondary scattering foils provided by Dhole et al. were plotted against the corresponding nominal energies 6 MeV, 12 MeV and 18 MeV. These plots are presented in figure 14. Evidently, the thickness of the foils grows as a function of energy but the small sampling of 3 data points was not enough to tell exactly how.

A quadratic fit matched the 3 data points very accurately so at first a quadratic function obtained this way was extrapolated to the 20 MeV nominal energy to give a primary foil thickness of and a secondary foil thickness of. However, after the initial beam energy was calibrated so that the outgoing electron energy distribution spiked at 20 MeV, it was found that the bremsstrahlung contamination levels in the dose depth distribution were too high. This indicated, that the chosen foil thickness values were too large.

A linear fit to the energy-thickness-data matched the data points in a satisfactory way. Thickness values obtained from linear extrapolation were 93% and 97% of the primary and secondary foil thickness values obtained with quadratic extrapolation respectively. The accuracy of simulation results was improved for thinner scattering foils but some differences between the simulated and measured results remained. These are discussed further in sections 4 and 5. Two images of the dual scattering foil model used in this study are presented in figure 15.



(a) Primary foil thickness as a function of nominal electron energy.



(b) Secondary foil thickness as a function of nominal electron energy.

Figure 14. Plots of the reference data used to determine the thickness values of the primary and secondary scattering foil models. Both quadratic and linear extrapolations were tested in the simulation and based on the results the linearly extrapolated values were chosen. The reference data was obtained from a study by Dhole et al. [82].

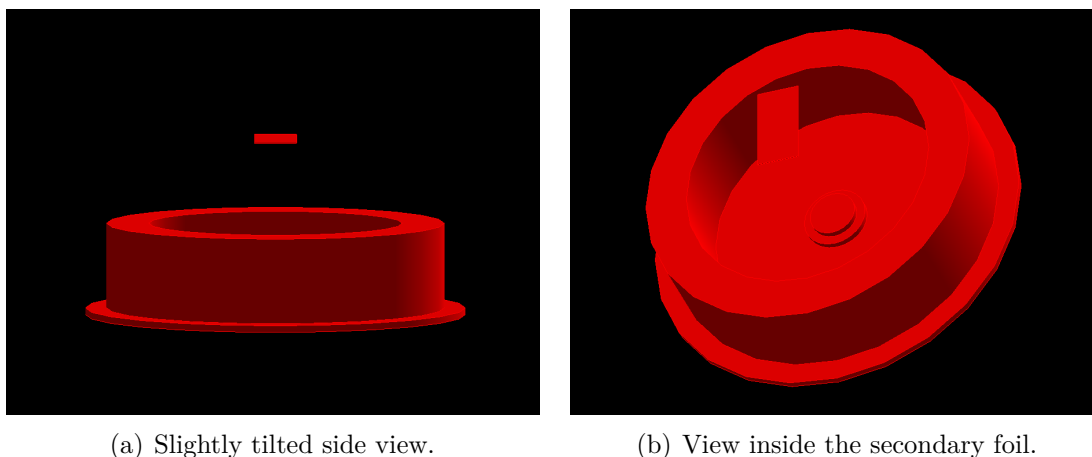


Figure 15. Close-up views of the dual scattering foil model produced with OpenGL runtime visualization of Geant4. The diameter of the widest part of the structure is 9.0 cm.

3.1.5 Optimizing simulation time and accuracy

Modeling a complex physical process with a computer simulation is always about balancing between accuracy and simulation time. Increased accuracy requires more time. The calculations of this study were done with a Dell Latitude E7440 laptop computer, with a Intel Core i7-4600 CPU 2.10 GHz x 4p processor. With this hardware, results of satisfactory accuracy required a minimum simulation time of 2 days depending on the modeled setup.

The simulation time is proportional to the number of interaction events collected in the phantom, which is set sensitive. This number grows with phantom size, cross-sectional beam area and beam energy. This was one of the reasons why only 10 cm by 10 cm beams were studied. The beam energy was fixed to the calibrated value and could not be changed within the simulated set up, but reducing the phantom size was a feasible option. Originally the phantom was a cube with a side length of 30 cm. Reducing the side length to 15 cm in Z-direction, was justified as the area of interest in the dose depth curve was known to be less than 15 cm in depth. This reduced the simulation time by 49%.

The dose on the phantom surface and the shape of the depth dose curve were in the focus of this study. Getting realistic results about them required the invoking of a low-energy physics list for increased accuracy below relativistic energies. Without invoking these models, the surface dose values were consistently too high, making any conclusions about them unreliable. A downside to this was that invoking the low-energy physics list caused a 26% growth in the simulation time.

In Geant4 all particles are tracked up to zero energy by default. However, production cuts may be set by the user to control the optimize the accuracy and simulation

time. A production cut is a limit in energy below which a particle will not produce secondary particles. Each particle type has a production cut value defined as a length. This length is converted to energy in a given material. For optimized performance, each physical entity was defined as its own region to which a specific production cut was given. In the phantom this cut value was 10 μm which converted to 14.09 keV for electrons and to 990 eV for photons (which is the lower limit of a cut value in Geant4).

In the application also the surroundings of the accelerator were modeled for possible radiation safety simulations. However, the radiation effects in the surroundings of the accelerator were not in the focal point of this study. To minimize unnecessary tracking of errant particles, the accelerator head and the phantom were surrounded with particle killing planes that stop and terminate all particles hitting it.

3.2 Computational methods and calculations

3.2.1 Monte Carlo methods

Simulation methods that are based on using random numbers to repeatedly sample a known probability distribution are known as Monte Carlo methods [88]. In case of Geant4 and other similar simulation programs the Monte Carlo methods are used to model the interactions a particle goes through. This modeling is based on an idea, that the cross-section of a particle can be presented as a combination of two probability distributions. First for the distance traveled by the particle between interactions and second for the probability to produce a secondary particle corresponding to the energy and cross-section of the primary particle. [20]

In sampling Geant4 utilizes a combination of composition and rejection methods proven to be efficient [19]. Here these methods are outlined very briefly.

We wish to take a sample $x \in [x_1, x_2]$ from the distribution $f(x)$ and the normalized probability density function can be written in the form

$$f(x) = \sum_{i=1}^n N_i f_i(x) g_i(x), \quad (63)$$

where $N_i > 0$, $f_i(x)$ are the normalized density functions on the interval $[x_1, x_2]$ and $0 \leq g_i(x) \leq 1$. Then according to the method the sample x is chosen by the following steps.

1. A random integer $i \in \{1, 2, \dots, n\}$ is chosen with a probability proportional to N_i .
2. A value x_0 is chosen from the sub distribution $f_i(x)$

3. The rejection function $g_i(x_0)$ is calculated and $x = x_0$ is accepted with a probability of $g_i(x_0)$.
4. If x_0 is rejected, then the procedure restarts from step 1.

This sequence has been proven to work and it can be shown that the average number of attempts required is

$$\sum_{i=1}^n N_i.$$

[20] [88] [19]

In practice a good performance of this method requires the subdistributions $f_i(x)$ to be easily sampled, the rejection functions $g_i(x)$ to be easily evaluated and the mean number of tries to be sufficiently small.

3.2.2 Computation of interactions

Generally the computations related to any interaction include the following three parts:

- calculation of the total cross-section for the interaction
- calculation of the mean free path
- sampling of the final state.

Because Geant4 has multiple computational models for a single interaction depending on what physics lists are invoked, the number of interactions is large and there are several computations per interactions to discuss, the computational models are not discussed individually here. A comprehensive documentation of the physics of Geant4 is found in the Geant4 Physics Reference Manual [19].

Generally the cross-sections and mean free path are calculated according to the cross-section data set associated with the physics process invoked to model a given interaction. For charged particles and neutrons also the computation of energy loss (continuous and discrete) is done.

The calculations involved in the final state sampling vary with each interaction. E.g. for scattering processes the scattering angles are computed according to the associated differential cross-section formula. For pair production and annihilation the energies and momentums of the produced particles are computed. Respectively all recoil momentums and secondary particle energies are computed for each process.

The complexity of each calculation depends on the interaction and the type of computational model invoked.

3.2.3 Energy loss and dose calculation

As described in section 2.3, a charged particle propagating through matter loses its energy both continuously and discretely. Unlike charged particles which experience the Coulomb forces of all atomic electrons and nuclei in the matter, photons lose energy only through discrete processes.

In Geant4 the production threshold energy determines how the energy loss of a charged particle is treated. Above the threshold, the energy loss is simulated by the explicit production of secondary particles. Below the threshold the energy loss is continuous. This means that below the threshold the energy lost in interactions is simulated as continuous and the ejected secondary particles are considered “soft” and never actually generated.

The calculation of the particle’s energy loss and the respectively deposited energy is divided in two. First the mean energy loss and energy deposition are calculated. Then the exact values are calculated by applying different types of energy loss fluctuation models for different types of absorbers.

The mean energy loss of a particle in one step of the simulation is calculated as follows. Let $D(Z, E, T)$ be the differential cross-section per atom for the ejection of a secondary particle with kinetic energy T . E is the total energy of the incident particle and Z is the atomic number of the material. By denoting the production threshold as T_{cut} the mean rate of energy loss of a particle with energy $T < T_{\text{cut}}$ can be written as

$$\frac{dE_{\text{soft}}(E, T_{\text{cut}})}{dx} = n_{\text{at}} \cdot \int_0^{T_{\text{cut}}} D(Z, E, T) T dT \quad (64)$$

in which n_{at} is the number of atoms per unit volume in the material. For more than one process contributing to the energy loss of a a particle, the total continuous part of the energy loss is the sum of equation 64 over these processes

$$\frac{dE_{\text{soft}}^{\text{tot}}(E, T_{\text{cut}})}{dx} = \sum_i \frac{dE_{\text{soft},i}(E, T_{\text{cut}})}{dx}. \quad (65)$$

The discrete part of the energy loss is determined by the total cross-section for the ejection of a secondary particle of energy $T \geq T_{\text{cut}}$, which is

$$\sigma(Z, E, T_{\text{cut}}) = \int_{T_{\text{cut}}}^{T_{\text{max}}} D(Z, E, T) dT \quad (66)$$

where T_{max} is the maximum energy that can be transferred to the secondary particle. Based on this, the mean energy loss is calculated according to the computational model of each process.

These values are pre-calculated and tabulated during the initialization phase of Geant4. Based on the dE/dx table values, a range table is created in a manner

similar to equations. These range values are further converted to an inverse range table. These values are used to compute the particle's continuous energy loss during run time.

If the mean energy loss $\langle\Delta T\rangle$ is less than an allowed limit ξT_0 , where ξ is the linear loss limit parameter with default value $\xi = 0.01$ and T_0 is the kinetic energy of the particle, then the tabulated dE/dx values are used to calculate the mean energy deposition according to

$$\langle\Delta T\rangle = \frac{dE}{dx} \Delta s \quad (67)$$

where Δs is the true step length. For larger fractions of energy lost, the mean loss is computed as

$$\langle\Delta T\rangle = T_0 - f_T(r_0 - \Delta s) \quad (68)$$

where r_0 is the range in the beginning of the step, $f_T(r)$ is the associated inverse range table value which gives the kinetic energy of the particle for a given range value r .

The fluctuations in the energy loss are computed in one of the following ways depending on the absorber thickness and thus, the step length.

1. If the mean energy loss and step length are in the range of validity of a Gaussian approximation of the fluctuation, a Gaussian sampling is used to compute the actual energy loss.
2. For smaller steps the energy loss is computed in the model under the assumption that the step length and the relative energy loss are small so that it is justified to assume that the cross-section can be considered constant along the step.

In the former case the energy loss function approaches the Gaussian distribution with Bohr's variance:

$$\Omega^2 = 2\pi r_e^2 m_e c^2 N_{\text{el}} \frac{Z_h^2}{\beta^2} T_c s \left(1 - \frac{\beta^2}{2}\right), \quad (69)$$

where N_{el} is the electron density of the medium, Z_h is the charge of the incident particle in units of positron charge and T_c is the cut kinetic energy of δ -electrons, and s is the step length.

In the latter case it is assumed that an atom has only 2 energy states E_1 and E_2 . Then, a particle-atom interaction can result in an energy loss of E_1 or E_2 due to atomic excitation. Ionization energy loss is distributed along a function

$$g(E) = \frac{E_0 T_{\text{up}}}{(T_{\text{up}} - E_0) E^2}, \quad (70)$$

where E_0 is the ionization energy of the atom and T_{up} is the production threshold for delta ray production. The numbers of different level excitations n_1 and n_2 as well as the number of ionizations n_3 follow the Poisson distribution and are sampled from it.

The choice of parameter values for determining the excitation and ionization cross-sections in this model is somewhat arbitrary, but they have been chosen to satisfy several conditions from theoretical knowledge and experimental data.

With this method good values for most probable energy loss in thin layers is obtained, but in most cases the width of the energy loss distribution becomes too small. This is why a width correction algorithm is used to rescale E_1 , E_2 , n_1 , and n_2 so that mean energy loss remains the same, but also the FWHM value of the distribution becomes realistic. With the width-corrected values the energy loss from atomic excitations ΔE_{exc} is

$$\Delta E_{\text{exc}} = n_1 E_1 + n_2 E_2. \quad (71)$$

The ionization energy loss is obtained from the distribution $g(E)$ with the inverse transformation method the following way:

$$u = F(E) = \int_{E_0}^E g(x) dx \quad (72)$$

$$\Leftrightarrow E = F^{-1}(u) = \frac{E_0}{1 - u \frac{T_{\text{up}} - E_0}{T_{\text{up}}}}, \quad (73)$$

in which u is a uniformly distributed random number $\in [0, 1]$. The energy loss due to ionization ΔE_{ion} then becomes

$$\Delta E_{\text{ion}} = \sum_{j=1}^{n_3} \frac{E_0}{1 - u_j \frac{T_{\text{up}} - E_0}{T_{\text{up}}}}. \quad (74)$$

Finally, for small steps the total energy loss in one step is

$$\Delta E = \Delta E_{\text{exc}} + \Delta E_{\text{ion}}, \quad (75)$$

and the fluctuations in the energy loss come from the fluctuations in the number of collisions n_i and from the sampling of the ionization loss.

The energy deposited to a an arbitrary volume dV is equal to the total energy loss occurring in that volume. The absorbed dose D , measured in units of $1 \text{ Gy} = 1 \text{ J/kg}$, is equal to the energy deposited to a volume divided by the mass in that volume. In the application Varian, the energy deposition values calculated by Geant4 are invoked for the dose calculation which uses information about the phantom material and voxel division determined by the user. This way the absorbed dose in different parts of the phantom is calculated with a desired density.

Majority of the information in this chapter is taken from the Physics Reference Manual of Geant4 [19]. The reader should see it for greater details about this and other related methods.

3.2.4 Simulation output

For this study, the Varian application was set to produce 2 output files. One for the dose calculations in the selected phantom and one for information about the particles hitting the phantom surface in the central area of the beam.

The output file for dose calculations contains the data about the voxel positioning and sizing as well as the absorbed dose values and square dose values for each voxel. Also the number of events per voxel is provided.

The second output file is generated with the use of the phase space plane that was set to have an area of 2.4 cm by 2.4 cm. The plane was placed in the middle of the phantom surface, perpendicular to the beam direction. The output file contains the data about the particles' positions, momentums, and particle type. Also the type and number of the primary particle that generated the particle in question are provided.

3.2.5 Data analysis

For data analysis a comprehensive Matlab script was written. Important information, such as dose profiles in the phantom along different dimensions and particle energy distributions were extracted. This section is a brief compilation of the methods used to calculate the main results of this study using the data of the simulation output files.

Three different plots of the surface dose of the phantom were created. Cross-sectional scatter plots in x - and y -directions were created by plotting the absorbed dose values for the voxels on the phantom surface with central y - and x - coordinate values respectively. Also a 3D color map of the whole surface distribution was created to visualize the symmetry and uniformity of the dose distribution throughout the phantom surface.

The dose distribution in the phantom was also visualized along the z -axis to create a depth profile of the absorbed dose along the center of the x - y -plane.

The dose values in the output file are the accumulated over the events that take place in each voxel during the simulation (in this context an event refers to any interaction that results in an energy deposition in the phantom). The uncertainty related to each dose value can be deduced the following way.

First the mean dose per event in a voxel is defined as

$$\bar{d} = \sum_{i=1}^N \frac{d_i}{N}, \quad (76)$$

where d_i is the dose deposition related to event number i and N is the total number of events in a voxel.

The sample variance σ^2 which is an estimate of the true variance of individual dose depositions over an infinite number of events is computed as

$$\sigma^2 = \sum_{i=1}^N \frac{(d_i - \bar{d}_i)^2}{N} \quad (77)$$

$$= \frac{1}{N} \sum_{i=1}^N (d_i^2 - 2d_i\bar{d}_i + \bar{d}_i^2) \quad (78)$$

$$= \frac{1}{N} \sum_{i=1}^N (d_i^2) - 2\bar{d}_i \left(\frac{1}{N} \sum_{i=1}^N (d_i) \right) + \bar{d}_i^2 \quad (79)$$

$$= \frac{1}{N} \sum_{i=1}^N (d_i^2) - \bar{d}_i^2 \quad (80)$$

$$= \frac{1}{N} \sum_{i=1}^N (d_i^2) - \left(\frac{1}{N} \sum_{i=1}^N d_i \right)^2 \quad (81)$$

$$= \frac{1}{N} \left[\sum_{i=1}^N (d_i^2) - \frac{1}{N} \left(\sum_{i=1}^N d_i \right)^2 \right]. \quad (82)$$

The expected value of a sample variance defined this way is biased with a factor $(N-1)/N$. Applying Bessel's correction yields the unbiased sample variance s^2

$$s^2 = \frac{N}{N-1} \sigma^2 \quad (83)$$

$$= \frac{1}{N-1} \left[\sum_{i=1}^N (d_i^2) - \frac{1}{N} \left(\sum_{i=1}^N d_i \right)^2 \right] \quad (84)$$

The associated standard deviation is the value interval in which the dose deposition of the next event will belong to with a probability of 68%. The standard deviation s is

$$s = \sqrt{s^2} \quad (85)$$

$$= \sqrt{\frac{1}{N-1} \left[\sum_{i=1}^N (d_i^2) - \frac{1}{N} \left(\sum_{i=1}^N d_i \right)^2 \right]}. \quad (86)$$

The standard error Δd_i of the mean dose deposition per event then is

$$\Delta d = \frac{s}{\sqrt{N}} \quad (87)$$

$$= \frac{\sqrt{\frac{1}{N-1} \left[\sum_{i=1}^N (d_i^2) - \frac{1}{N} \left(\sum_{i=1}^N d_i \right)^2 \right]}}{\sqrt{N}}, \quad (88)$$

and finally the uncertainty related to the total dose deposition per voxel over N events is computed as the cumulative standard error

$$\Delta D = N \Delta d \quad (89)$$

$$= N \frac{\sqrt{\frac{1}{N-1} \left[\sum_{i=1}^N (d_i^2) - \frac{1}{N} \left(\sum_{i=1}^N d_i \right)^2 \right]}}{\sqrt{N}} \quad (90)$$

$$= \sqrt{\frac{N}{N-1} \left[\sum_{i=1}^N (d_i^2) - \frac{1}{N} \left(\sum_{i=1}^N d_i \right)^2 \right]}. \quad (91)$$

With the cumulative dose values $\sum_{i=1}^N d_i$, cumulative square dose values $\sum_{i=1}^N (d_i^2)$ and number of events per voxel N computed automatically to the dose output file, the error bars to all 2D dose plots were computed according to equation 91.

The output file containing particle data was used to compute the number of particles coming out of the accelerator head with different energies. The spacing in energy was 0.25 MeV. These plots were done for electrons and photons separately.

With the same spacing in energy, the contributions of different energy particles to the total energy of the beam were also plotted for electrons and photons separately.

When computing derivative results based on computation results with inherent uncertainties, the error propagation law was used. The error δq of variable q which is a function of variables x_i with inherent uncertainties δx_i is estimated according to

$$\delta q = \sqrt{\sum_i \left(\frac{dq}{dx_i} \delta x_i \right)^2}. \quad (92)$$

4 Results

4.1 Validation of application Varian

In general the validation of a computational model of any physical phenomenon requires for the computed results to be compared with measurements. For a computational model to be valid, the results it produces must meet the measurement results with a given degree of accuracy. In many cases official standards for validation of computational models exist. They are often used to supervise the reliability of commercial software.

Commercially it is important to set fixed standards a product can be measured against. But more importantly for purposes of research and development, validating a computational model will provide information about the strengths and weaknesses of a computational model defining its range of validity, and the applicability of different algorithms and components. This gives important insight for further development work.

The application of this study was not measured against any existing standards, but thorough comparison of computed and measured results was done to identify the level of accuracy and precision of the produced results and to assess their reliability for future simulations.

All the figures related to the validation of application Varian are presented in appendix B. When comparing the computed results with the measurement in dosimetry, a common approach is to compare relative dose values, so that both the measured and the computed values are normalized to unity. This is because simulating a realistic number of particles on a computer is highly inefficient. The form of a dose profile curve is independent of the number of particles as long as there are enough particles for significant statistics.

4.1.1 Electron and photon energy spectra

In figure 16 the energy spectrum of electrons in the central region of the beam is presented. The number of electrons passing through a 2.4 cm times 2.4 cm plane on the phantom surface was tracked, the electron fluence was calculated in units of 1 cm^{-2} and a normalized plot of the results was created to analyze the electron energy distribution. Backscattered particles were filtered from the data. This data visualization was used to set the energy of the incident beam so that the energy of the outgoing particles matches the nominal operation energy.

The spectrum has an expected shape, with a sharp peak at the nominal energy 20 MeV. However, there are minor anomalies. In energies above 20 MeV the spectrum behaves as expected as the normalized electron fluence quickly decreases to 0% for electron energies above 22 MeV. Below 20 MeV the shape of the spectrum is of the expected kind, but the tail of the 20 MeV peak falls down too gradually. Against expectations, the normalized electron fluence doesn't decrease to zero at any point of the spectrum on the left side of the peak. Another unexpected observation is the increase in fluence for the lowest energy electrons below 1 MeV.

To further estimate the effect of the excessive amount of lower energy electrons on the beam, figure 17 shows the fraction of total kinetic energy delivered by electrons of different energies. The amount of total energy delivered by electrons from 18 MeV to 22 MeV amounts for 54.05%, while electrons below 18 MeV amount for 19.08% of the total energy. While the fluence of lower energy electrons is small, their cumulative effect through out the lower part of the spectrum causes a significant contamination to the beam in this simulation model. The energy spectrum is highly dependent on the scattering foil model. Figure 18 is taken from the work of Dhole et. al [82] and it shows that an optimized model of the dual scattering foil could produce a much smaller fraction of low-energy electrons than seen in figure 16.

Figure 19 shows the energy spectrum of photons in a similar manner than figure 16 for electrons. The spectrum is a continuous curve with a peak around 500 keV which decreases quickly as a function of photon energy.

Figure 20 illustrates that the spectrum of photon contribution to the beam energy is shifted to the low energy photons, but photons of all energies up to the incident beam energy contribute significantly. This continuous spectrum is of the expected shape, but the total amount of photons is higher than expected. The energy delivered by photons to the phantom surface accounts for 26.39% of total energy of the beam, while a fraction less than 20% could be expected. This too is highly dependent on the scattering foil model used.

The remaining 0.48% of the total beam energy is delivered by other particles, mainly positrons.

4.1.2 Surface dose profiles

In figure 21 a 3D color map of the surface dose distribution through out the water phantom surface is presented. This was done to assess the shape and uniformity of the surface dose distribution. As expected, the dose distribution is rather uniform with a geometrical cross-section of 10 cm by 10 cm square.

More detailed view of the side profiles of the surface dose distribution is given in figures 22 and 23 which show surface distribution cross-sectional side profiles in x and y directions respectively. Both profiles have an expected shape with maximum values around the center of the profile and minimum values on near the edges.

Figure 24, is a compilation of dose profile measurements done with Varian Clinac 2100 C/D. The measurement setup was otherwise similar to the simulated setup, except that the measured beam size was 20 cm times 20 cm and the absolute dose was 0.2 Gy while the simulated beam size was 10 cm times 10 cm and the absolute dose was 8.8 μ Gy.

Figures 21, 22 and 23 and the related variables have all been normalized to the mean dose of each profile. Variables that describe the profiles numerically are tabulated and compared in tables 3 and 4. The variable “deviation” is the standard deviation computed from the high plateau of the profile. In both directions the computed overall deviation is satisfactory compared to the measured deviation. However, by comparing figures 22 and 23 with figure 24 it can be seen, that the measured profile curve is smooth and continuous while the computed scatter plots are not. In the computed results, the dose values of neighboring voxels differ in many cases more than the uncertainties of individual dose values.

Characteristically to Monte Carlo simulations, the precision of the results improves with sample size. The deviation of the profile curve was observed to decrease with increasing the number of incident electrons generated. The precision of these results is a compromise between simulation time and accuracy to meet the priorities of this project.

With different computational sequences the maximum individual deviations from the mean also varied. An example of this can be seen by comparing variables D_{\min} and D_{\max} for x - and y -directional profiles. For the chosen sequence, the maximum deviation in the x -direction is almost twice as large than in the y -direction even though the standard deviation is approximately the same for both directions. On the

Table 3. The surface dose profile in x direction

	Computed	Measured	Difference
Deviation	3.64%	1.38%	2.26%
D_{\min}	93.92%	98.63%	4.71%
D_{\max}	112.60%	100.01%	12.59%

Table 4. The surface dose profile in y direction

	Computed	Measured	Difference
Deviation	3.47%	2.29%	1.18%
D_{\min}	93.14%	97.73%	4.59%
D_{\max}	106.66%	100.02%	6.64%

other hand, excluding the few anomalies, the x -directional profile is more consistent than the y -directional profile, with smaller differences in dose between neighboring voxels. Based on the many test simulations performed with different numbers of generated incident electrons, the deviation, the consistency and the symmetry of the profiles can be expected to improve in precision with increasing number of incident electrons.

The statistical accuracy in the measured curve is higher than that of the computed curve mainly because the number of incident particles is several orders of magnitude higher. In addition to this, the data points of the measured curve were gathered from 125 mm^3 cavities of the PTW OCTAVIUS 729 detector, while the volume of the voxels in the computation was only 27 mm^3 . Thus each measured data point was averaged over a 4.63 times larger volume.

4.1.3 Depth dose curve

Figure 25 is the computed percentage depth dose (PDD) curve. It illustrates the dose distribution along increasing depth in the water phantom with $z = 0 \text{ mm}$ at the phantom surface. The data was plotted from the voxels at the center of the x - y -plane. Again, the curve has an expected shape with a few anomalies that correspond to the anomalies in the electron and photon energy spectra in figures 16, 17, 19 and 20.

Figure 26 shows the measured PDD curve in water for a 20 MeV electron beam from Varian Clinac 2100 C/D. The depths of maximum dose and relative doses of 90%, 80%, 50% and 30% are highlighted in the figure. To better understand the computed PDD curve of figure 25, the shape of the measured PDD curve of figure 26, which is the expected result, is first analyzed. For comparison also the measured PDD curves for 12 MeV and 6 MeV electron beams are provided in figures 27 and 28.

In the measured 20 MeV PDD curve the surface dose is 95% of the relative maximum. This is a typical result for a 20 MeV electron beam. The reason the maximum dose deposition occurs a few centimeters below the surface is to a minor degree due to the build-up of knock-on electrons and to a larger degree due to the increasing obliquity of electron tracks. The region of the curve before the maximum dose is known as the build-up region. For lower energy beams such as 6 MeV and 12 MeV the surface

dose is even smaller, only 78% and 89% respectively. Lower energy electrons are more likely to be deflected from their tracks in interactions and thus lower energy beams have a greater build-up effect.

When the high energy electrons of the beam enter the water, the electromagnetic cascade starts and the number of free electrons capable of further ionization starts to increase. The dose deposition at a given depth is proportional to the number of electrons passing through it. The number of free electrons reaches its maximum value at a depth where the incident electrons have freed as many electrons as they can before losing all their kinetic energy. After this depth, the number of free electrons starts to decrease as more and more electrons lose their kinetic energy and the number of electrons that scatter away from the central region of the beam exceeds the number of electrons that scatter into that region.

However the depth of maximum deposited dose is dependent on more than just the number of free electrons. The obliquity of electron tracks increases with depth as the electrons go through more and more scattering events. The larger the x - and y -components of an electron's velocity are, the more energy it will deposit per unit length in depth (z -direction). Due to the increasing obliquity of the electron tracks the electron fluence through a 3 dimensional volume reaches its maximum value at the depth where the number of electrons passing through the volume in any direction is the highest. This is the depth of maximum deposited dose.

After this depth, the ever increasing obliquity of electron tracks results in more and more electrons leaving the beam. As the fraction of dispersed electrons grows with increasing depth, the deposited dose starts to fall.

The depth at which electron fluence through a given volume reaches its maximum value increases with beam energy. Due to this the depth of the maximum dose deposition increases as well, but only to a limit. This increase can be seen by comparing the depths of maximum dose in figures 27 and 28. The higher the electron beam energy is, the longer and flatter the beginning of the depth dose curve becomes as shown in figure 26. This is because high energy electrons penetrate deeper into the water with little deflections in their tracks, depositing a more or less constant amount of energy per unit length in depth.

An effect which shifts the depth of the maximum dose closer to the phantom surface for high energy electron beams, is the photon contamination from the bremsstrahlung forming in the accelerator as well as in the phantom. The higher the electron energy is, the higher its fractional energy loss due to bremsstrahlung is. Also the scattering foil structure used to broaden and flatten the beam in the accelerator has to be thicker for higher energies leading to higher amounts of bremsstrahlung forming in the accelerator head. This is why the depth of maximum dose clearly less for the 20 MeV beam in figure 26 than for the 12 MeV in figure 27.

A large portion of the bremsstrahlung contamination consists of lower energy photons, thus the dose deposition due to photons achieves its maximum value in a

shallower depth than the dose deposition due to electrons. With the depth dose curve due to electrons having a flat shape, the photon contribution shifts the maximum value of the curve closer to the phantom surface.

After the depth of maximum dose deposition in the PDD curve, the deposited dose starts to decrease. This area of the curve is known as the fall-off region. The deposited dose decreases with increasing depth as more and more electrons in the beam lose their energy and stop and the remaining beam energy is dispersed over a wider and wider area. The measurement shows that the 20 MeV electron beam loses 95% of its energy by the depth of 12 cm. By this depth, most electrons in the beam have lost their kinetic energy or have scattered away from the central region of the beam. The rapidness of the dose fall-off increases with decreasing beam energy (in the MeV scale). For a 20 MeV beam the fall-off is much more gradual than for the 12 MeV and 6 MeV beams which lose 95% of their energy by 6.2 cm and 3.0 cm depths respectively. This is because on average a higher energy electron must go under more interactions to lose its energy or to be likely deflected from the beam. In a homogeneous medium, a higher number of interactions requires a longer range.

After the fall-off region the dose deposition per unit length in depth stabilizes to a very slowly decreasing slope that can be considered constant in the range of the phantom. This portion of the PDD curve is called the bremsstrahlung tail, and it is due to the photon contamination of the beam. The height of the bremsstrahlung tail, just like the total portion of photons in the beam, gets larger for higher energy electron beams. For a 20 MeV beam the height of the tail should be just under 5% of the maximum dose, as it is in figure 26. For the 12 MeV beam the relative height is less than half of that for the 20 MeV beam, and for the 6 MeV beam the tail height is less than 1% of the maximum dose.

With a general understanding of the expected PDD curve and knowledge about the energy spectra of the particles in the beam, it is easier to analyze the computed result of figure 25. An evident difference between the computed curve of figure 25 and the measured curve of figure 26 is that the computed surface dose is significantly higher than expected. As mentioned, for a nominal energy as high as 20 MeV, the surface dose is close to the maximum dose deposition, but the measurement shows that there ought to be at least a 5% difference. This result is due to the excessive amount of low-energy electrons and photons produced in the simulation model. The data of figures 16, 17, 19 and 20 revealed, that the energy delivered by low-energy electrons and photons was unexpectedly high. This accounts for the 5% rise in the surface dose.

The expected height of the bremsstrahlung tail was under 5%, but the computed result was as high as 6.81%. The tail height was computed by averaging the dose deposition values from depth 11.4 cm to 15.0 cm. This result first revealed that the photon contamination levels produced by the computational model are too high. This observation was backed up by the photon spectra discussed in section 4.1.1,

and the estimations of the desired photon levels were based on this result.

To assess the shape of the computed PDD curve, the depths of maximum dose and relative doses of 90%, 80%, 50% and 30% for both computed and measured PDD curves were tabulated in table 5. The dose deposition was computed for cubic voxels with a side length of 3 mm, due to which there's an 1.5 mm uncertainty related to each computed depth value.

Instead of a one well-defined maximum, the computed PDD curve fluctuates steadily about the maximum value. This results in 4 local maxima before the fall-off region each with a dose over 99% of the global maximum which is located at 3.45 cm. The maximum occurring on the surface of the phantom is explained by the excess low-energy electrons and photons produced in the simulation. The latter three maxima are less separated from their neighboring data points and may be explained to a certain degree by statistical uncertainty due to sample size, but the anomalies of the electron energy spectrum present themselves in this result as well.

As discussed in section 4.1.1, the peak at 20 MeV in figure 16 rises too gradually from the low-energy side of the spectrum, and there is an excess of electrons all the way from a few MeV up to 18 MeV. The contamination effect of these electrons is significant. Based on how the maximum dose depth shifts with electron energy, there is reason to suspect that these electrons cause the PDD curve to fluctuate about the maximum dose all the way to 3.5 cm depth. Mutually an excess in the number of electrons of unwanted energies means a deficit in the number of electrons of desired energies. With a less distinct peak in the energy spectrum of the electrons, subtle characteristics of the PDD curve such as the well-defined maximum value are suppressed by the effects of the lower energy background radiation.

The relative dose values in the fall-off region show a trend that is analogous with previous observations. The differences between the computed and measured values are of the order of a few millimeters and overall the agreement between computed and measured PDD curves is satisfactory. The minor deviations correspond to the anomalies in the energy spectra of figures 16, 17, 19 and 20. The computed values of R_{90} , R_{80} , R_{50} and R_{30} are all smaller or equal to the measured values, within their uncertainties. Because of the excess in the lower energy electrons and deficit in the ~ 20 MeV electrons, the average range of the electrons becomes shorter.

Table 5. Computed and measured PDD values

	Computed	Measured	Difference
R_{\max}	0.15 cm / 1.05 cm / 1.95 cm / 3.45 cm	1.58 cm	
R_{90}	4.95 cm	5.48 cm	-0.53 cm
R_{80}	6.15 cm	6.52 cm	-0.37 cm
R_{50}	7.95 cm	8.10 cm	-0.15 cm
R_{30}	8.55 cm	8.92 cm	-0.37 cm

4.2 Depth dose analysis in water and silicon phantoms

To gain further understanding about the PDD curves in water and to make predictions about the dose deposition occurring in irradiation experiments of electric circuits, an in-depth analysis of the depth dose distribution was done for water and silicon phantoms. Figures related to this analysis are given in appendix C.

Figure 29 shows the computed PDD curve of figure 25 with approximated fractions of electron-induced and photon-induced dose. The approximation of the dose composition was done by running the simulation with the same computational sequence 2 times. A particle filtering phase space plane was placed on top of the phantom. During the first run, all photons incident on the phantom surface were filtered out of the beam and during the second run all electrons and positrons incident on the phantom surface were filtered out.

The two PDD curves produced this way do not represent the actual electron- and photon-induced fractions of the total dose. The mutual effect of these fractions on the PDD curve could not be included in this approach. Secondly, both beams were separately fired to a phantom in an electronic equilibrium state. This is why both beams deposited an absolute dose significantly higher than the actual electron- and photon-induced fractions of the dose.

For this analysis, the sum of the electron- and photon-induced depth dose was calculated and normalized to unity in the manner of figure 25. In figure 29 the blue scatter plot is the original computed PDD curve. The overlapping cyan scatter plot is the normalized sum curve of the separately generated electron- and photon-induced dose. The figures overlap to a large degree with the most significant yet small differences occurring in the beginning of the fall-off region. This good agreement gives reason to think that even though the absolute doses deposited by the filtered electron and photon beams were too high, the shapes of the curves are similar to their relative fractions in the PDD curve.

In figure 29 the red scatter plot is the approximated electron-induced fraction of the dose generated by normalizing the electron-induced PDD curve to the maximum value of the sum curve. The green scatter plot is the approximated photon-induced fraction of the dose generated in a respective manner. As expected, the slope in the fall-off region is mainly due to the fall in the electron-induced dose, while photon induced dose drops less and leaves a higher bremsstrahlung tail.

The curves for the electron- and photon-induced fractions of dose confirm, that the unexpectedly high surface dose in the PDD curve is due to low-energy electrons and photons. Of these, the electron contamination is more significant.

It is also worth noting, that after the phantom surface the electron-induced dose remains very flat, with no significant maximum at any depth. This backs up the previous conclusion that the lower energy contamination around the 20 MeV peak in the electron energy spectrum of figure 16 causes the expected maximum of the

PDD curve to be covered by the background dose.

The curve for the photon-induced dose is also flat before the fall-off region except for a very temperate maximum at 1.95 cm which seems to contribute to the maximum visible at the same depth in the actual PDD curve. However, the expected depth of the photon-induced maximum is smaller as it should shift the maximum of the total PDD curve towards the phantom surface. The measured maximum of the PDD curve occurred at 1.58 cm. If this computed maximum is not due to statistical fluctuation the result suggests, that the photon energy spectrum should be more heavily shifted to lower energies. However the shape of the photon energy spectrum is dependent on the shape of the electron energy spectrum that has verifiable anomalies. There is reason to think, that improvements in the electron spectra will directly translate to photon spectra as well.

The data of figures 17 and 20 reveals that electrons and positrons deliver 73.61% of the beam energy incident on the phantom surface while photons make up for 26.39%. Despite this, summing over the electron-induced and photon-induced dose data of figure 29 shows that only 62.09% of the dose in depth direction is due to the electrons incident on the phantom surface while photons make up for 37.91%. This difference can only be explained by the dispersion of electrons from the beam center in the phantom. It shows that the effect of the photon contamination in the beam is magnified when the energy is absorbed in matter. This underscores the need to minimize the photon contamination of the beam.

Figure 30 has the same data plotted for a silicon phantom, than figure 29 has for water. The silicon phantom's volume and shape were equal to those of the water phantom.

The shape of the actual computed PDD curve is more of the expected type than the one for water. This is due to several reasons. The penetration ranges of electrons of given energy in silicon are a lot shorter than in water. E.g. in water a 5 cm average penetration range requires electrons to have kinetic energy of 10.98 MeV. In silicon the respective value is 22.69 MeV. This results in fewer unwanted low-energy electrons affecting the shape of the PDD curve. Also the absolute deviation of ranges is reduced resulting in more events per voxel. This causes the statistical accuracy of data points to improve. The shorter ranges are naturally due to higher atomic number and density of silicon.

Also the surface dose is close to expected with a relative value of 92.53%. Phase space data-analysis showed, that the effect of low-energy electrons and photons on the surface dose was reduced due to increased back scattering.

Again a good agreement is found between the actual computed PDD curve, and the normalized sum curve of the separately computed electron-induced and photon-induced dose. Thus the normalized curves of the separately calculated electron-induced and photon-induced doses can be considered as valid approximations of the actual dose composition. The most significant yet small differences between the

curves occurs near the phantom surface.

Both the electron-induced fraction of dose and the actual PDD curve reach their maximum at the depth of 1.05 cm. The measured depth of maximum dose deposition in water was 1.58 cm. As expected, the depth of maximum dose for silicon is less than for water. However, based on the previous observations about the energy distribution and composition of the beam as well as the measured and computed PDD curves in water, there is reason to think that the actual depth of maximum dose in silicon is located a little deeper.

Comparing the measured and computed relative dose depth values in table 5 shows that in water the mean difference in depth values along the curves is (3.6 ± 0.8) mm with the standard error of the mean included. Regarding the difference in range-energy relationship of water and silicon as the ratio $10.98/22.69$, the depth of maximum dose deposit in silicon can be approximated to take place (1.7 ± 0.4) mm deeper. Applying the error propagation law to account for the computed uncertainty of 0.4 mm and the inherent uncertainty of 1.5 mm, the corrected depth of maximum dose deposition becomes (1.2 ± 0.2) cm.

Table 6 presents the computed results for the R_{90} , R_{80} , R_{50} and R_{30} values in silicon along with the values corrected in the way presented above. The corrected values can be considered reliable within the deduced uncertainties.

4.3 The ratio of absorbed dose and incident electrons

To estimate the ratio of the absorbed dose and the number of 20 MeV electrons incident on the phantom surface, the maximum depth dose in each phantom was divided by the number of 18 to 22 MeV electrons incident on an area of 1 cm^2 in the central region of the beam at the phantom surface.

The results were $2.87 \cdot 10^{-10} \text{ Gy cm}^2/\text{electron}$ for water and $2.77 \cdot 10^{-10} \text{ Gy cm}^2/\text{electron}$ for silicon. For instance, this means that the deposition of a 10 Gy maximum dose requires a fluence of $3.48 \cdot 10^{10} \text{ electrons/cm}^2$ in water and $3.61 \cdot 10^{10} \text{ electrons/cm}^2$ in silicon.

A reference value was obtained from the electron stopping power data of National

Table 6. Computed and corrected PDD values in silicon

	Computed	Corrected
R_{\max}	$1.05 \pm 0.15 \text{ cm}$	$1.2 \pm 0.2 \text{ cm}$
R_{90}	$2.55 \pm 0.15 \text{ cm}$	$2.7 \pm 0.2 \text{ cm}$
R_{80}	$2.85 \pm 0.15 \text{ cm}$	$3.0 \pm 0.2 \text{ cm}$
R_{50}	$3.45 \pm 0.15 \text{ cm}$	$3.6 \pm 0.2 \text{ cm}$
R_{30}	$3.75 \pm 0.15 \text{ cm}$	$3.9 \pm 0.2 \text{ cm}$

Institute of Standards and Technology (NIST) [89]. The NIST data value for the collision stopping power of 20 MeV electrons in water was 2.046 MeV cm²/g electron which is equal to $3.278 \cdot 10^{-10}$ Gy cm²/electron. This value can be used to estimate the electron fluence required to deposit a given dose. The estimation is done with the help of the measured PDD curve the following way.

A maximum dose deposition of 10 Gy is to be generated in a water phantom with a 20 MeV electron beam. The required electron fluence is to be estimated. The dose deposition of the electrons changes as a function of electron energy. This is why it is difficult to estimate the electron fluence required to produce a dose of 10 Gy at the depth of maximum dose deposition where the beam energy has reduced. However based on the measured PDD curve of figure 26 it is known, that in water a 20 MeV electron beam deposits 95% of its maximum value to the phantom surface. At the very surface of the phantom the beam energy is approximately equal to the nominal energy of 20 MeV. Thus the stopping power of 20 MeV electrons can be used to calculate the electron fluence required to deposit a surface dose equal to 95% fraction of the desired maximum dose of 10 Gy

$$\frac{0.95 \cdot 10.00 \text{ Gy}}{3.278 \cdot 10^{-10} \text{ Gy cm}^2/\text{electron}} = 2.898 \cdot 10^{10} \text{ electrons/cm}^2.$$

The computed value $3.48 \cdot 10^{10}$ electrons/cm² is in good agreement with the reference value $2.898 \cdot 10^{10}$ electrons/cm². This reference value corresponds to an ideal case of a pure monoenergetic unidirectional 20 MeV electron beam. Thus the expected value of electron fluence to deposit a given dose in practice is higher than the theoretical reference value.

No quantitative error analysis was conducted to refine the computed electron fluence and stopping power values as their order of magnitude can be considered valid under the accuracy of the computations done in this study. Based on analysis of figures 16 and 17 it is known that the fluence of 18 to 22 MeV electrons in the simulation was lower than expected. However the maximum dose value is proportional to this fluence, so the ratio of absorbed dose and high-energy electron fluence is expected to change only a little as the accelerator model is further refined.

The values calculated here can be considered as approximative reference values until further development steps are taken to improve the accuracy of the model used.

5 Conclusions

Regarding the validation of the simulation program created in this study, it can generally be stated that all obtained results were close to expected. Equally importantly, the subtle anomalies found in the results were consistent with each other. This is why there is no reason associate any of them with possible shortcomings in the computational models of Geant4.

Throughout different phases of this study, the performance of Geant4 was evaluated. It was verified that Geant4 has the capability to accurately reproduce and predict measured results of electron and photon interactions with matter at energies of ~ 20 MeV and below. On the contrary it was also verified that despite the optimized performance of Geant4, high precision results require a great deal of computational power. With a processor unit of an average laptop at hand, compromises between simulation time and accuracy were necessary.

All dose deposition profiles were of the expected shape. The surface dose side profiles of figures 21, 22 and 23 indicated that the intensity distribution of the computed beam is uniform, and the precision of these results improved with growing sample size throughout the test calculations done in study. The consistency of the surface dose profiles is a good indicator of the statistical uncertainty related to the sample size of each simulation.

The anomalies in the depth dose profile of figure 25 were the hight of the surface dose, the lack of one well defined maximum value, the small shifting of the curve towards the phantom surface and the height of the bremsstrahlung tail. The first three of these could clearly be attributed to the anomalies in the electron energy spectrum of figure 16 and the fourth to the excess of gamma rays in the beam.

The unexpected 5% rise in the surface dose was due to the excess of low-energy electrons which deposit all their energy in the first 3 mm below the phantom surface. The lack of a well defined maximum was due to the gradual rise of energy in the electron energy spectrum. Due to it there was an excessive amount of electrons of all energies all the way up to 18 MeV. Their presence in the beam caused the area of the maximum dose in the PDD curve to spread out over a longer depth. The expected maximum is so subtle, that also statistical uncertainties became significant in this area of the PDD curve.

Having an excess of photons and low-energy electrons in the beam consequently reduced the fraction of high-energy electrons. This is why the whole computed depth curve was slightly shifted towards the phantom surface. With a higher fraction of

the beam energy attributed to high-energy electrons, the average range of a particle in the beam also increases. The height of the bremsstrahlung tail was verified to be an effect of excess gamma rays by analyzing the data of figures 19 and 20 as well as figure 29.

Many of the conclusions made about the PDD curve in water were also verified by the dose composition analysis of figure 29. Most importantly it was found that the effects of excess low-energy electrons and photons in the beam are amplified in the absorbed dose. The fraction of electron-induced dose in the water phantom was found to be 11.52% less than the electron energy fraction of the beam. The high-energy electrons are more likely to disperse from the beam before depositing their energy into the phantom. This adds to why the right electron energy spectrum and particle composition of the beam are crucial to the depth dose profile.

With the understanding obtained from the validation process, the predicted PDD curve in a silicon phantom was assessed. The curve had the expected shape similar to the PDD curve in water, only compressed in depth due to shorter average particle ranges. The most significant difference was that in silicon the surface dose was not too high. Phase space data analysis showed that this was due to increased back scattering of low energy electrons at the phantom surface. Due to shorter ranges there were more events per voxel, which is why the statistical accuracy of the result was improved. Also the deviation about the nominal electron energy and the effect of low-energy electrons were damped down, resulting in a more consistent PDD curve shape.

The validation process showed that there is reason to suspect that the PDD curve is shifted towards the phantom surface. The expected error was calculated and the results were corrected. This showed, that the developed simulation model allows for the prediction of measurement results with well-defined and justified limits of uncertainty.

Excluding the statistical uncertainty related to chosen sample size, all unexpected features in the dose profile curves can be associated with anomalies in the electron energy spectrum of the beam and the excessive gamma ray yield. As mentioned, the beam composition and energy distribution are largely determined by the dual scattering foil which spreads out and flattens the incident beam which first enters the accelerator head. A major challenge regarding this study was that the data regarding the dual scattering foil was not available. Thus there is reason to suspect that most anomalies in the results are due to lack of accuracy in the dual scattering foil model.

A significant amount of effort was put to adjusting and testing the dual scattering foil model, but no arbitrary changes were made. All measures and material choices were based on reference data found in literature.

Other sources of low-energy electrons and photons are the jaw collimators and the electron applicator. These parts cut off the edges of the beam. Naturally their inner

surfaces are sources to many scattering events which contribute to the amount of low-energy electrons and photons in the beam.

It is also known that the beam area size has an effect on the PDD curve shape. The PDD curve is measured in depth direction at the center of the phantom. Due to scattering, all radiated areas in the phantom contribute cumulatively to the dose in the central region. This is why a larger field size results in amplification of these scattering effects which include a lower relative surface dose (or greater build-up effect) and a greater depth of maximum dose and fall-off region. Of these the first and the last were observed but mainly attributed to the anomalies in the electron energy spectrum.

The effect of beam area size is mostly important for small beam areas it saturates for larger areas. The simulation computed the PDD curve for a 10 cm by 10 cm beam area, while the measured PDD curve was for a 15 cm by 15 cm beam. Even though the difference in area size is notable, in these area sizes these effects become negligible.

Another difference between the computed and measured setup was that in the simulation model, the phantom surface was placed at $SSD = 100$ cm and the PDD curve was measured in a single run. Contrarily in measurements the detector remained at $SSD = 100$ cm while the phantom was moved around it. Due to this the beam got more dispersed in the lower parts of the phantom in the computational setup. More scattering events occurred resulting in relatively higher doses in greater depths. However this effect is very small, and based on the results it does not compensate for the shifting of the beam towards the phantom surface due to low-energy particle contamination.

Having mapped the sources of uncertainties in this study, the next steps in simulation program development and research become clear. Basing the dual scattering foil model on accurate data is crucial to better evaluate the contribution of other sources of uncertainty in the results. To evaluate the effect of the beam area on the PDD curve, similar simulations of different beam area sizes should be conducted. To reduce the statistical uncertainty in the results with a larger sample size, increased computational power also is necessary.

This study was focused around simulation program development work so not as much attention was paid to the methods with which the comparative measurement results had been obtained. This also guides the way for further research. New measurements to create comparable data of different beam areas should be conducted. Also detailed knowledge about detector sensitivity and Geant4 performance could be obtained by creating computational models of the detectors themselves.

While the simulation model may be developed further, the version created in this study is operational and has been tested to work within defined limits of uncertainty.

References

- [1] Lahti V. A simulation model for varian Clinac 2100C/D linear accelerator. Erikoistyö, University of Jyväskylä, Finland, 2016. Unpublished.
- [2] J. Allison et al. Geant4 - a simulation toolkit. *Nuclear Instruments and Methods in Physics Research*, 506:250–303, 2003.
- [3] K. Amako, S. Guatelli, V. Ivanchenko, M. Maire, B. Mascialino, K. Murakami, L. Pandola, S. Parlati, M.G. Pia, M. Piergentili, T. Sasaki, and L. Urban. Geant4 and its validation. *Nuclear physics B*, 150:44–49, 2006.
- [4] K. Amako. Present status of geant4. *Nuclear Instruments and Methods in Physics Research*, 453:455–460, 2000.
- [5] V.N. Ivanchenko. Geant4: Physics potential for instrumentation in space and medicine. *Nuclear Instruments and Methods in Physics Research*, 525:402–405, 2004.
- [6] G. Barca, F. Castrovillari, S. Chauvie, D. Cuce, F. Foppiano, G. Ghiso, S. Guatelli, E. Lamanna, M.C. Lopes, L. Peralta, M.G. Pia, P. Rodrigues, A. Trindade, and M. Veltri. A powerful simulation tool for medical physics applications: Geant4. *Nuclear physics B*, 125:80–84, 2003.
- [7] M.G. Pia. The geant4 toolkit: simulation capabilities and application results. *Nuclear physics B*, 125:60–68, 2003.
- [8] A. Einstein. Ist die trägheit eines körpers von seinem energieinhalt abhängig? [Does the inertia of a body depend upon its energy-content?]. *Annalen der Physik*, 323(113):639–641, March 1905.
- [9] A. Einstein. Zur Elektrodynamik bewegter Körper [On the electrodynamics of moving bodies]. *Annalen der Physik*, 322(10):891–921, 1905.
- [10] D.H. Perkins. *Introduction to High Energy Physics*. Cambridge University Press, 4th edition, 2000. First published by Addison-Wesley Publishing Company Inc. 1972.
- [11] D.J. Griffiths. *Introduction to Quantum Mechanics*. Pearson Prentice Hall, 2nd edition, 2005.
- [12] H. Bethe. Zur theorie des durchgangs schneller korpuskularstrahlen durch materie [Theory of the passage of fast corpuscular rays through matter]. *Annalen der Physik*, 397(3):325–400, 1930.

- [13] K. S. Krane. *Introductory Nuclear Physics*. John Wiley & Sons Inc., 3rd edition, 1988.
- [14] A. Kramida, Yu. Ralchenko, J. Reader, and NIST ASD Team. NIST Atomic Spectra Database (ver. 5.3), [Online]. Available: <http://physics.nist.gov/asd> [2017, January 20]. National Institute of Standards and Technology, Gaithersburg, MD., 2015.
- [15] C. T. Ulrey. An experimental investigation of the energy in the continuous x-ray spectra of certain elements. *Phys. Rev.*, 11:401–410, May 1918.
- [16] H. W. Koch and J. W. Motz. Bremsstrahlung cross-section formulas and related data. *Rev. Mod. Phys.*, 31:920–955, Oct 1959.
- [17] Y. S. Tsai. Pair production and bremsstrahlung of charged leptons. *Rev. Mod. Phys.*, 46:815–851, Oct 1974.
- [18] Y. S. Tsai. Erratum: Pair production and bremsstrahlung of charged leptons. *Rev. Mod. Phys.*, 49:421–423, Apr 1977.
- [19] D.H. Wright et al. *Geant4.10.1 Physics Reference Manual*. Geant4 Collaboration, 2005. Available: Geant4 User Documentation, <http://geant4.cern.ch/support/userdocuments.shtml>.
- [20] H. Messel and D.F. Crawford. *Electron–Photon Shower Distribution Function: Tables for Lead, Copper and Air Absorbers*. Elsevier Science, 2013 (1970).
- [21] W. Heitler. *The quantum theory of radiation*. Clarendon Press Oxford, 3rd ed. edition, 1954.
- [22] C. et al. Patrignani. Review of Particle Physics. *Chin. Phys.*, C40(10):100001, 2016.
- [23] A. Einstein. Concerning an heuristic point of view toward the emission and transformation of light. *Annalen Phys.*, 17:132–148, 1905.
- [24] R. D. Knight. *Physics for scientists and engineers*. Pearson Addison-Wesley, 2nd edition, 2008.
- [25] I. S. Grant and W. R. Phillips. *Electro-magnetism*. John Wiley & Sons, 2nd edition, 1990.
- [26] J. H. Hubbell. Photon cross sections, attenuation coefficients, and energy absorption coefficients from 10 keV to 100 GeV. *NSDRS-NBS*, 29, 1969.
- [27] A. H. Compton. A quantum theory of the scattering of x-rays by light elements. *Phys. Rev.*, 21:483–502, May 1923.
- [28] O. Klein and Y. Nishina. Über die streuung von strahlung durch freie elektro-nen nach der neuen relativistischen quantendynamik von dirac. *Zeitschrift für Physik*, 52(11):853–868, 1929.

- [29] S. Flügge. *Handbuch der Physik*. Number nid. 34 in *Handbuch der Physik*. Springer, 1958.
- [30] J. H. Hubbell, Wm. J. Veigele, E. A. Briggs, R. T. Brown, D. T. Cromer, and R. J. Howerton. Atomic form factors, incoherent scattering functions, and photon scattering cross sections. *Journal of Physical and Chemical Reference Data*, 4(3):471–538, 1975.
- [31] J.H. Hubbell. Electron–positron pair production by photons: A historical overview. *Radiation Physics and Chemistry*, 75(6):614 – 623, 2006. Pair Production.
- [32] P. A. M. Dirac. The quantum theory of the electron. *Proceedings of the Royal Society of London A: Mathematical, Physical and Engineering Sciences*, 117(778):610–624, 1928.
- [33] P. A. M. Dirac. The quantum theory of the electron. part ii. *Proceedings of the Royal Society of London A: Mathematical, Physical and Engineering Sciences*, 118(779):351–361, 1928.
- [34] C. D. Anderson. The positive electron. *Phys. Rev.*, 43:491–494, Mar 1933.
- [35] F. Perrin. Possibilité de maté rialisation par interaction d’un photon et d’un é lectron. *Compt. Rend.*, 197:1100–1102, 1933.
- [36] R. C. Mohanty, E. H. Webb, H. S. Sandhu, and R. R. Roy. Momentum and angular distribution of recoil electrons in triplet production. *Phys. Rev.*, 124:202–205, Oct 1961.
- [37] J. Castor, J. Augerat, A. Devaux, M. Lieutier, L. Avan, and D. Isabelle. Determination de la section efficace de production de triplets dans l’emulsion nucléaire. *Journal de Physique Colloques*, 31(C2):C2–108–C2–109, 1970.
- [38] J. H. Hubbel, H. A. Gimm, and I. Øverbø. Pair, triplet, and total atomic cross sections (and mass attenuation coefficients) for 1 mev –100 gev photons in elements $z = 1–100$. *J. Phys. Chem. Ref. Data*, 9:1023–1147, 1980.
- [39] H. Bethe and W. Heitler. On the stopping of fast particles and on the creation of positive electrons. *Proceedings of the Royal Society of London A: Mathematical, Physical and Engineering Sciences*, 146(856):83–112, 1934.
- [40] L. C. Maximon. Simple analytic expressions for the total born approximation cross section for pair production in a coulomb field. *J. Res. Bur. Stand.*, 72B(1):79, 1968.
- [41] I. Øverbø, K. J. Mork, and H. A. Olsen. Exact calculation of pair production. *Phys. Rev.*, 175:1978–1981, Nov 1968.
- [42] J. H. Hubbell and Øverbø I. Relativistic atomic form factors and photon coherent scattering cross sections. *Journal of Physical and Chemical Reference Data*, 8(1):69–106, 1979.

- [43] H. K. Tseng and R. H. Pratt. Screening effects in pair production near threshold. *Phys. Rev. A*, 21:454–457, Feb 1980.
- [44] I. Øverbø. Screening correction in electron pair production by intermediate and low-energy photons. *Phys. Scripta*, 19:299–306, 1979.
- [45] I. Øverbø. The Coulomb Correction to electron Pair Production by Intermediate-Energy Photons. *Phys. Lett.*, B71:412–414, 1977.
- [46] K. Mork and H. Olsen. Radiative corrections. i. high-energy bremsstrahlung and pair production. *Phys. Rev.*, 140:B1661–B1674, Dec 1965.
- [47] A. Borsellino. Über die materialisierung der γ -strahlen im feld eines elektrons. *Helvetica Physica Acta*, 20:136–138, 1947.
- [48] A. Borsellino. Sulle coppie di elettroni create da raggi γ in presenza di elettroni. *Il Nuovo Cimento (1943-1954)*, 4(3):112–130, 1947.
- [49] A. Ghizzetti. Teoria della produzione di coppie dielettroni. *Rev. Math. y Fisica Teor. (Ser. A)*, 6:37–50, 1947.
- [50] E. Haug. Bremsstrahlung and Pair Production in the Field of Free Electrons. *Z. Naturforsch.*, A30:1099–1113, 1975.
- [51] E. Haug. Simple analytic expressions for the total cross-section for gamma e pair production. *Z. Naturforsch.*, 36A:413–414, 1981.
- [52] E. Haug. On Energy and Angular Distributions of Electrons in Triplet Production. *Zeitschrift Naturforschung Teil A*, 40:1182–1188, December 1985.
- [53] J. A. Wheeler and W. E. Lamb. Influence of atomic electrons on radiation and pair production. *Phys. Rev.*, 55:858–862, May 1939.
- [54] K. J. Mork. Pair production by photons on electrons. *Phys. Rev.*, 160:1065–1071, Aug 1967.
- [55] J.W. Rayleigh. *On the Light from the Sky, Its Polarization and Colour*. 1871.
- [56] J. W. Strutt. *On the Scattering of Light by small Particles*, volume 1 of *Cambridge Library Collection - Mathematics*. Cambridge University Press, 1899.
- [57] J. W. Strutt. *On the Electromagnetic Theory of Light*, volume 1 of *Cambridge Library Collection - Mathematics*, page 518–536. Cambridge University Press, 1899.
- [58] J. W. Strutt. *On the Transmission of Light through an Atmosphere containing Small Particles in Suspension, and on the Origin of the Blue of the Sky*, volume 4 of *Cambridge Library Collection - Mathematics*, page 397–405. Cambridge University Press, 1903.

- [59] W. Bambynek, B. Crasemann, R. W. Fink, H. U. Freund, H. Mark, C. D. Swift, R. E. Price, and P. V. Rao. X-ray fluorescence yields, auger, and coster-kronig transition probabilities. *Rev. Mod. Phys.*, 44:716–813, Oct 1972.
- [60] R. W. Fink, R. C. Jopson, H. Mark, and C. D. Swift. Atomic fluorescence yields. *Rev. Mod. Phys.*, 38:513–540, Jul 1966.
- [61] M. O. Krause. Atomic radiative and radiationless yields for k and l shells. *Journal of Physical and Chemical Reference Data*, 8(2):307–327, 1979.
- [62] L. Meitner. Über die entstehung der β -strahl-spektren radioaktiver substanzen. *Zeitschrift für Physik*, 9(1):131–144, 1922.
- [63] D. Coster and R. De L. Kronig. New type of auger effect and its influence on the x-ray spectrum. *Physica*, 2(1):13 – 24, 1935.
- [64] B. Richard, B. Firestone, and Virginia S. S. *Table of Isotopes*. John Wiley & Sons, Inc., 8th edition, 1996.
- [65] K. A. Snover. Giant nuclear resonances. 2014.
- [66] J. C. Liu, K. R. Kase, X. S. Mao, W. R. Nelson, J. H. Kleck, and S. Johnson. Photoneutrons from varian clinac accelerators and their transmissions in materials. *SLAC-PUB-7404*, 2006.
- [67] A. Ma, J. Awotwi-Pratt, A. Alghamdi, A. Alfuraih, and N. M. Spyrou. Monte carlo study of photoneutron production in the varian clinac 2100c linac. *Journal of Radioanalytical and Nuclear Chemistry*, 276(1):119–123, 2008.
- [68] M.T.B. Toossi, M. Behmadi, M. Ghorbani, and H. Gholamhosseinian. A monte carlo study on electron and neutron contamination caused by the presence of hip prosthesis in photon mode of a 15 mv siemens primus linac. *Journal of Applied Clinical Medical Physics*, 14:52–67, 2013.
- [69] N. A. Burgov, G. V. Danilyan, Dolbilkin. B. S., L. E. Lazareva, and F. A. Nikolaev. Cross section for gamma-ray absorption by carbon in the giant resonance region. *JETP*, 148, 1964.
- [70] B. S. Dolbilkin, V. A. Zapevalov, V. I. Korin, L. E. Lazareva, and Nikolaev. F. A. *PICNS*, 64, 1964.
- [71] B. S. Dolbilkin, V. A. Zapevalov, V. I. Korin, L. E. Lazareva, and F. A. Nikolaev. *Izv. Akad. Nauk fiz.*
- [72] S. C. Fultz, R. L. Bramblett, J. T. Caldwell, and R. R. Harvey. Photoneutron cross sections for natural cu, cu⁶³, and cu⁶⁵. *Phys. Rev.*, 133:B1149–B1154, Mar 1964.
- [73] B. L. Berman, J. T. Caldwell, R. R. Harvey, M. A. Kelly, R. L. Bramblett, and S. C. Fultz. Photoneutron cross sections for zr⁹⁰, zr⁹¹, zr⁹², zr⁹⁴, and y⁸⁹. *Phys. Rev.*, 162:1098–1111, Oct 1967.

- [74] R. L. Bramblett, J. T. Caldwell, B. L. Berman, R. R. Harvey, and S. C. Fultz. Photoneutron cross sections of pr^{141} and i^{127} from threshold to 33 mev. *Phys. Rev.*, 148:1198–1205, Aug 1966.
- [75] E. Ambler, E. G. Fuller, and H. Marshak. Direct observation of the optical anisotropy of the holmium nucleus. *Phys. Rev.*, 138:B117–B126, Apr 1965.
- [76] R. L. Bramblett, J. T. Caldwell, G. F. Auchampaugh, and S. C. Fultz. Photoneutron cross sections of ta^{181} and ho^{165} . *Phys. Rev.*, 129:2723–2729, Mar 1963.
- [77] R. R. Harvey, J. T. Caldwell, R. L. Bramblett, and S. C. Fultz. Photoneutron Cross Sections of Pb-206, Pb-207, Pb-208, and Bi-209. *Phys. Rev.*, 136:B126–B131, 1964.
- [78] C. D. Bowman, G. F. Auchampaugh, and S. C. Fultz. Photodisintegration of u^{235} . *Phys. Rev.*, 133:B676–B683, Feb 1964.
- [79] J.H. Hubbell. Photon mass attenuation and energy-absorption coefficients. *The International Journal of Applied Radiation and Isotopes*, 33(11):1269 – 1290, 1982.
- [80] A. McNair. Icru report 33 - radiation quantities and units pub: International commission on radiation units and measurements, washington d.c. usa issued 15 april 1980, pp.25. *Journal of Labelled Compounds and Radiopharmaceuticals*, 18(9), 1980.
- [81] J. H. Hubbell, National Institute of Standards, and Technology (U.S.). *An examination and assessment of available incoherent scattering S-Matrix theory, also compton profile information, and their impact on photon attenuation coefficient compilations [microform] / J.H. Hubbell*. U.S. Dept. of Commerce, Technology Administration, National Institute of Standards and Technology Gaithersburg, MD (100 Bureau Drive, Gaithersburg 20899-8463), 1999.
- [82] S. T. Chavan, R. Krishnan, S. N. Pethe, V. N. Bhoraskar, S. D. Dhole, and B. J. Patil. Optimization of Dual Scattering Foil for 6 to 20 MeV Electron Beam Radiotherapy. *Conf. Proc.*, C110328:2157–2159, 2011.
- [83] M. Vesternholm and J. Kyppö. *Java-ohjelmointi*. Talentum Media, 8th edition, 2010.
- [84] A.P. Black. Object-oriented programming: Some history, and challenges for the next fifty years. *Information and Computation*, 231:3–20, 2013.
- [85] A. Snyder. The essence of objects: Common concepts and terminology. Technical report, Hewlett Packard Software and Systems Laboratory, 1991.
- [86] J. V. Turian, B. D. Smith, D. A. Bernard, K. L. Griem, and J. C. Chu. Monte carlo calculations of output factors for clinically shaped electron fields. *Journal of Applied Clinical Medical Physics*, 5(2):42–63, 2004.

- [87] L. Brualla, F. Salvat, E. Franchisseur, S. García-Pareja, and A. Lallena. Advanced variance reduction techniques applied to monte carlo simulation of linacs. Seminar Presentation, 2008.
- [88] W. R. Nelson, H. Hiriyama, and D.W.O. Rogers. The egs4 code system, slac-report 265. Technical report, Stanford Linear Accelerator Centre, 1985.
- [89] ESTAR stopping-power and range tables for electrons, NIST. http://physics.nist.gov/cgi-bin/Star/e_table.pl.

A Tabulated data of the materials and structure of the simulation model

Table 7. The structure of the simulated accelerator model

Part	Position vector	Rotation
UpperCollimator	$\begin{bmatrix} 0.0 & 0.0 & -1.0 \end{bmatrix}$	$\begin{bmatrix} 0 \end{bmatrix}$
CylMinusCone	$\begin{bmatrix} 0.0 & 0.0 & 6.2 \end{bmatrix}$	$\begin{bmatrix} 180.0 & 0.0 & 0.0 \end{bmatrix}$
BeWTubePV	$\begin{bmatrix} 0.0 & 0.0 & 10.0 \end{bmatrix}$	$\begin{bmatrix} 0 \end{bmatrix}$
SF20MEVPlate1	$\begin{bmatrix} 0.0 & 0.0 & 11.0 \end{bmatrix}$	$\begin{bmatrix} 0 \end{bmatrix}$
SF20MEVTube	$\begin{bmatrix} 0.0 & 0.0 & 14.0 \end{bmatrix}$	$\begin{bmatrix} 0 \end{bmatrix}$
SF20MEVBrassUpper	$\begin{bmatrix} 0.0 & 0.0 & 14.77 \end{bmatrix}$	$\begin{bmatrix} 0 \end{bmatrix}$
SF20MEVBrassLower	$\begin{bmatrix} 0.0 & 0.0 & 14.92 \end{bmatrix}$	$\begin{bmatrix} 0 \end{bmatrix}$
SF20MEVPlate2	$\begin{bmatrix} 0.0 & 0.0 & 15.08 \end{bmatrix}$	$\begin{bmatrix} 0 \end{bmatrix}$
ionisationChamberTubeW1PV	$\begin{bmatrix} 0.0 & 0.0 & 15.7 \end{bmatrix}$	$\begin{bmatrix} 0 \end{bmatrix}$
ionisationChamberTubeP1PV	$\begin{bmatrix} 0.0 & 0.0 & 15.8 \end{bmatrix}$	$\begin{bmatrix} 0 \end{bmatrix}$
ionisationChamberTubeW2PV	$\begin{bmatrix} 0.0 & 0.0 & 15.9 \end{bmatrix}$	$\begin{bmatrix} 0 \end{bmatrix}$
ionisationChamberTubeP2PV	$\begin{bmatrix} 0.0 & 0.0 & 16.0 \end{bmatrix}$	$\begin{bmatrix} 0 \end{bmatrix}$
ionisationChamberTubeW3PV	$\begin{bmatrix} 0.0 & 0.0 & 16.1 \end{bmatrix}$	$\begin{bmatrix} 0 \end{bmatrix}$
ionisationChamberTubeP3PV	$\begin{bmatrix} 0.0 & 0.0 & 16.2 \end{bmatrix}$	$\begin{bmatrix} 0 \end{bmatrix}$
MirrorTubePV	$\begin{bmatrix} 0.0 & 0.0 & 17.5 \end{bmatrix}$	$\begin{bmatrix} 0.0 & 12.0 & 0.0 \end{bmatrix}$
Jaws1XPV	User defined	User defined
Jaws2XPV	User defined	User defined
Jaws1YPV	User defined	User defined
Jaws2YPV	User defined	User defined
mylarReticule	$\begin{bmatrix} 0.0 & 0.0 & 52.0 \end{bmatrix}$	$\begin{bmatrix} 0 \end{bmatrix}$
cm10x10applicatorUpper	$\begin{bmatrix} 0.0 & 0.0 & 64.1 \end{bmatrix}$	$\begin{bmatrix} 0 \end{bmatrix}$
cm10x10applicatorMiddle	$\begin{bmatrix} 0.0 & 0.0 & 77.55 \end{bmatrix}$	$\begin{bmatrix} 0 \end{bmatrix}$
cm10x10applicatorLower	$\begin{bmatrix} 0.0 & 0.0 & 94.2 \end{bmatrix}$	$\begin{bmatrix} 0 \end{bmatrix}$

Table 8. Simulated accelerator parts

Cylinders

Part	Material	Inner radius (cm)	Outer radius (cm)	Height (cm)
UpperCollimator	W	1.0	8.0	3.0
CylMinusCone	W	1.77 - 0.5	8.0	3.1
BeWTube	Be	0.0	3.6	0.02
3 X ionisationChamberTubeW	KAPTON	0.0	5.8	0.04064
3 X ionisationChamberTubeP	KAPTON	0.0	5.8	0.02540
MirrorTubePV	MYLAR	0.0	6.3	0.05
mylarReticule	MYLAR	0.0	15.0	0.04
SF20MEVTube	Al	3.0	4.0	2.0
SF20MEVPlate2	Al	0.0	4.5	0.156
SF20MEVBrassLower	Al	0.0	0.75	0.156
SF20MEVBrassUpper	Al	0.0	0.55	0.156

Boxes

Part	Material	Length (cm)	Width (cm)	Height (cm)
SF20MEVPlate1	Ta	1.0	2.0	0.0290
Jaws1XPV	steel1	9.0	18.6	7.8
Jaws2XPV	steel1	9.0	18.6	7.8
Jaws1YPV	steel1	18.6	7.0	7.8
Jaws2YPV	steel1	18.6	7.0	7.8
cm10x10applicatorUpper	steel1	28.0	28.0	0.6
cm10x10upperOuterPlate	steel1	30.0	30.0	0.2
cm10x10applicatorMiddle	steel1	28.0	28.0	2.1
cm10x10middleOuterPlate	steel1	30.0	30.0	0.2
cm10x10applicatorLower	steel1	28.0	28.0	1.4
cm10x10lowerOuterPlate	steel1	30.0	30.0	0.2

Extruded octagon apertures

Name	Long side length (cm)	Short side length (cm)	Height (cm)	Extrusion ratio
cm10x10upperAperture	6.96	1.83	0.602	99.0/95.5
cm10x10middleAperture	7.35	1.56	2.102	98.4/95.7
cm10x10lowerAperture	10.18	0.99	0.602	94.5/93.8
cm10x10insertBlockAperture	7.98	1.00	1.402	94.5/93.8

Table 9. Materials present in the simulation

Category	Material	Name	Density (g/cm ³)	Mass fractions of elements	
G4Material	Iron	Fe	7.874	Fe (100.00%)	
	Copper	Cu	8.960	Cu (100.00%)	
	Beryllium	Be	1.848	Be (100.00%)	
	Tungsten	W	19.3	W (100.00%)	
	Kapton	material	1.420	C (69.11%) H (2.64%) N (7.33%) O (20.92%)	
	Mylar	MYLAR	1.400	C (62.50%) H (4.20%) N (33.30%)	
	Water	WATER	1.0	H (11.19%) O (88.81%)	
	Vacuum	Vacuum	0.000	H (100.00%)	
	Self created	Steel	Steel1	7.76	Fe (93.5%) S (1.0%) Mn (5.0%) C (0.5%)
		Steel	Steel2	8.19	Fe (75.9%) S (11.0%) Si (1.0%) Cr (12.0%) P (0.1%)
Steel		Steel3	8.19	Fe (69.0%) S (10.0%) Si (1.0%) Cr (18.0%) Mn (2.0%)	
Ezcut		EZcut	7.9	Fe (98.0%) Mn (2.0%)	
Tungsten		W	15.0	W (100.00%)	

Table 10. Elements present in the simulation

Name	Symbol	A (g/mol)	Z	Relative abundances of isotopes	
Hydrogen	H	1.01	1	¹ H (99.99%)	² H (0.01%)
Beryllium	Be	9.01	4	⁹ Be (100.0%)	
Carbon	C	12.011	6	¹² C (98.93%)	¹³ C (1.07%)
Oxygen	O	16.00	8	¹⁶ O (99.76%)	¹⁷ O (0.04%) ¹⁸ O (0.20%)
Aluminum	Al	26.98	13	²⁷ Al (100.00%)	
Silicon	Si	28.09	14	²⁸ Si (92.23%)	²⁹ Si (4.68%) ³⁰ Si (3.09%)
Phosphorus	P	30.974	15	³¹ P (100.00%)	
Sulfur	S	32.064	16	³² S (94.93%)	³³ S (0.76%) ³⁴ S (4.29%) ³⁶ S (0.02%)
Chromium	Cr	51.9961	24	⁵⁰ Cr (4.84%)	⁵² Cr (83.79%) ⁵³ Cr (9.50%) ⁵⁴ Cr (2.37%)
Manganese	Mn	54.94	25	⁵⁵ Mn (100.00%)	
Iron	Fe	55.85	26	⁵⁴ Fe (5.84%)	⁵⁶ Fe (91.75%) ⁵⁷ Fe (2.12%) ⁵⁸ Fe (0.28%)
Nickel	Ni	58.69	28	⁵⁸ Ni (68.08%)	⁶⁰ Ni (26.22%) ⁶¹ Ni (1.14%) ⁶² Ni (3.63%) ⁴⁴ Ni (0.93%)
Copper	Cu	63.55	29	⁶³ Cu (69.17%)	⁶⁵ Cu (30.83%)
Tantalum	Ta	180.95	73	¹⁸⁰ Ta (0.01%)	¹⁸¹ Ta (99.99%)
Tungsten	W	183.84	74	¹⁸⁰ W (0.12%)	¹⁸² W (26.50%) ¹⁸³ W (14.31%) ¹⁸⁴ W (30.64%) ¹⁸⁶ W (28.43%)
Lead	Pb	207.22	82	²⁰⁴ Pb (1.40%)	²⁰⁶ Pb (24.10%) ²⁰⁷ Pb (22.10%) ²⁰⁸ Pb (52.40%)

B Validation figures

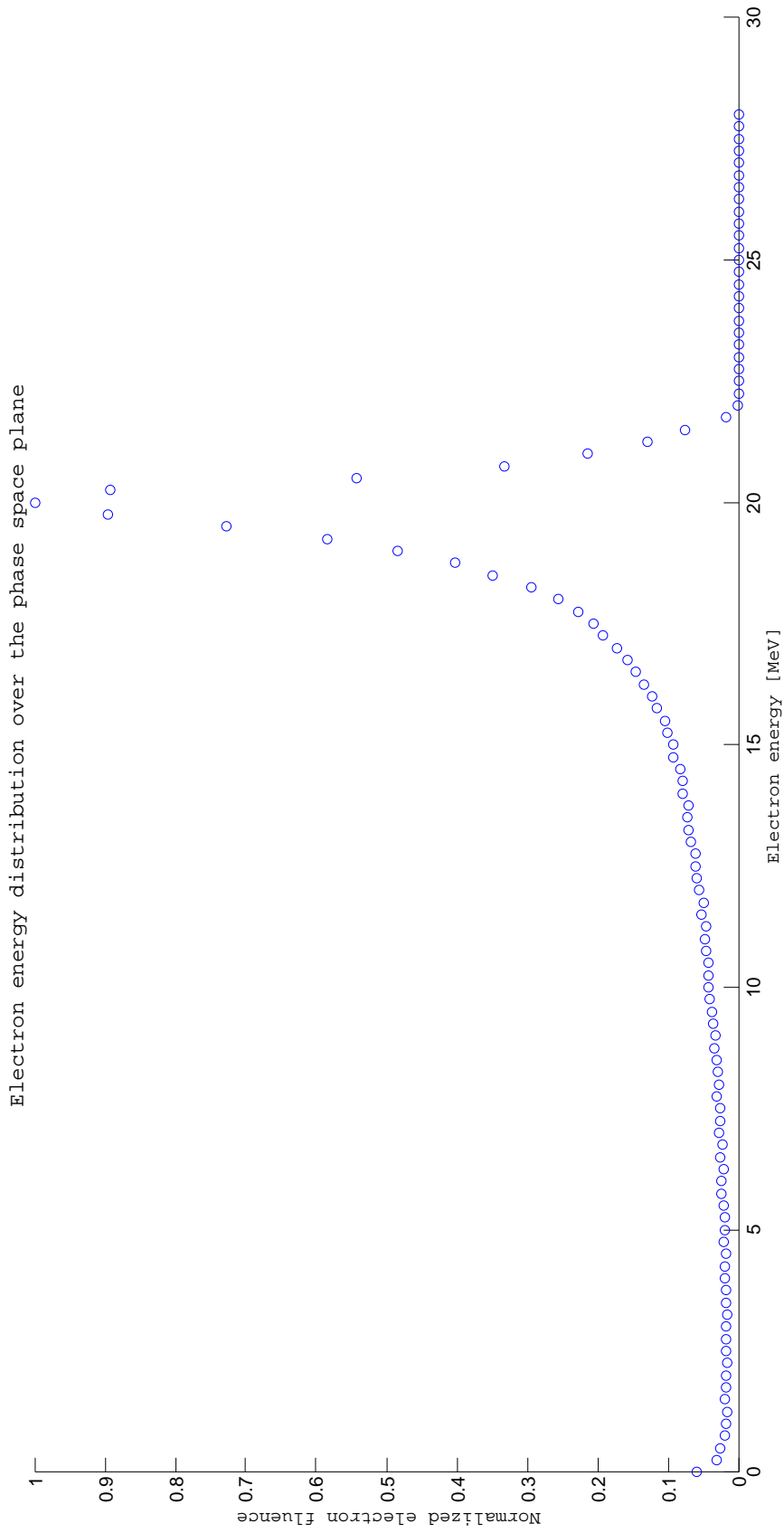


Figure 16. The electron energy spectrum in the central region of the 20 MeV electron beam.

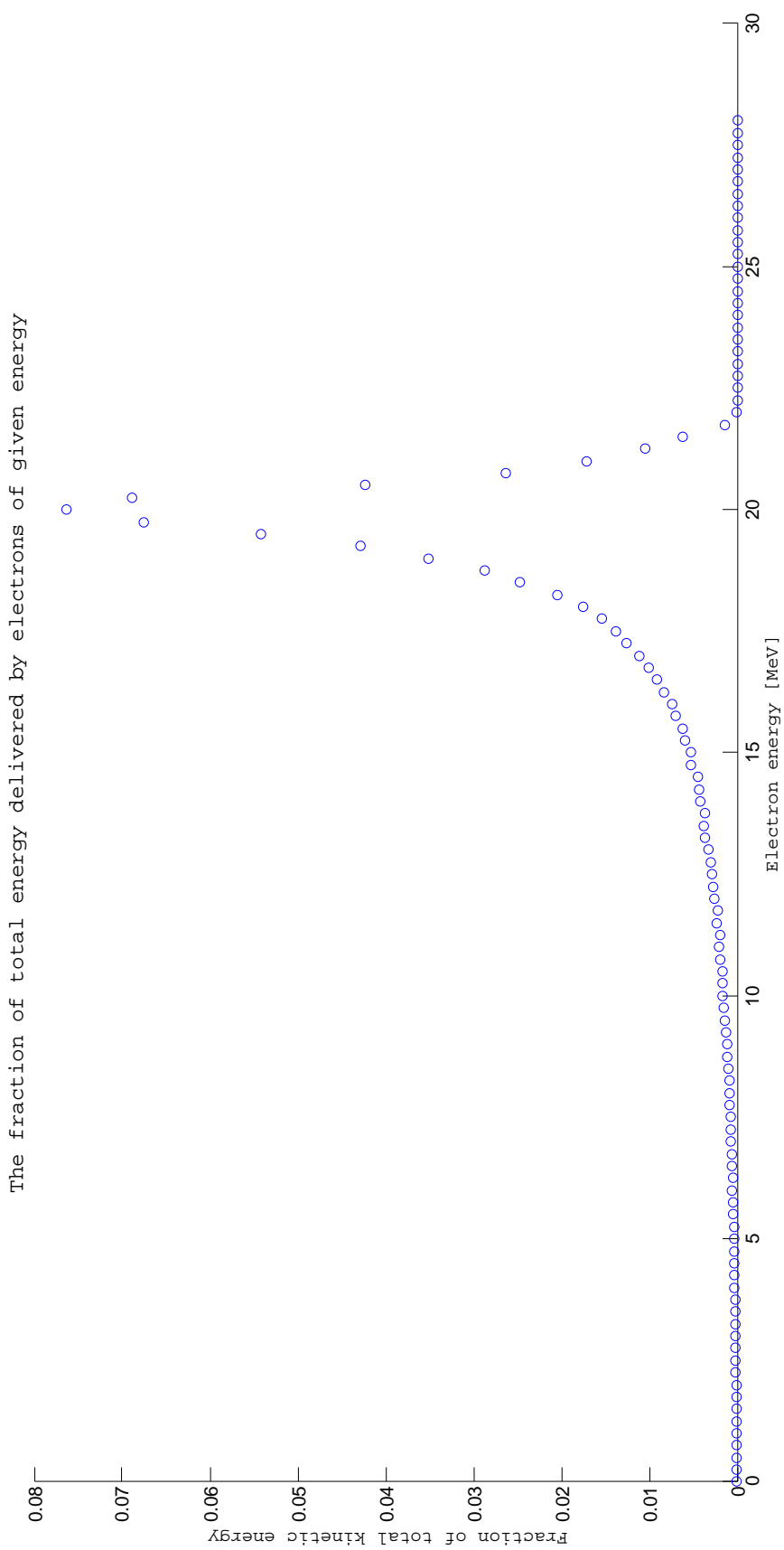


Figure 17. Fraction of total beam energy delivered by electrons of different energies.

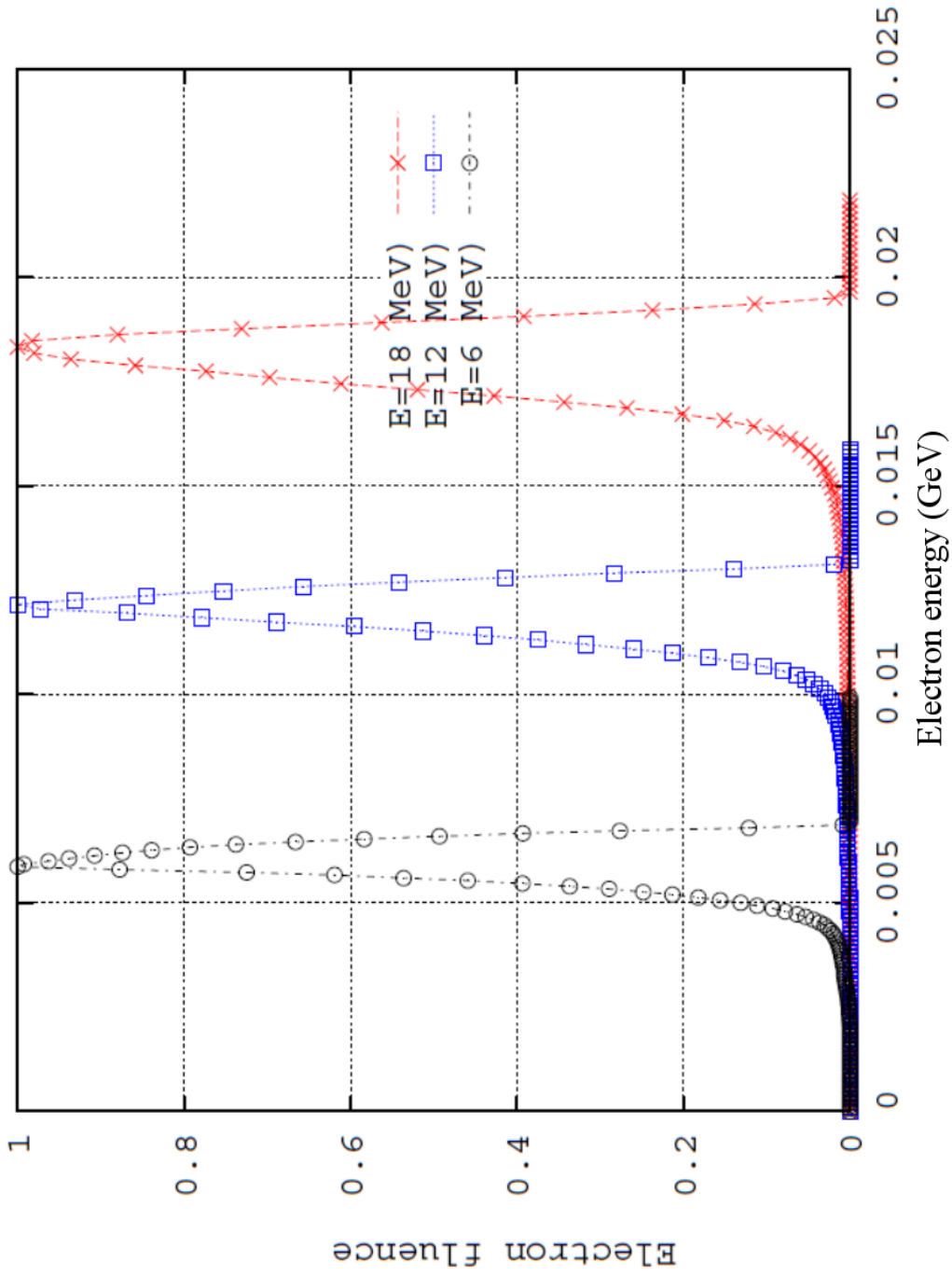


Figure 18. Electron energy spectra for 6 MeV, 12 MeV and 18 MeV beams computed by Dhole et. al [82]. The axis labels in the original image are faulty and have been corrected here. The unit of energy in this figure is GeV and the electron fluence is normalized and therefore dimensionless.

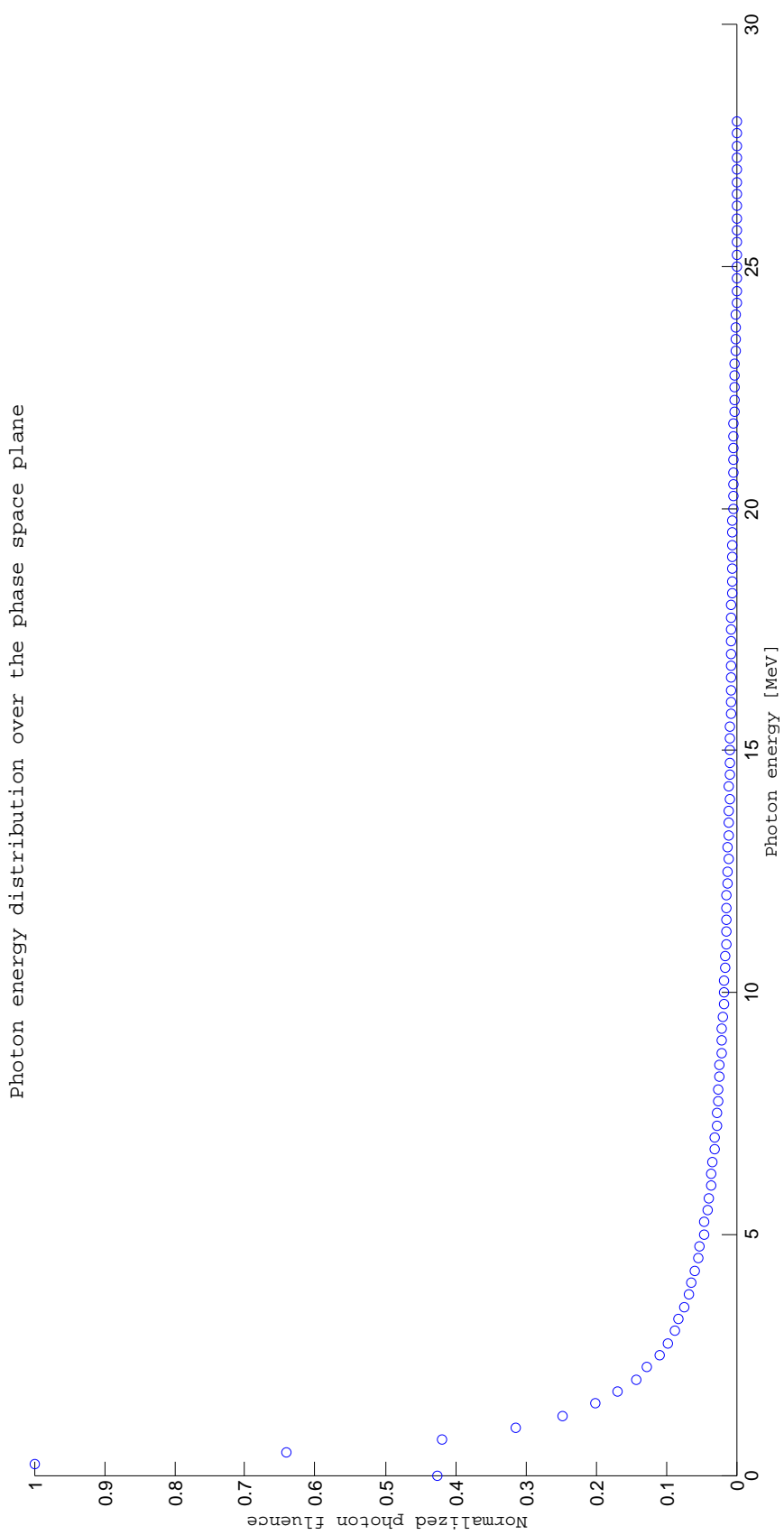


Figure 19. The photon energy spectrum in the central region of the 20 MeV electron beam.

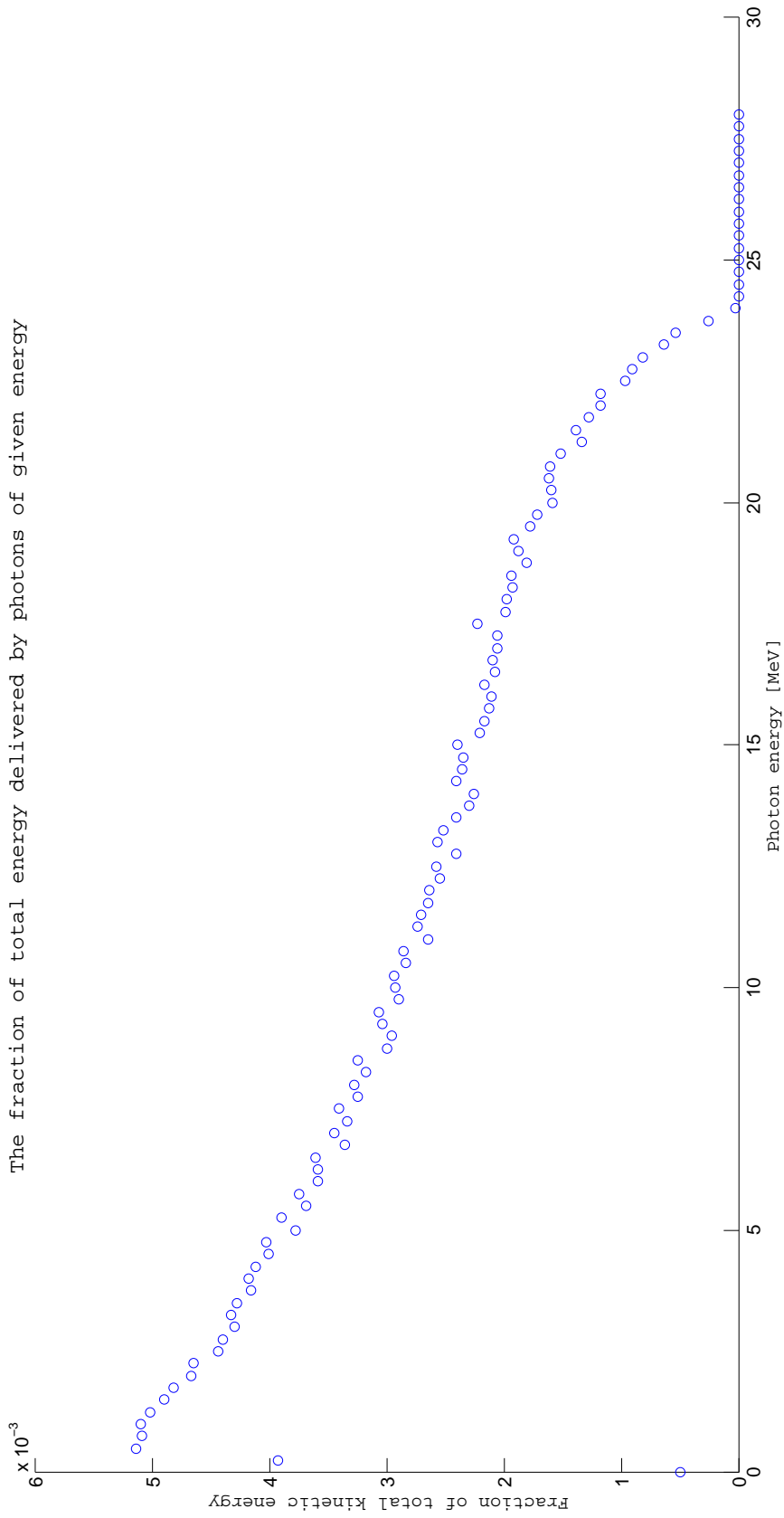


Figure 20. Fraction of total beam energy delivered by photons of different energies.

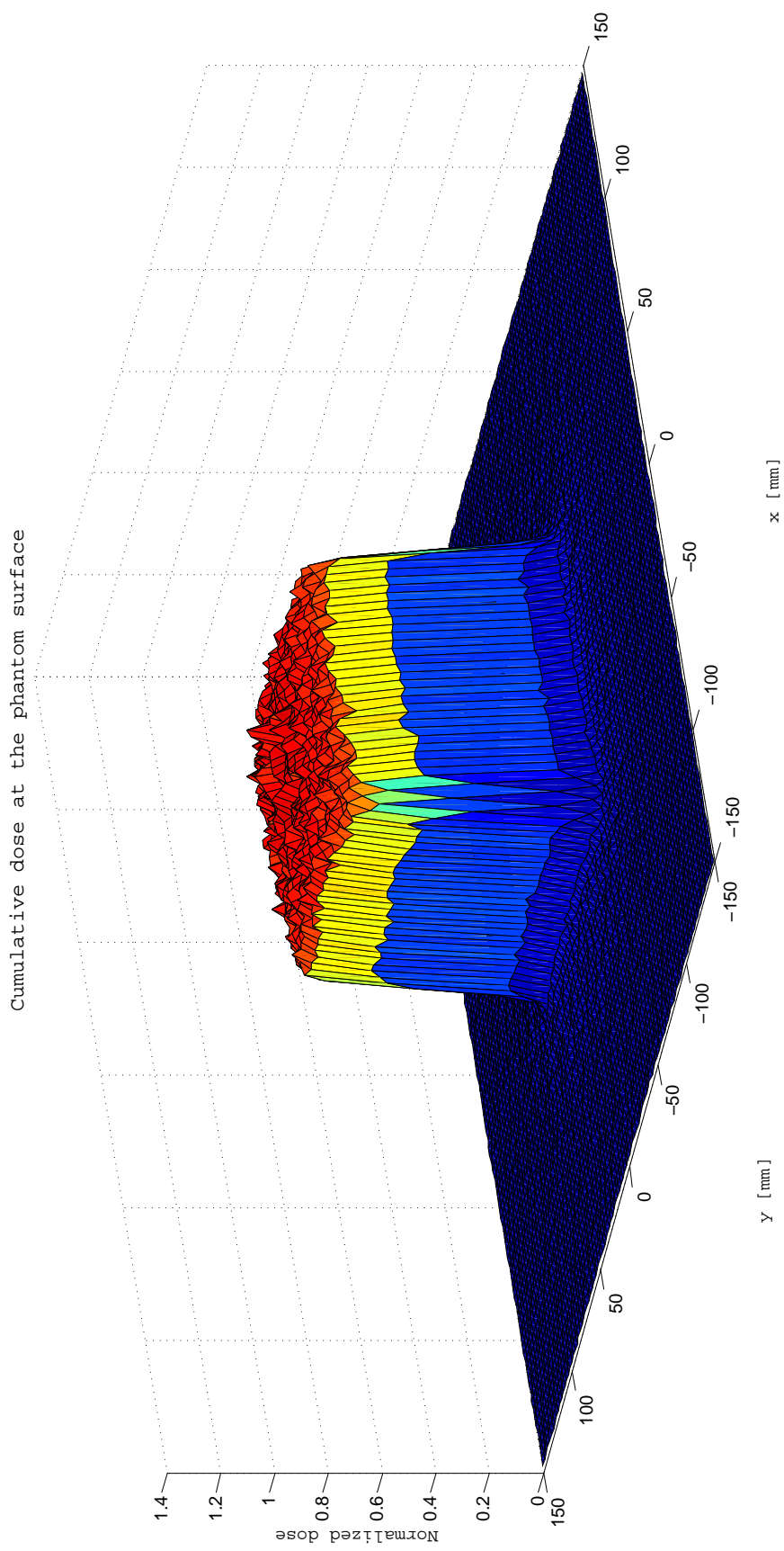


Figure 21. A color map of the relative dose distribution on the surface of the water phantom for a 20 MeV electron beam.

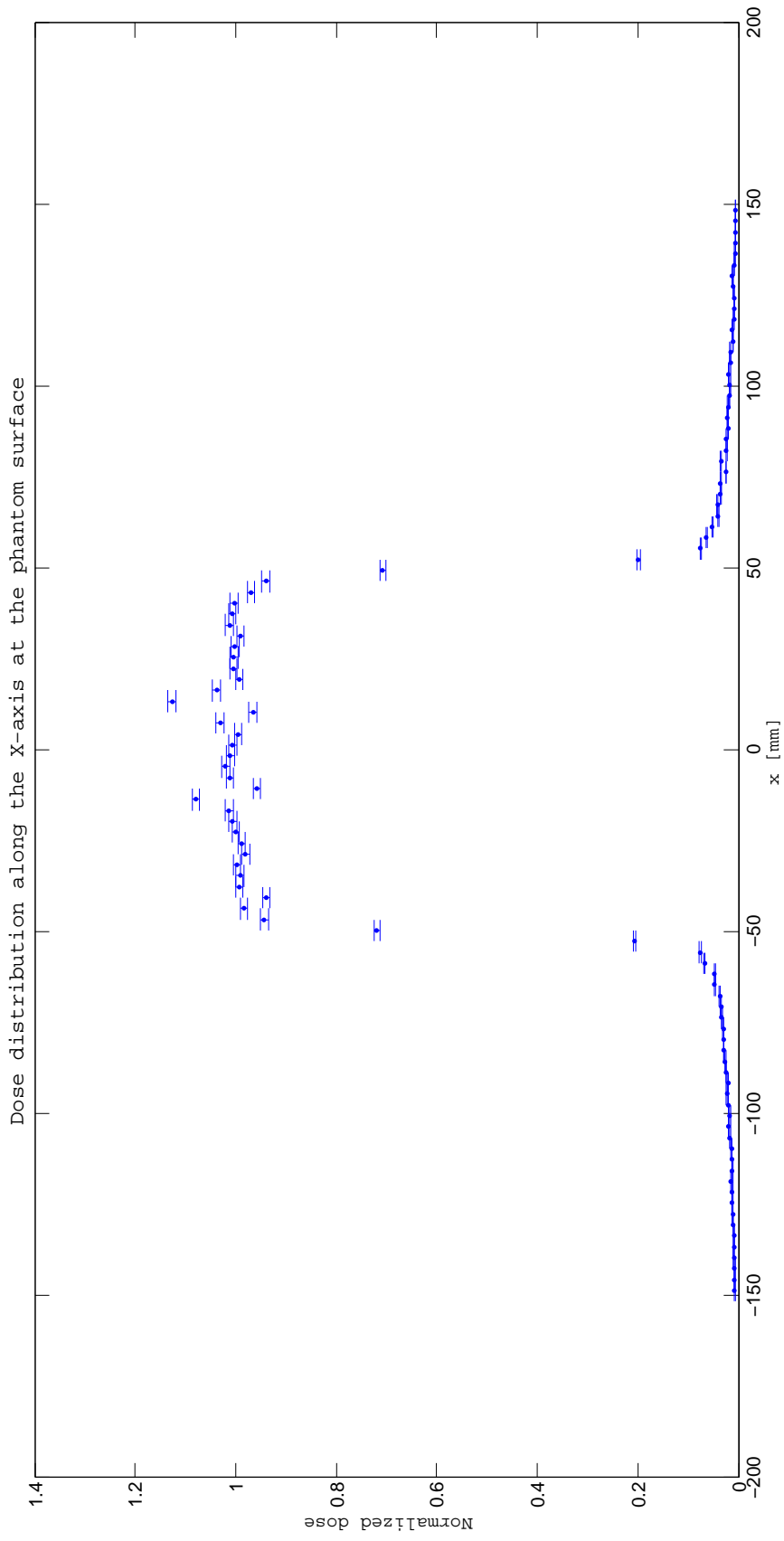


Figure 22. A cross sectional profile of the relative surface dose distribution in x direction with error bars.

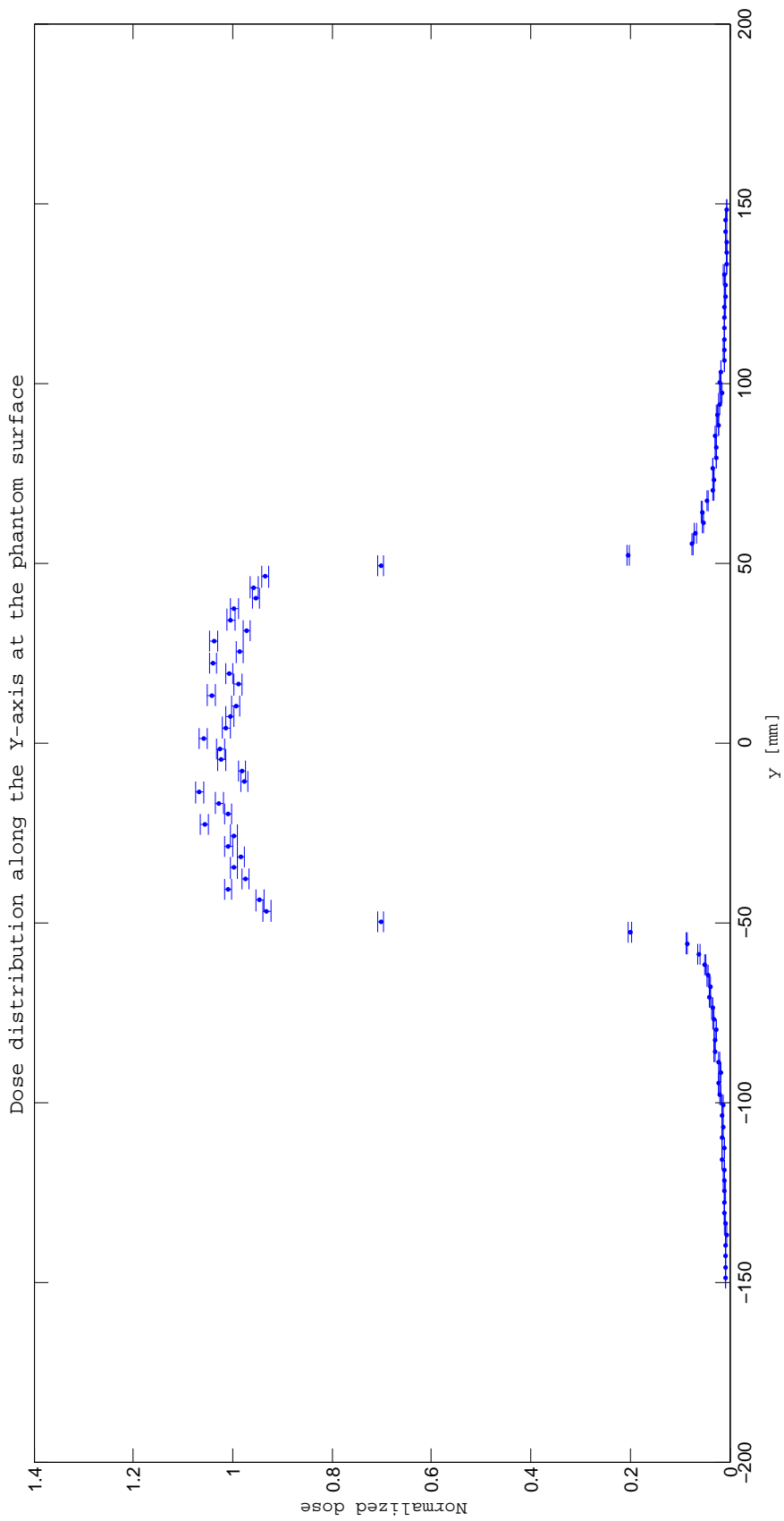


Figure 23. A cross sectional profile of the relative surface dose distribution in y direction with error bars.

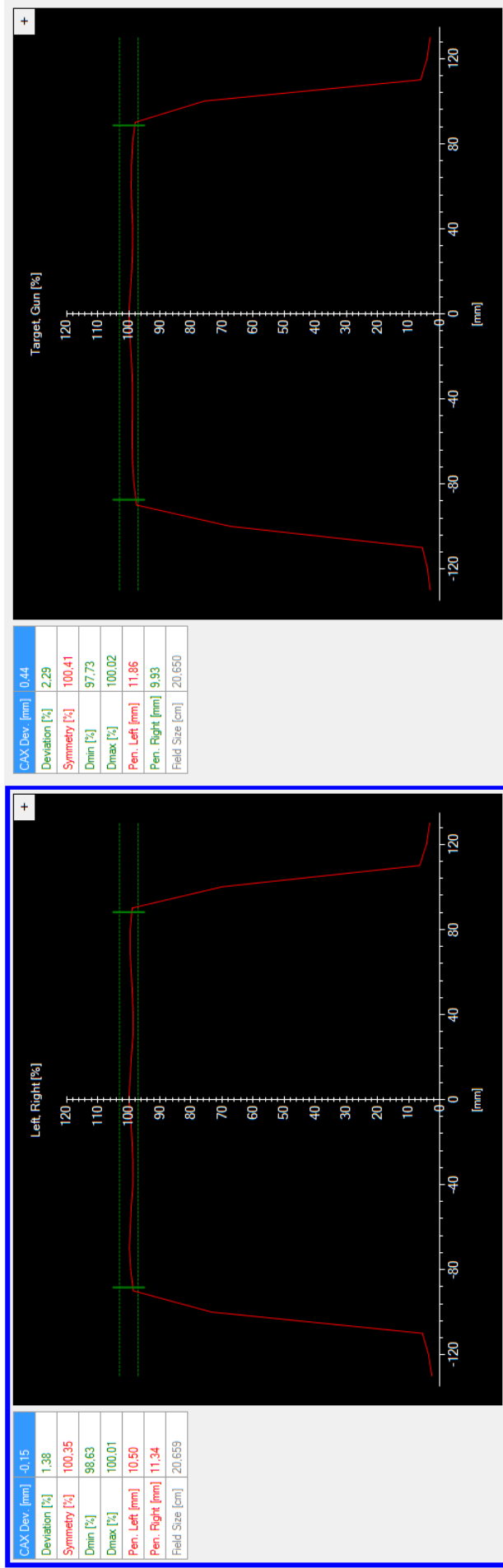


Figure 24. Dose profile measurements for Varian Clinac 2100 C/D done at JYU. These profiles are for 20 MeV electrons with a beam size of 20 cm times 20 cm. The measurements were done with a PTW OCTAVIUS 729 detector at 100 cm SSD.

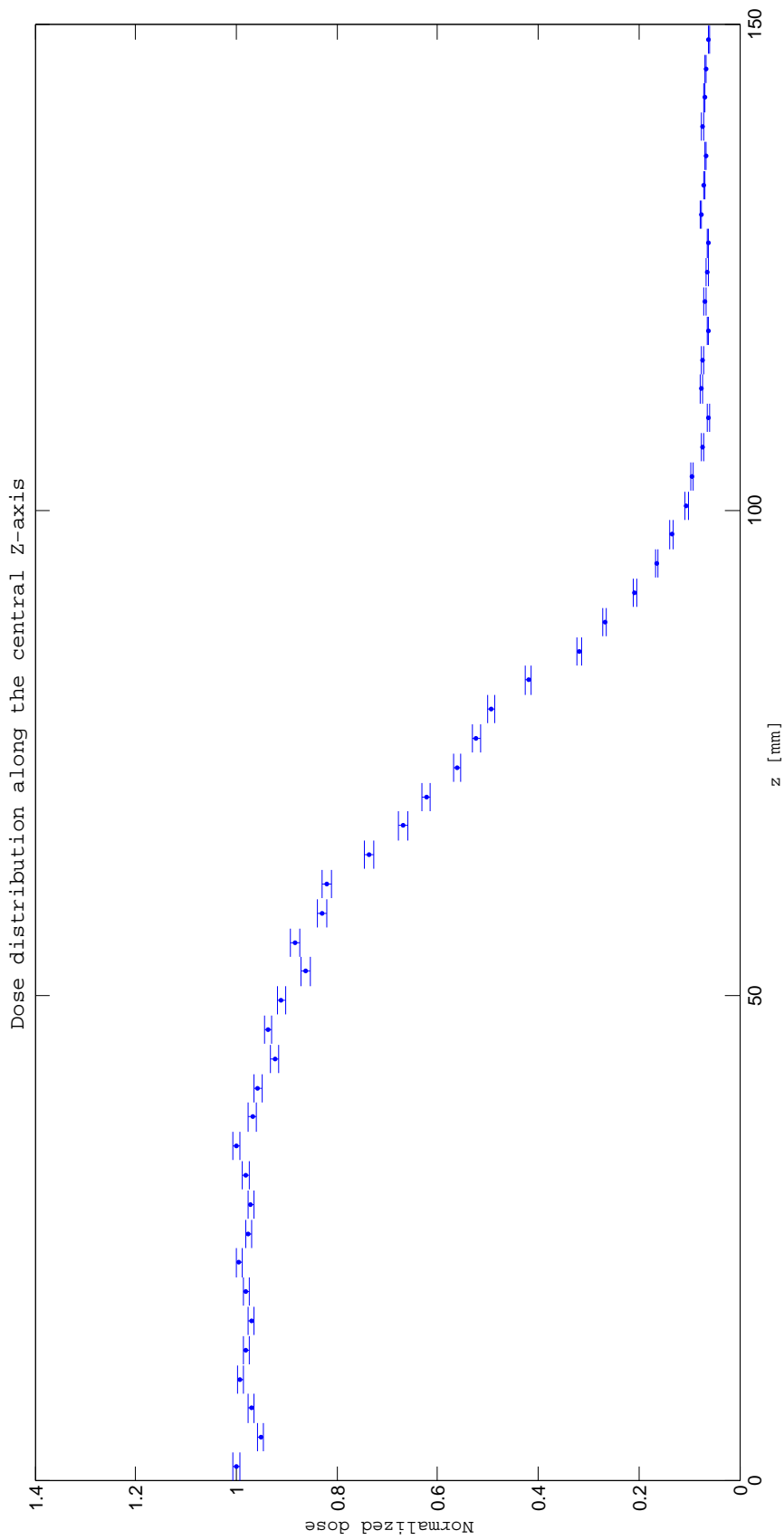


Figure 25. A scatter plot of the percentage depth dose profile for the 20 MeV electron beam in water with error bars included. The profile is calculated from the center of the beam.

44

WP600 20e Depth of Ionization

2UPPA0M0.0AJ/ D tank
 displacement .2 cm 2100 #1306/Sep-25-1988
 Dmax = 1.58 cm 20MeV/electrons
 R90 = 5.48 cm 45.00x45.00/SSD=100.00cm
 R90 = 6.52 cm depth dose
 R90 = 6.10 cm mod:smoothed
 R90 = 6.52 cm
 smooth least sq- 7

FFN = 8.17 BMG (mV) = 54.54
 GAN I = 8.29 GAN I (mA) = 2.6
 BR = -0.44 TRST I (mA) =
 BT = -0.39 TRST I (V) =
 AR = 8.74 SCL1 = 54.7
 AT = -1.28 PFER = 2.1
 PT = -0.48
 TRIM = -0.88 BY Adas L.

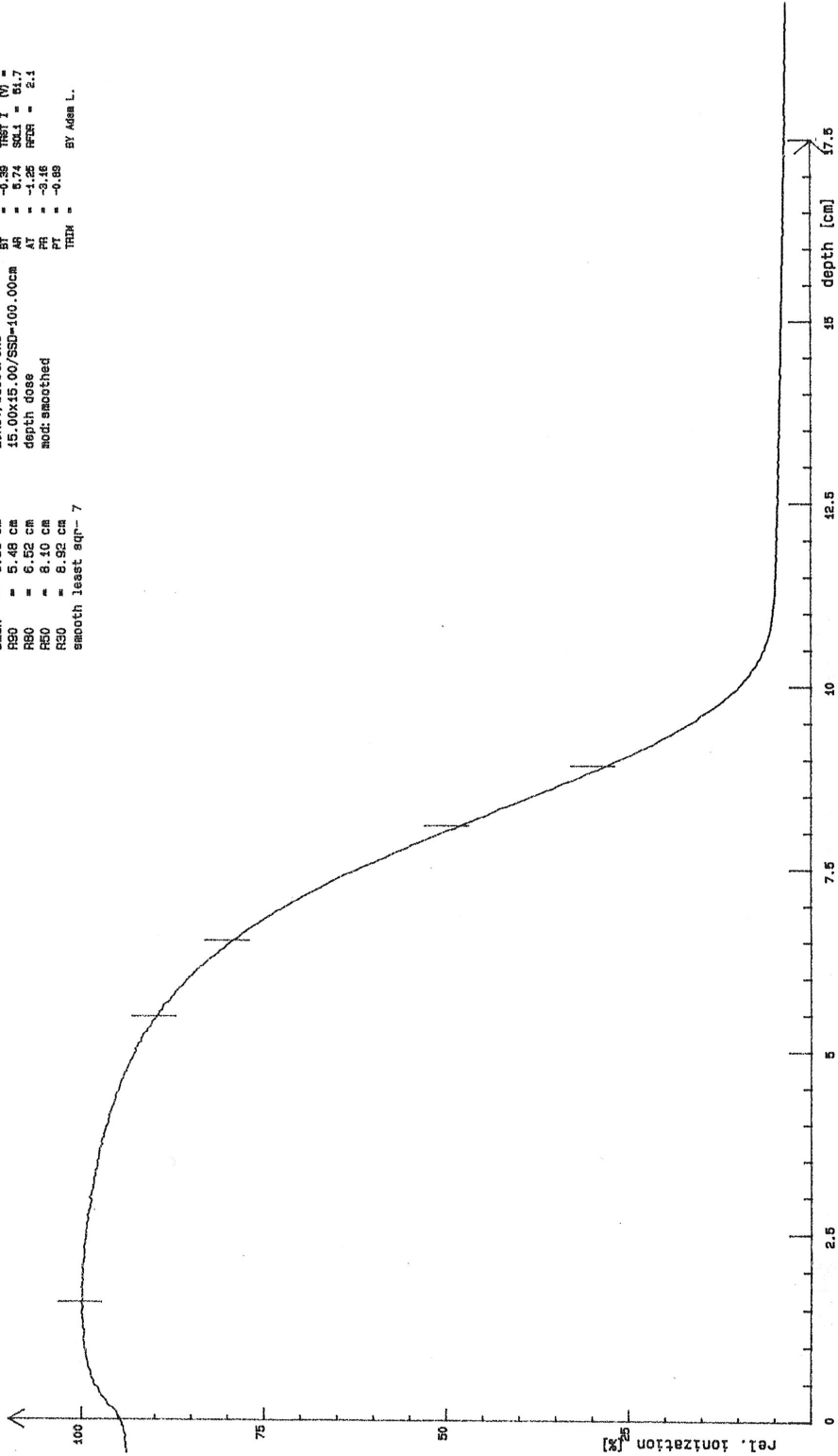


Figure 26. A percentage depth dose profile measurement in water for a 20 MeV electron beam of Varian Clinac 2100 C/D done at Kuopio University Hospital in 1998. The profile was measured using Wellhofer WP600 scanning tank physics equipment for a 15 cm by 15 cm beam area.

442

WP600 12a Depth of Ionization

2HPPA0H0.0AH/ D tank
 displacement .2 cm 2100 #1306/Sep-25-1998
 Dmax = 2.61 cm 12MeV/electrons
 R90 = 3.75 cm 45.00x15.00/SSD=100.00cm
 R80 = 4.13 cm depth dose
 R50 = 4.88 cm read: smoothed
 R30 = 5.34 cm
 smooth least sq= 7

PFN = 6.29 BMAG (MV) = 31.00
 GEN I = 4.39 GEN I (MA) = 7.0
 BR = -0.67 TRIT I (MA) =
 R = 0.78 TRIT I (MA) =
 AT = -2.78 SW1 = 68.4
 PR = -0.40 PFER = 8.0
 FT = -2.04
 TRXR = -4.45
 BY Ahsa L.

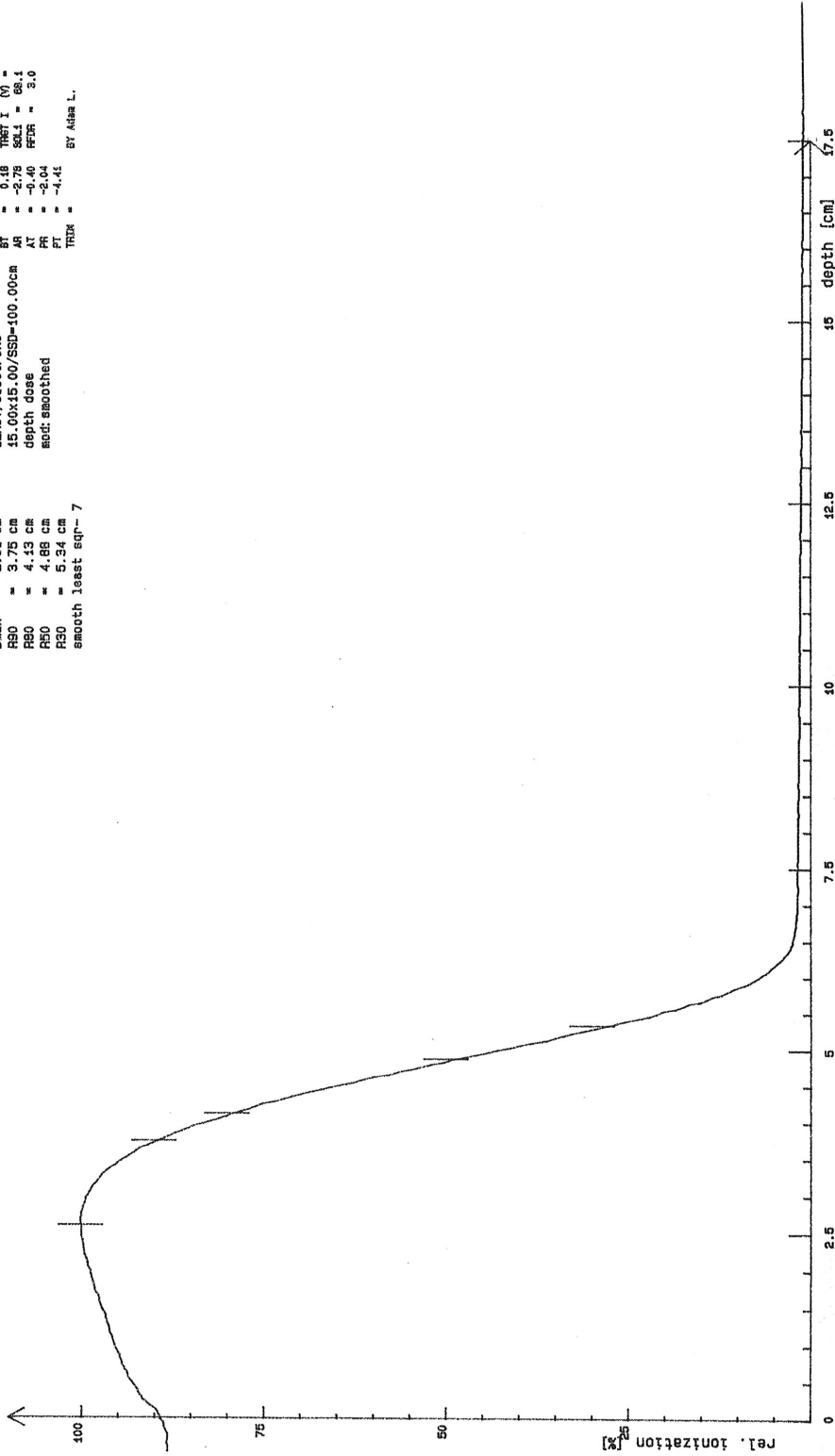


Figure 27. A percentage depth dose profile measurement in water for a 12 MeV electron beam of Varian Clinac 2100 C/D done at Kuopio University Hospital in 1998. The profile was measured using Wellhofer WP600 scanning tank physics equipment for a 15 cm by 15 cm beam area.

40

WP600 6e Depth of Ionization

2BPFA0H0.0AF/D tank
 displacement .16 cm 2100 #1306/Sep-25-1998
 Dmax = 1.19 cm 6MeV/6electrons
 R90 = 1.70 cm 15.00x15.00/SSD=100.00cm
 R80 = 1.90 cm depth dose
 R50 = 2.27 cm mod: smoothed
 R30 = 2.52 cm
 smooth leaset eqn= 7

PRN = 6.39 BHAG (mV) = 15.92
 GUN I = 6.01 GUN I (uA) = 60.0
 RI = 2.08 TRST I (uA) =
 AR = -1.10 SG1 = 84.3
 AT = -1.48 RFR = 2.2
 PR = 0.23
 PT = -0.02
 TRIM = BY ADNA L.

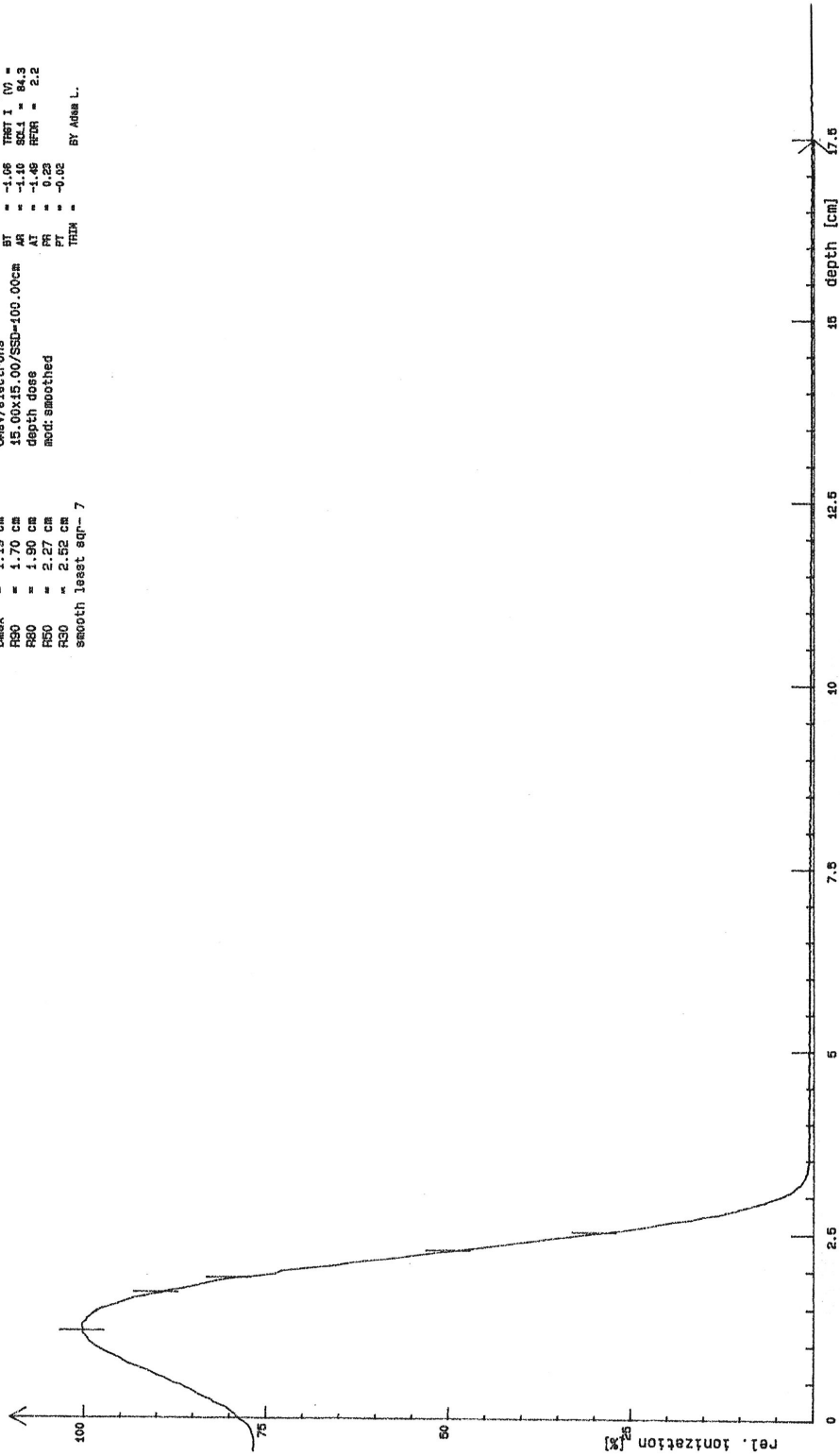


Figure 28. A percentage depth dose profile measurement in water for a 6 MeV electron beam of Varian Clinac 2100 C/D done at Kuopio University Hospital in 1998. The profile was measured using Wellhofer WP600 scanning tank physics equipment for a 15 cm by 15 cm beam area.

C PDD curves for water and silicon phantoms

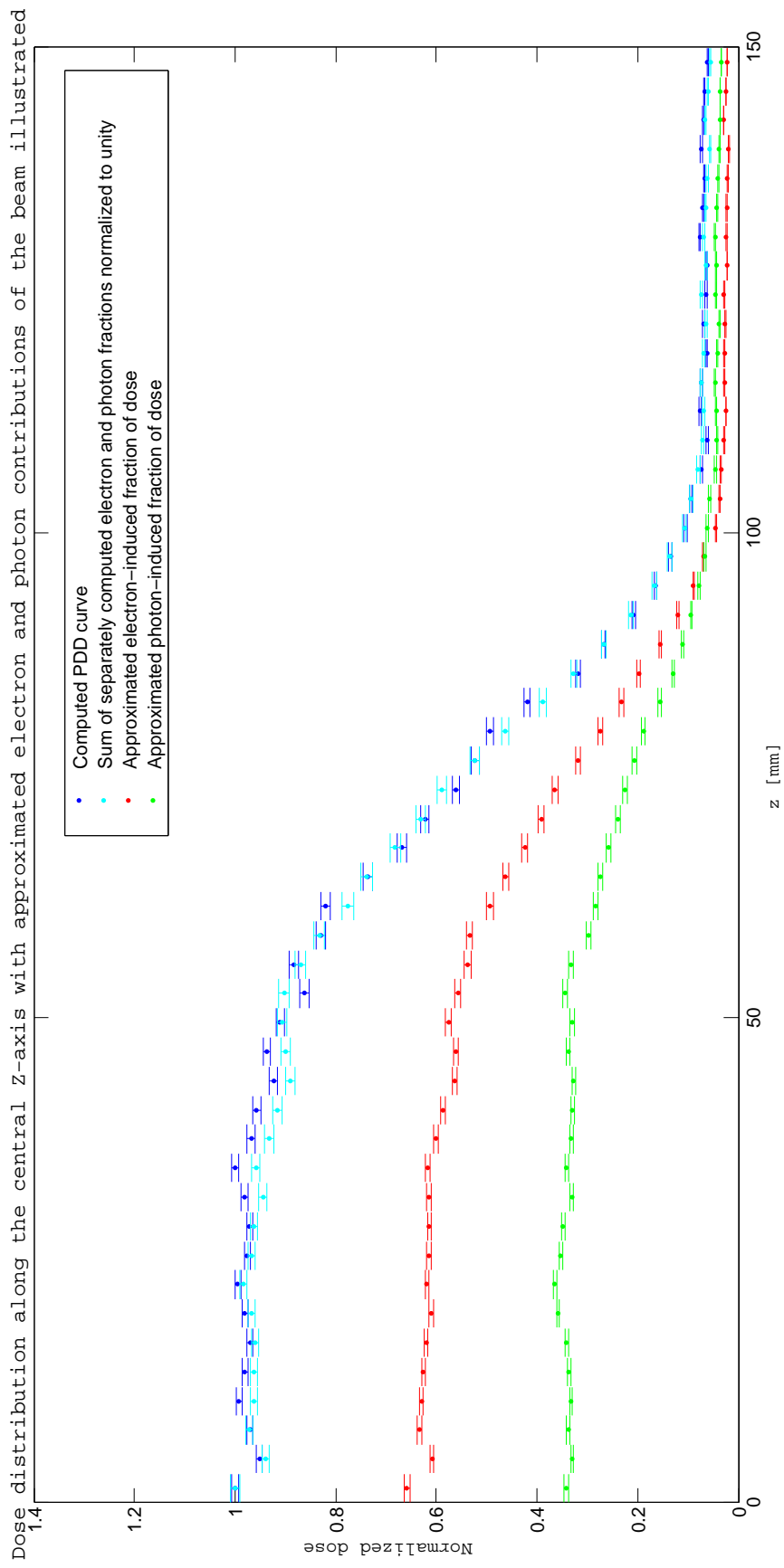


Figure 29. PDD curves for in-depth analysis of dose deposition in water.

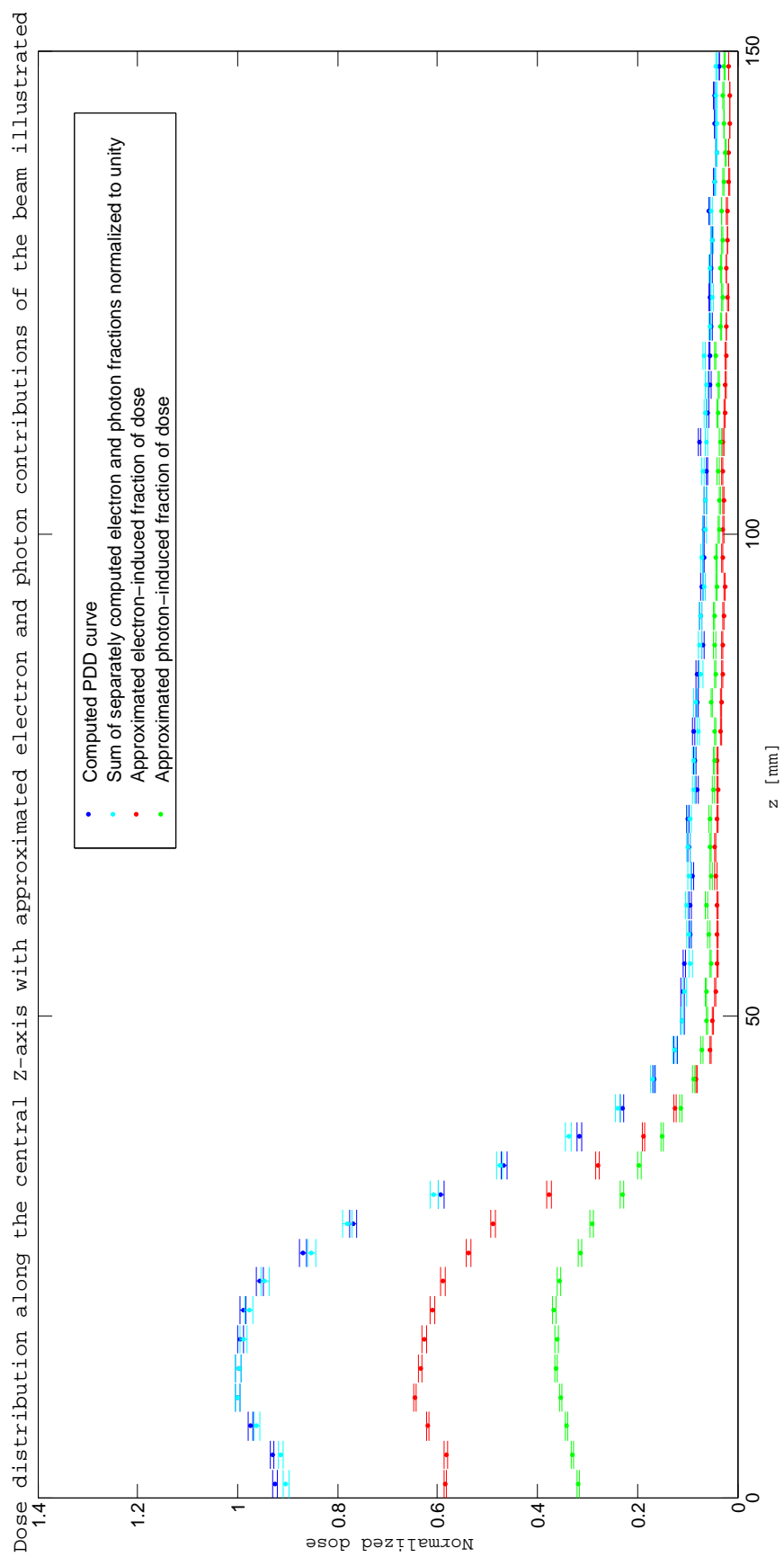


Figure 30. PDD curves for in-depth analysis of dose deposition in silicon.